Universidade do Minho
Escola de Engenharia

Hugo Daniel da Costa Dinis

Wireless power transmission for power-hungry biomedical devices

maio de 2021

UMinho | 2021
Hugo Daniel da Costa Dinis
Wireless power transmission for power-hungry biomedical devices

Universidade do Minho
Escola de Engenharia

Hugo Daniel da Costa Dinis

Wireless power transmission for power-hungry biomedical devices

Tese de Doutoramento
Engenharia Biomédica

Trabalho efetuado sob a orientação do
Professor Doutor Paulo M. Mendes

maio de 2021

DIREITOS DE AUTOR E CONDIÇÕES DE UTILIZAÇÃO DO TRABALHO POR TERCEIROS

Licença concedida aos utilizadores deste trabalho

Agradecimentos

Em primeiro lugar, quero agradecer aos meus pais, Fernando e Jacinta, e à minha irmã Diana. O meu mais sincero obrigado pelo amor, carinho e dedicação ao longo da minha vida. O que sou hoje devo-o também a vocês. Em particular aos meus pais, agradeço o esforço e sacrifícios que sempre fizeram para que nunca me faltasse nada neste meu percurso.

Agradeço à Denise pelos momentos que partilhamos, pelo amor, força e motivação que me dá, e pelo carinho e boa disposição constante.

Ao meu orientador, Paulo Mendes, um muito obrigado por este percurso que já dura há sete anos. Agradeço tudo o que me ensinou, a disponibilidade, a frontalidade, os desafios que me foi colocando e a confiança que deposita em mim. O meu crescimento enquanto investigador deve-se muito a si e às oportunidades que me proporcionou. Obrigado!

Aos meus colegas e amigos do laboratório agradeço a amizade, os bons momentos, as memórias que ficarão para sempre e as palhaçadas no geral. É o ambiente fenomenal que cultivamos que torna os dias de trabalhos um prazer. Em particular, agradeço ao Ivo, ao Vítor, à Margarida e à Cristiana, com quem partilhei o laboratório durante mais tempo e que faziam dos dias uma animação. Ao Anacleto, um obrigado pelo apoio constante e risadas que foi dando ao longo dos anos!

Spiral out. Keep going.

- *Tool*

O autor foi financiado pela Fundação para a Ciência e Tecnologia (FCT) através da bolsa SFRH/BD/116554/2016, cofinanciada pelo FSE através do Programa Operacional Regional Norte.

STATEMENT OF INTEGRITY

I hereby declare having conducted this academic work with integrity. I confirm that I have not used plagiarism or any form of undue use of information or falsification of results along the process leading to its elaboration.

I further declare that I have fully acknowledged the Code of Ethical Conduct of the University of Minho.

Resumo

Transferência de energia sem fios para dispositivos biomédicos de consumo elevado

As fontes de energia tradicionais limitam a miniaturização de dispositivos médicos implantáveis, dado que a densidade energética das baterias é insuficiente e o fabrico e integração destas com microssistemas é um desafio. Métodos alternativos para alimentar estes dispositivos são, portanto, muito desejados. Isto permitiria o desenvolvimento de dispositivos mais pequenos, necessários para a criação de novas aplicações que irão revolucionar os cuidados de saúde.

À medida que os dispositivos implantáveis ficam mais pequenos, a eficiência da transferência de energia também diminui devido a transdutores e antenas menos eficientes ou ao uso de frequências mais altas que sofrem maior atenuação nos tecidos. Para compensar isto, deve-se aumentar a potência transmitida. Contudo, existem regras de segurança que impõem limites à potência que podemos enviar através do corpo humano.

Esta tese aborda as lacunas dos sistemas de transferência de energia sem fios tradicionais através da exploração de parâmetros da ligação que permitam o aumento da energia transferida para o implante sem aumentar os níveis de SAR. Para tal, foi desenvolvido um sistema de transferência de energia sem fios que usa múltiplos transmissores. Através do posicionamento dos transmissores de forma a que os caminhos de propagação de cada um dos seus sinais não se intersetem à superfície do meio, onde o SAR é maior, a energia colocada dentro do meio aumenta enquanto o SAR máximo permanece inalterado. Juntamente com um mecanismo de focagem de energia através da manipulação das fases dos sinais, a distribuição de potência dentro de um fantoma de cabeça humana aumentou drasticamente mantendo o SAR máximo inalterado. O sistema proposto forneceu -13.7 dBm a uma antena colocada a uma profundidade de 5.3 mm num fantoma de cabeça humano. Ajustando a potência transmitida para o SAR_{10g} ser 10 W/kg, a antena receberia -0.9 dBm. Foi também demonstrado que o sistema aumenta até 18 dB e 25 dB a potência entregue a um dispositivo sem fios que circula dentro de modelos de corpo e cabeça humano, respetivamente, comparativamente a um sistema tradicional de uma antena.

O sistema de transferência de energia sem fios apresentado nesta tese é escalável, segue o implante enquanto este se move, e concentra energia na sua localização. Adicionalmente, trata o meio como uma caixa negra, não precisando de informação prévia sobre este. Assim sendo, o dispositivo desta tese tem o potencial de contribuir para a forma como se implementam ligações de transferência de energia sem fios para implantes médicos miniaturizados.

Palavras-chave: Transferência de energia sem fios, dispositivo médico implantável, SAR

Abstract

Wireless power transmission for power-hungry biomedical devices

Conventional power sources remain a major bottleneck in implantable medical device miniaturization, as the achievable energy densities of batteries are insufficient and fabrication and integration with microsystems are still a challenge. Alternative powering methods that can provide energy for the implantable medical device are highly desirable, as the device’s lifetime would no longer be directly correlated to its battery size, allowing the development of smaller devices. This miniaturization of implantable electronic devices is a necessary step to enable new applications that will revolutionise healthcare.

Wireless power transfer is an attractive technology to satisfy the power needs of implantable devices. Nevertheless, as implants become smaller, so do their antennas/transducers, causing the efficiency of the power transfer link to decrease, and forcing the use of high frequencies which suffer more attenuation as they propagate through the tissue. To compensate, more power needs to be made available to the implant. However, safety regulations impose a limit to the power transmitted through a human body.

This thesis addresses the shortcomings of a traditional wireless power transfer link, by looking into link parameters that can be explored to increase the power delivered to an implant without increasing the maximum SAR value in the medium. To accomplish this, a wireless power transfer system using multiple transmitters was developed. This was achieved by ensuring that the propagation paths of the transmitters’ signals didn’t overlap at the surface of the medium, where SAR is typically higher. Together with the use of a focusing and tracking method through phase control, the power availability inside a human head phantom increased dramatically all over. A power of -13.7 dBm was delivered to an antenna inside a human head phantom at a depth of 5.3 mm. Adjusting the transmitted power for a SAR_{10g} of 10 W/kg, -0.9 dBm would be delivered to the antenna. It was also demonstrated that the proposed system increases the power delivery by up to 18 dB and 25 dB to a wireless device circulating inside human body and head models, respectively, compared to a single transmitter system.

The presented wireless power transfer system is scalable, can track the implant as it moves, and focuses the power in its location. Additionally, it doesn’t require information about the medium, treating it as a black box. As such, this thesis’ findings can contribute to shaping how future wireless power transfer links to miniaturized implantable devices are developed.

Keywords: Wireless power transfer, implantable medical device, SAR

Table of contents

List of abbreviations and acronyms

CC	Capacitive Coupling
CSF	Cerebrospinal fluid
DBS	Deep brain stimulation
DGBE	Diethylene glycol monobutyl ether
DRIE	Deep reactive-ion etching
DRL	Dosimetric reference limit
EH	Energy harvesting
ERL	Exposure reference level
EWPT	Electrodynamic wireless power transfer
FF	Far-field
IC	Inductive coupling
IMD	implantable medical device
IoT	Internet of Things
ME	Magnetoelectric
MEMS	Microelectromechanical system
MF	Midfield
NEMS	Nanoelectromechanical system
OW	Optical wave
RX	Receiver
SAR	Specific absorption rate
TE	Thermoelectric
TrE	Triboelectric
TX	Transmitter
US	Ultrasound
WPT	Wireless power transfer

List of figures

List of tables

CHAPTER 1 INTRODUCTION

The first implantable medical devices (IMDs) date back to the 1930s, when early attempts of electric stimulation were carried on [1]. From there on a cascade of new devices for a plethora of different applications came to exist. The cardiac pacemaker, a revolutionary medical technology and the first IMD in history, was first introduced in 1952 by Dr. Paul Zoll who experimented with an external pacemaker. Then, in 1960, with the advent of the transistor a few years earlier, Wilson Greatbatch and William Chardack developed the first successful human-implanted pacemaker [2].

The success of the pacemaker made it clear to scientists and engineers that many other health complications could also benefit from similar devices. Therefore, the 1970s and 1980s marked the beginning of the development of IMDs for several other illnesses. For example, the first implantable drug delivery system was developed in that period, aiming to manage diseases that required chronic administration of drugs, such as diabetes. The defibrillator was implanted for the first time in 1980, and neurostimulators for epilepsy treatment and pain management were introduced in the 1990s [2].

With the development of microelectronics and integrated circuits it was possible to miniaturize the devices while simultaneously increasing their capabilities. Sensors, actuators, communication technologies and better, more energy-dense batteries [3], [4] were incorporated into the devices and uncovered a whole new world of medical solutions. Advances in chemical, biological and mechanical transducers, and micro electromechanical systems (MEMS) and nano electromechanical systems (NEMS) technologies overcame many technical barriers. This allowed IMDs to monitor, manage and treat a plethora of medical conditions, improving the quality of life of countless patients [1], [2], [5]

At the time of writing this thesis, a simple search for “implantable medical device” on Google Scholar returns 202 000 results, excluding citations and patents. Narrowing the search to papers published in the last 5 years, the search engine reports 31 800 matches. Naturally, not all these results report on a new device. Reviews, comparisons, and multiple papers per device are a common occurrence. Nevertheless, such a high number of results demonstrates the importance of these devices in the present and is also a good indication of how important they will be in the future. The global IMD market is expected to grow at a rate of 7.3% between 2019 and 2026, and it is expected to reach a market value of around 154 billion USD by the end of that period [6].

In the bibliography, numerous papers report state-of-the-art electronic devices for diagnostic purposes. Examples of such devices are sensors for: intraocular pressure, both invasive [7]–[11] and non-invasive [12], neural activity [13]–[15], bladder pressure [16], glucose [17], [18], blood pressure [19]–[23], pH [24], [25] and intracranial pressure [26], [27]. Actuators are also abundantly present in the literature, as pacemakers and defibrillators [28], neural stimulators [29], cochlear implants [30] and vision restoring devices [31] have recently been reported. Figure 1.1 contains examples of the mentioned devices.

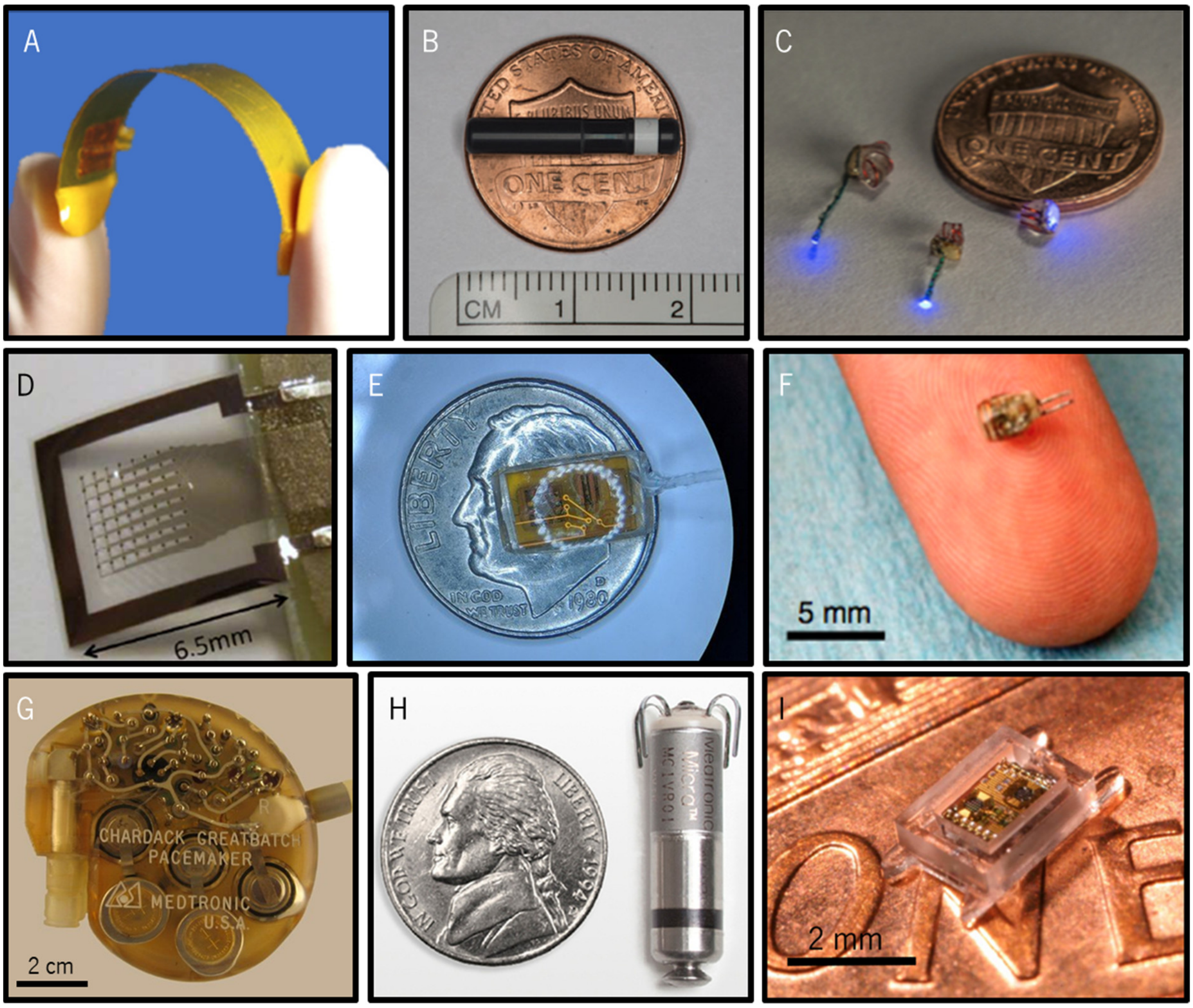

Figure 1.1 -Examples of implantable medical devices. A) Pulmonary artery blood pressure monitor with an internal diameter of 17 mm [21]. B) Fully encapsulated glucose monitor [18]. C) Optical neurostimulator [32]. D) Neuronal activity recorder (the picture shows the array of electrodes and the antenna) [15]. E) Intraocular pressure monitor [11]. F) Wireless pacemaker [33]. G) A 1960s Chardack and Greatbatch pacemaker, roughly 8x7x2.5 cm^3 in size [34], followed by H) Medtronic Micra leadless pacemaker [28] for comparison. I) Wireless intraocular pressure monitor [7].

A modern IMD can be entirely electronic, or it can have mechanical, chemical, or biological components. It can either sense a given physical parameter and relay that information to the outside world through a wireless communication link or actuate on a biological system when instructed to do so. When a device can do both, i.e. monitor a parameter and actuate accordingly, it classifies as a closed-loop control system. IMDs also require a source of energy capable of guaranteeing regular operation during their lifetime, which can be a battery, an external dedicated power source, an energy harvester, or a combination of the above. Figure 1.2 presents a conceptual diagram of a modern IMD containing the mentioned blocks.

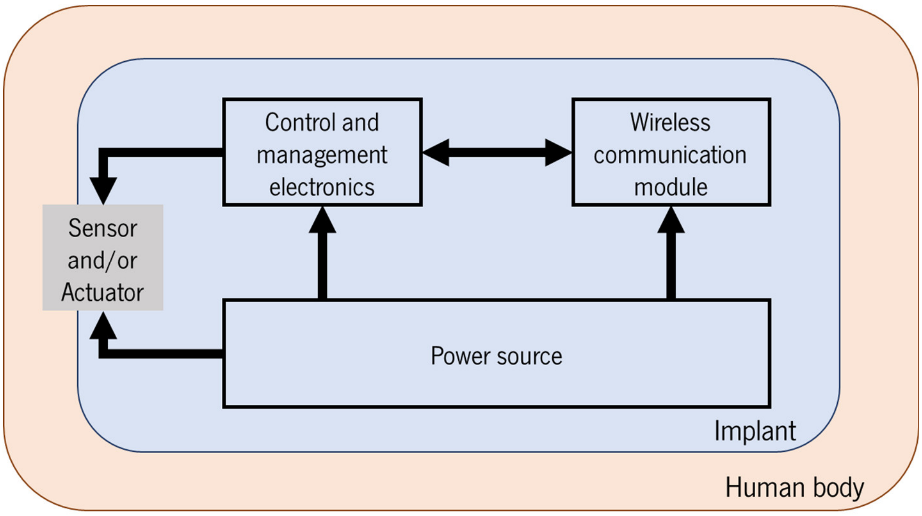

Figure 1.2 - Conceptual diagram of the building blocks of a classic IMD. The sensor and actuator block is in direct contact with the human body to perform its function. The power source can be a battery, a wireless power receiver, an energy harvester, or a combination of these.

As present technological trends bring forth the rise of 5G communications and the Internet of Things (IoT), it shall be possible to develop tailor-made healthcare solutions that better suit a given patient and lead to better monitoring and treatment outcomes. However, when it comes to IMDs, this breakthrough is still challenged by the energy requirements of such devices.

1.1 Powering an implantable medical device

Two extremes can be observed when it comes to IMDs: complex devices comprised of distinct modules to perform diverse functions, much like the devices represented in Figure 1.2, and highly simplified and miniaturized devices that perform a single task.

Entirely passive sensors capable of relaying information to the outside when interrogated by an external device, much like an RFID system, have been presented in the literature. These mix the biological parameter information with the interrogator’s signal and backscatter the modulated signal from which the information is retrieved [35]. Examples of these devices are presented in Figure 1.3. The majority of passive sensors found in the literature are based on LC resonators [20], [36]–[38], where the biological parameter translates into a shift in the resonant frequency of the sensor's coil that is detected by the interrogator. Nonetheless, those are elementary devices that can only be used for very particular and simple applications [39] and do not fit the conceptual IMD description presented in Figure 1.2.

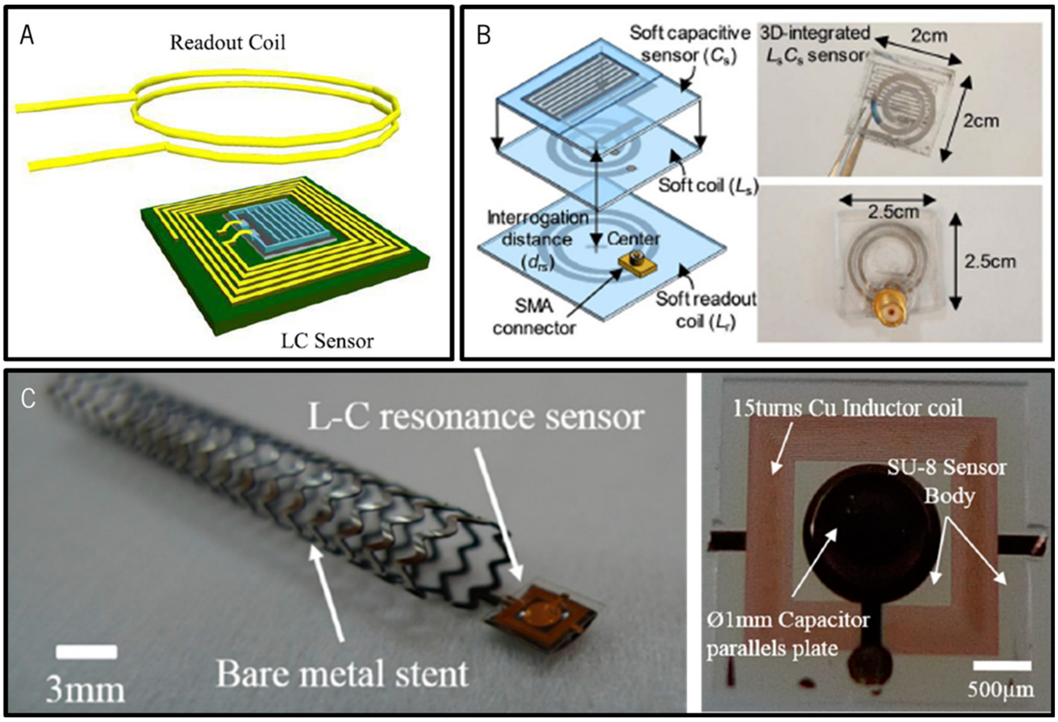

Figure 1.3 – A) and B) present schematic representations of LC-based passive sensors where a capacitive sensor is used to tune an inductor's resonance frequency [36], [37]. The right side of B) shows photographs of the sensor (top) and its interrogator (bottom). C) presents a blood pressure LC sensor attached to a stent (left) and a close-up of the passive sensor (right) [20].

All other IMDs have electronics circuits, communication modules, sensors and actuators that require energy to perform the tasks they are designed for. As such, they must include an energy source.

1.1.1 Batteries

The most common method to provide energy to an IMD is through a battery, as they are portable, reliable, and convenient. Nevertheless, batteries are often bulky and can make up for most of the IMD's volume [40], [41]. Additionally, they need to be replaced periodically [42], which is a significant economic and health burden, and the materials that compose them are toxic, making leakage a severe health concern [43].

Battery technology has not stopped in time, though, as significant research efforts have been made to increase achievable power densities, allow for direct integration with substrates and to make them biocompatible and flexible [3], [43]–[53]. Figure 1.4 presents state-of-the-art batteries for miniaturized devices.

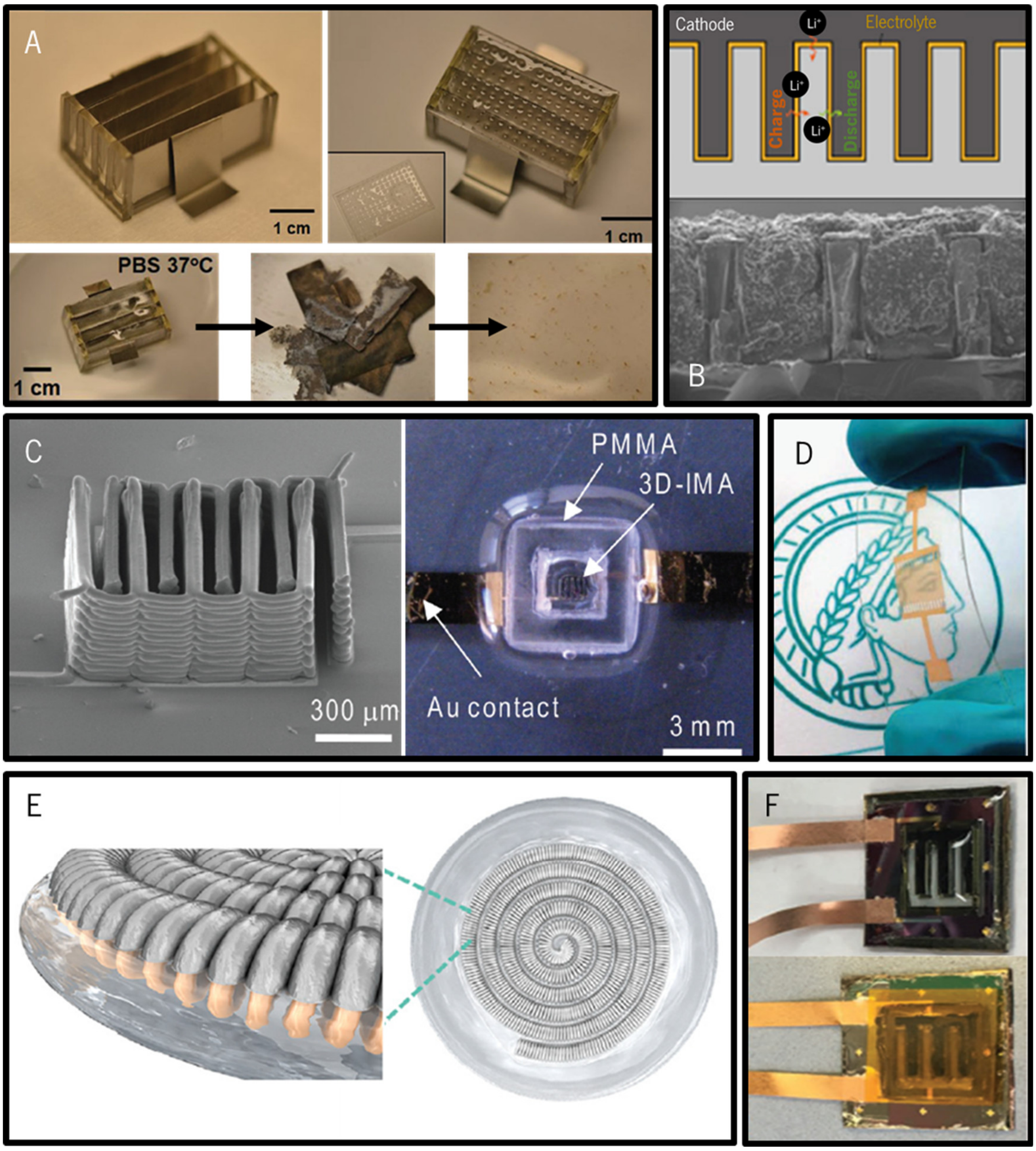

Figure 1.4 - Examples of state-of-the-art battery technology. A) Fully biodegradable magnesium-molybdenum battery (top) and its dissolution process (bottom) [43]. B) 3D microbattery fabricated with standard cleanroom procedures (photolithography and DRIE) with a footprint of 3 x 3 mm^2 [47]. C) 3D-printed interdigitated Lithium-ion battery before (left) and after packaging (right) with a final volume of 2.1 × 2.1 × 1.5 mm^3 [48]. D) Planar flexible micro-supercapacitor [49]. E) Stretchable Lithium-metal anode [3]. G) On-chip Zinc micro-supercapacitor before (top) and after packaging (bottom) (1.8 x 1.8 cm^2) [44].

Supercapacitors with an area of 4 cm^2 have been reported in [45] to achieve an energy density of 40.0 Wh kg^{-1}. In [44], Zinc ion micro-supercapacitors with an area of 3.2 cm^2 achieved an energy density of 0.12 mWh cm^{-2}, while supercapacitors made with printable graphene ink achieved 2.5 mWh cm^{-3} [54]. In the literature there are also reports of 3D Lithium-ion batteries with energy densities of 5.2 mWh cm^{-2} (9mm^2 footprint) [47] and 2.7 mWh cm^{-2} (4.4 mm^2 footprint) [48].

Conventional power sources remain a major bottleneck in IMD miniaturization, as achievable energy densities are insufficient [39] and fabrication and integration with microsystems is still a challenge [55]. Miniaturization and increased safety for patients are fundamental for battery research, and the advent of devices such as supercapacitors and flexible Lithium-ion batteries may push energy storage technology to a point where it may be helpful for miniaturized IMDs in the near future. Nevertheless, alternative powering methods that can provide energy for the IMD are highly desirable [40], [42], as the device's lifetime would no longer be directly correlated to its battery size, thus allowing for smaller devices to be developed.

1.2 Motivation

The performance, reliability, and functionalities of electronic medical devices, such as data collection and wireless communications, are rising. However, these perks are inevitably accompanied by an energy requirement that must be met for proper device operation.

Long-term and reliable powering within the human body has been a major challenge since the development of the first implantable pacemaker. Batteries are used due to extended operation time. Still, their high volume, limited lifetime, and miniaturization limits are an obstacle for further miniaturization of medical implants, limiting the deployment of technologies aiming to reach locations in the human body with severely limited available space.

As device miniaturization is the desired goal, a compromise must be made between battery size, the size of the device itself, and its autonomy. Table 1.1 displays the expected lifespan of commercial electronic biomedical devices that resort to batteries as power sources. As it can be seen, sub-decade battery lifespans can be expected for these devices that require surgical procedures to replace their batteries, thus increasing the hospitals' surgery waiting lists and potentially causing severe health complications to the patients, as previously referenced.

Table 1.1 - Average lifespan of common commercially-available implantable medical devices.

Device	Life span	Ref.
Cardioverter defibrillator	7.1 years	[56]
Cardiac resynchronization therapy defibrillator	5.8 years	[56]
Vagus nerve stimulator	4.9 years	[57]

The previously presented energy drama may be solved by combining three vectors: making devices energy-efficient (low-power electronics), improving the energy storage mechanisms, or using alternative energy capture solutions. Gifting implantable medical devices with wireless powering capabilities would allow for them to be less voluminous, as smaller-capacity batteries, or even no batteries at all, would be required. This would enable the devices to be placed in areas inside of the human body that were previously inaccessible, birthing new applications and therapies. Furthermore, powering the devices from the outside can significantly increase their lifetime and allow for uninterrupted use while eliminating the need for battery replacement procedures.

The implantation depth at which the IMD operates is a key parameter that limits the suitability of wireless power transfer (WPT) technologies to power the device. An example of this was reported by Oxley *et al.* in [58]. They reported an endovascular neural interface for neural recording that does not require craniotomy for implantation, avoiding brain trauma and inflammatory responses (Figure 1.5). This is achieved by guiding the implant to the brain through veins, as cerebral veins lie in sulcal folds. It consists of a stent-electrode array, which takes advantage of the actual knowledge on stent technology to deliver the integrated electrodes into the desired location for chronical measurements.

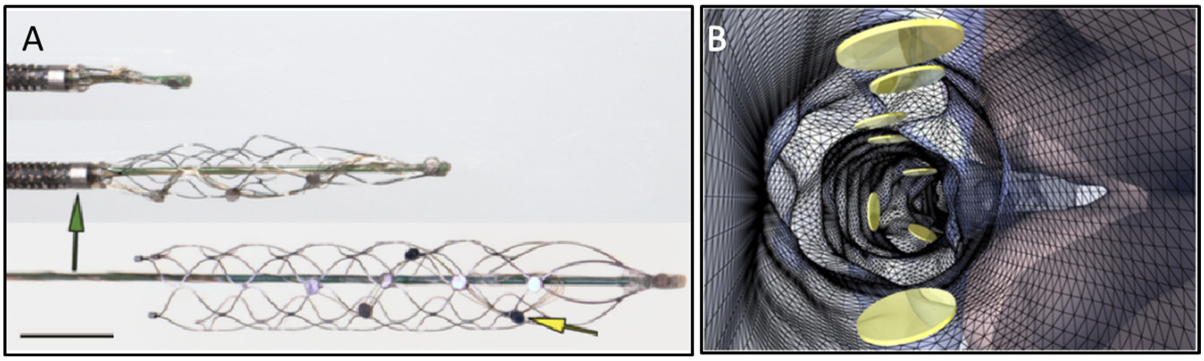

Figure 1.5 A) Stentrode self-expansion with electrodes marked by the yellow arrow. Scale bar, 3 mm. B) Graphical representation of the electrodes placed against the blood vessel's interior walls. Adapted from [58].

This prototype is a novel approach to deep brain electrical signal recording, yet data transmission relies on a wire. Wire fatigue was verified in chronic implantation, which hindered the durability of the implant. The authors have proposed wireless power and data transmission as the safest solution to this issue but stated that wireless technology at the time of developing the prototype was still unsuitable for endovascular approaches. Such a statement is a clear indication that this kind of technology is highly sought after and that research in this field still has a long way to go.

Additionally, the previously presented device is of significant size. Much smaller devices are required for deep implantation outside of blood vessels, as volume availability is scarce. In that case it becomes even harder to develop an effective WPT solution for such a small and deep-implanted IMD.

It is possible to observe a tendency to develop IMDs that are as small and functional as possible in order to enable new applications in locations of the human body inaccessible for larger devices. The literature reveals efforts in the development of extremely small sub-mm IMDs, and fabrication technologies that enable the creation of essential components for miniaturized IMDs have been extensively reported [55], [59]–[62]. The need for these technological advances can be understood by looking into some of the problems tackled by IMDs, such as deep brain stimulation (DBS) and epilepsy.

DBS is a therapy that changed the way brain disorders are studied and treated. It consists of the implantation of electrodes in the brain to deliver precise electrical stimulation to the neurons in order to control their erratic activity. As of 2019, 160 000 patients have undergone DBS therapy. As a research tool, DBS allows scientists to investigate the physiological underpinnings of neural disorders and identify pathological neural activity signatures. Current DBS devices are implanted in locations where the available volume is less restrictive, and the electric current is delivered to the desired location in the brain via a lead. However, according to [63], lead failure was the third most common hardware-related complication registered in the authors' review. Should these devices be small enough to be implanted directly in the site where electrical stimulation is required, this problem would be eliminated. The biggest challenges this technology faces are extending the battery life of devices, miniaturization and integration of wireless technology [64].

Epilepsy is a neurological disease affecting more than 50 million people worldwide that often results in patients having life-threatening seizures that, in 30-40% of the cases, cannot be controlled with medication. Since an episode is characterised by erratic neuronal electrical activity, alternative therapies such as DBS and thermal neuromodulation that can control electrical activity in the neurons are highly sought-after [65]. Epileptic seizure foci occur in random regions of the brain, including deep ones. As such, a practical application would require several stimulators implanted in the brain, forming a sensor-actuator network. Unfortunately, such a solution faces significant technological barriers such as the need for radical miniaturization while still meeting the power requirements of the IMD [32].

Two examples of critical medical challenges have been presented to exemplify how the miniaturization of IMDs is a cornerstone in developing new research and therapy tools and how reliable wireless powering capabilities are a crucial step towards achieving this goal. This conclusion appears to be a consensus within the scientific community, as numerous publications report the need to miniaturize IMDs and the challenges that this effort poses [55], [64], [66]–[69].

1.2.1 Powering challenges of future IMDs

With the reduction of an IMD's volume, its energy efficiency is also expected to increase. For example, a miniaturized 2D sensor with high sensitivity will analyse a smaller tissue or fluid sample, thus requiring less energy to perform its task. On the other hand, a smaller device means less available volume for the receiving transducer, e.g. an antenna or a piezoelectric element, therefore, lower efficiency is expected in these components, which hinders the powering efforts.

In the age of the IoT and sensor networks, each IMD may become highly adapted to a single role, such as monitoring a tiny region of the brain or applying a low-power electrostimulation. Hence, an implant may no longer be a single device, but rather a network of tiny devices operating in sync with each other. In [70], extremely small, sub-mm^3 3D antennas were reported. These are cubic-shaped and hollow; therefore, it is possible to imagine an implant node integrated inside the antenna volume, forming a 500 x 500 x 500 µm^3 sensor or actuator that can be used as part of a network of devices. In this scenario, a method capable of powering all the IMDs simultaneously may be extremely advantageous.

The effort to miniaturise IMDs and make them more efficient is currently far from over and will proceed in the future. Present knowledge indicates that 2D flexible and miniaturised devices will be a reality. Though they're expected to be more efficient than today's devices, how to power them may still be a bottleneck in miniaturisation efforts [71].

1.3 Objectives

The development of new implantable solutions for healthcare is dependent on integration and miniaturisation technologies, which in turn must combine traditional powering solutions with alternative ones, such as WPT. When aiming to wirelessly deliver power to a device placed either in, on, or close to the human body, safety standards must be considered and respected to protect the device's user. Safety thresholds exist to preserve the health of the patients, limiting the amount of power that can be used. Consequently, to deliver more energy to an IMD, simply increasing the transmitted power is not an adequate solution. Other ways to increase the power transfer to an IMD need to be explored.

The objectives of this thesis are presented below.

1. **Identify state-of-the-art IMDs and possible future development trends:**

   A bibliographical search will be conducted for state-of-the-art miniaturized IMDs with alternative powering methods, along with research for emerging technologies that have the potential to enable the IMD of the future.

2. **Study the powering technologies used in state-of-the-art IMDs and select the best for the IMD of the present and the future:**

   Published information regarding the methods used to power the state-of-the-art IMDs will be collected, studied, and discussed to allow the selection of the method that best suits the needs and constraints of present and future IMDs.

3. **Study the influence of the powering solution on the human body:**

   Having identified a WPT method to be developed, the impact of that solution on the human body will be studied to understand, at a biological level, how effects can manifest themselves. Additionally, the safety regulations associated with the chosen WPT technology will be studied.

4. **Identify WPT link parameters that can be engineered to increase the power delivered to the IMD:**

   Knowing how the human body reacts to the propagation of energy, WPT link parameters will be identified by their ability to increase power delivered to the IMD without surpassing the imposed safety limits. Link efficiency will be of minor importance, as the main parameter of interest to this work is the amount of power delivered to the implant.

5. **Develop and validate a prototype of a WPT solution:**

   Having determined what WPT approach to use, how it interacts with the human body and what parameters are worth manipulating, a prototype of a WPT transmitter will be developed. Simulations and experimental setups will be used to demonstrate the proposed method and verify if it is an improvement over traditional WPT links.

In summary, this thesis' objective is to study, propose and validate a multidimensional WPT technique for biomedical electronic devices operating inside the human body capable of outperforming traditional approaches while still respecting safety limits.

1.4 Main contributions

The contributions described in this thesis address the powering solutions available for miniaturised IMDs. It introduces a WPT system that takes advantage of previously unexplored WPT link parameters to deliver more power to IMDs, allowing them to become smaller while keeping up with their power needs. The work presented in this document is a multidisciplinary effort that merges the knowledge from several fields such as: human tissue physiology and electromagnetic (EM) wave propagation, to understand underlying concepts of EM wave interactions with biological tissue (dosimetry); 3D modelling and EM simulation, to numerically assess ideas and possible designs, and to validate experimental results; RF system design, to propose and implement a complex WPT system; and RF measurement techniques to perform the required experiments. In summary, the key contributions of this thesis are:

- Demonstration that the use of multiple transmitters and phase control of RF signals increases the power delivered to an implant without increasing the maximum specific absorption rate (SAR) value;
- Design and development of a fully functional WPT system that employs the findings of this thesis;
- Successful WPT demonstration to a fully functional wireless device inside human body models;
- An extensive and thorough review of alternative powering methods employed by state-of-the-art miniaturized IMDs, which is currently a hot research topic; and
- The theoretical study from multiple sources regarding the interaction of EM waves with biological tissues that is useful to implement WPT links or wireless communication to implantable or wearable devices.

1.4.1 List of publications

The work presented in this thesis contributed to several publications over the years, including two journal papers, one book chapter and four conference papers.

1. H. Dinis, I. Colmiais, and P. M. Mendes, “A multiantenna approach to maximize wireless power transfered to implantable devices,” 2017 *Int. Appl. Comput. Electromagn. Soc. Symp. - Italy, ACES 2017*, 2017.
2. H. Dinis and P. M. Mendes, “Recent Advances on Implantable Wireless Sensor Networks,” *Wirel. Sens. Networks - Insights Innov.*, 2017.
3. H. Dinis, I. Colmiais, and P. M. Mendes, “Extending the limits of wireless power transfer to miniaturized implantable electronic devices,” *Micromachines*, vol. 8, no. 12, 2017.
4. Colmiais, H. Dinis, and P. M. Mendes, “WPT system for implantable devices using a phased array and tracking algorithm for freely moving rats,” *6th IEEE Port. Meet. Bioeng. ENBENG 2019* - Proc., 2019.
5. H. Dinis, I. Colmiais, P. M. Mendes, and S. Member, “Increasing the Miniaturization Limit of Wireless Implantable Devices Through a Multimode Wireless Power Transfer Approach,” MMS 2019 - *IEEE 19th Mediterr. Microw. Symp.*, pp. 2016–2019, 2018.
6. H. Dinis, I. Colmiais, and P. M. Mendes, “Design and validation of a six-antenna WPT system with tracking capabilites for biomedical devices,” *17th IEEE Int. New Circuits Syst. Conf. NEWCAS 2019*, 2019.
7. H. Dinis and P. M. Mendes, “A comprehensive review of powering methods used in state-of-the-art miniaturized implantable electronic devices,” *Biosens. Bioelectron.*, vol. 172, no. October 2020, p. 112781, 2021.

1.5 Thesis outline

In the first chapter, we discuss introductory notes regarding the main drivers pushing for IMD miniaturization. A collection of miniaturized IMDs is presented, and difficulties faced in miniaturization efforts, namely the powering mechanism of such devices, are highlighted. The most recent advances in battery technology that are pertinent to IMDs are briefly approached to demonstrate that alternative powering solutions are still necessary and highly sought-after.

Chapter two contains extensive bibliographical research of state-of-the-art miniaturized IMDs with wireless powering capabilities ranging from energy harvesting to WPT. The basic operation principles of the plentiful alternative powering methods are presented, along with examples of IMDs that resort to them. Finally, a comparison between powering techniques is presented and guidelines to help select which one to adopt are suggested.

Chapter three presents a study of the interaction mechanism between EM waves and biological tissue and its underlying side effects. Here we try to understand the mechanisms behind EM WPT in the human body and identify link parameters that may be manipulated to safely increase the power that can be delivered to the implant.

Chapter four presents the development of a WPT system based on the findings of chapter three. This system intends to use multiple transmitters scattered around the implantation medium to deliver more power to the implant without surpassing SAR limits. Additionally, the system can control the phases of the signals it uses to transmit power to concentrate it in the implant's location.

Chapter five contains the experimental and simulation results that validate the proposed WPT system and demonstrate its usefulness. Power distribution maps inside a human head phantom are presented, along with a demonstration of WPT to a wireless device that circulates inside geometrically accurate human body models.

Finally, chapter six is reserved for the conclusions and presents future work opportunities associated with this research.

1.6 References

[1] E. Katz, *Implantable Bioelectronics*. Weinheim, Germany: Wiley-VCH Verlag GmbH & Co. KGaA, 2014.

[2] W. Greatbatch and C. F. Holmes, "History of implantable devices," *IEEE Eng. Med. Biol. Mag.*, vol. 10, no. 3, pp. 38–41, Sep. 1991.

[3] K. Liu *et al.*, "Stretchable Lithium Metal Anode with Improved Mechanical and Electrochemical Cycling Stability," *Joule*, vol. 2, no. 9, pp. 1857–1865, 2018.

[4] G. Zan *et al.*, "An approaching-theoretical-capacity anode material for aqueous battery: Hollow hexagonal prism Bi2O3 assembled by nanoparticles," *Energy Storage Mater.*, vol. 28, no. December 2019, pp. 82–90, 2020.

[5] Y. H. Joung, "Development of implantable medical devices: From an engineering perspective," *Int. Neurourol. J.*, vol. 17, no. 3, pp. 98–106, 2013.

[6] Acumen Research and Consulting, "Implantable Medical Devices Market (By Product: Dental Implants, Breast Implants, Orthopedic Implants, Cardiovascular Implants, Intraocular Lens, Others) - Global Industry Analysis, Market Size, Opportunities And Forecast, 2019 - 2026," 2019. .

[7] M. H. Ghaed *et al.*, "Circuits for a cubic-millimeter energy-autonomous wireless intraocular pressure

monitor," *IEEE Trans. Circuits Syst. I Regul. Pap.*, vol. 60, no. 12, pp. 3152–3162, 2013.

[8] G. Chitnis, T. Maleki, B. Samuels, L. B. Cantor, and B. Ziaie, "A minimally invasive implantable wireless pressure sensor for continuous IOP monitoring," *IEEE Trans. Biomed. Eng.*, vol. 60, no. 1, pp. 250–256, 2013.

[9] M. H. M. Kouhani, A. Weber, and W. Li, "Wireless intraocular pressure sensor using stretchable variable inductor," *Proc. IEEE Int. Conf. Micro Electro Mech. Syst.*, pp. 557–560, 2017.

[10] A. Donida *et al.*, "A 0.036mbar circadian and cardiac intraocular pressure sensor for smart implantable lens," in *2015 IEEE International Solid-State Circuits Conference - (ISSCC) Digest of Technical Papers*, 2015, vol. 58, pp. 1–3.

[11] A. Agarwal, A. Shapero, D. Rodger, M. Humayun, Y. C. Tai, and A. Emami, "A wireless, low-drift, implantable intraocular pressure sensor with parylene-on-oil encapsulation," *2018 IEEE Cust. Integr. Circuits Conf. CICC 2018*, pp. 1–4, 2018.

[12] J. C. Chiou *et al.*, "Toward a Wirelessly Powered On-Lens Intraocular Pressure Monitoring System," *IEEE J. Biomed. Heal. Informatics*, vol. 20, no. 5, pp. 1216–1224, 2016.

[13] Y.-P. Chen *et al.*, "An Injectable 64 nW ECG Mixed-Signal SoC in 65 nm for Arrhythmia Monitoring," *IEEE J. Solid-State Circuits*, vol. 50, no. 1, pp. 375–390, Jan. 2015.

[14] D. Seo *et al.*, "Wireless Recording in the Peripheral Nervous System with Ultrasonic Neural Dust," *Neuron*, vol. 91, no. 3, pp. 529–539, 2016.

[15] R. Muller *et al.*, "A Minimally Invasive 64-Channel Wireless μECoG Implant," *IEEE J. Solid-State Circuits*, vol. 50, no. 1, pp. 344–359, 2015.

[16] S. Majerus, I. Makovey, H. Zhui, W. Ko, and M. S. Damaser, "Wireless implantable pressure monitor for conditional bladder neuromodulation," in *2015 IEEE Biomedical Circuits and Systems Conference (BioCAS)*, 2015, pp. 1–4.

[17] S. Vaddiraju, M. Kastellorizios, A. Legassey, D. Burgess, F. Jain, and F. Papadimitrakopoulos, "Needle-implantable, wireless biosensor for continuous glucose monitoring," in *2015 IEEE 12th International Conference on Wearable and Implantable Body Sensor Networks (BSN)*, 2015, pp. 1–5.

[18] M. P. Christiansen *et al.*, "A Prospective Multicenter Evaluation of the Accuracy of a Novel Implanted Continuous Glucose Sensor: PRECISE II," *Diabetes Technol. Ther.*, vol. 20, no. 3, pp. 197–206, 2018.

[19] A. Aldaoud, C. Laurenson, F. Rivet, M. R. Yuce, and J. Redouté, "Design of an Inductively Powered Implantable Wireless Blood Pressure Sensing Interface using Capacitive Coupling," *IEEE/ASME Trans. Mechatronics*, vol. 20, no. 1, pp. 487–491, 2015.

[20] J. Park, J.-K. Kim, S. Patil, J.-K. Park, S. Park, and D.-W. Lee, "A Wireless Pressure Sensor Integrated with a Biodegradable Polymer Stent for Biomedical Applications," *Sensors*, vol. 16, no. 6, p. 809, Jun. 2016.

[21] X. Cheng *et al.*, "Implantable and self-powered blood pressure monitoring based on a piezoelectric thinfilm:

Simulated, in vitro and in vivo studies," *Nano Energy*, vol. 22, pp. 453–460, 2016.

[22] K. Meng *et al.*, "Flexible Weaving Constructed Self-Powered Pressure Sensor Enabling Continuous Diagnosis of Cardiovascular Disease and Measurement of Cuffless Blood Pressure," *Adv. Funct. Mater.*, vol. 29, no. 5, p. 1806388, Dec. 2018.

[23] K. Meng *et al.*, "A Wireless Textile-Based Sensor System for Self-Powered Personalized Health Care," *Matter*, vol. 2, no. 4, pp. 896–907, Apr. 2020.

[24] P. Gou *et al.*, "Carbon Nanotube Chemiresistor for Wireless pH Sensing," *Sci. Rep.*, vol. 4, no. 1, p. 4468, May 2015.

[25] M. Farella *et al.*, "Simultaneous wireless assessment of intra-oral pH and temperature," *J. Dent.*, vol. 51, pp. 49–55, 2016.

[26] M. H. Behfar, T. Björninen, E. Moradi, L. Sydänheimo, and L. Ukkonen, "Biotelemetric Wireless Intracranial Pressure Monitoring: An In Vitro Study," *Int. J. Antennas Propag.*, vol. 2015, pp. 1–10, Apr. 2015.

[27] S. Kang *et al.*, "Bioresorbable silicon electronic sensors for the brain," *Nature*, vol. 530, no. 7588, pp. 71–76, 2016.

[28] E. Y. Chow, S. P. Sanghani, and M. M. Morris, "Wireless MEMS-based implantable medical devices for cardiology," in *Wireless MEMS Networks and Applications*, Elsevier, 2017, pp. 77–100.

[29] A. Khalifa *et al.*, "The Microbead: A 0.009 mm3 Implantable Wireless Neural Stimulator," *IEEE Trans. Biomed. Circuits Syst.*, vol. 13, no. 5, pp. 971–985, 2019.

[30] X.-H. Qian *et al.*, " Design and In Vivo Verification of a CMOS Bone-Guided Cochlear Implant Microsystem ," *IEEE Trans. Biomed. Eng.*, vol. 66, no. 11, pp. 3156–3167, 2019.

[31] K. Tomioka, K. Toyoda, T. Ishizaki, T. Noda, J. Ohta, and M. Kimura, "Retinal Prosthesis Using Thin-Film Devices on a Transparent Substrate and Wireless Power Transfer," *IEEE Trans. Electron Devices*, vol. 67, no. 2, pp. 529–534, 2020.

[32] K. L. Montgomery *et al.*, "Wirelessly powered, fully internal optogenetics for brain, spinal and peripheral circuits in mice," *Nat. Methods*, vol. 12, no. 10, pp. 969–974, 2015.

[33] J. S. Ho *et al.*, "Wireless power transfer to deep-tissue microimplants," *Proc. Natl. Acad. Sci.*, vol. 111, no. 22, pp. 7974–7979, Jun. 2014.

[34] Museum of Health Care at Kingston, "Chardack-Greatbatch pacemaker." [Online]. Available: https://mhc.andornot.com/en/permalink/artifact84. [Accessed: 26-Mar-2020].

[35] A. Kiourti and K. S. Nikita, "A review of in-body biotelemetry devices: Implantables, ingestibles, and injectables," *IEEE Trans. Biomed. Eng.*, vol. 64, no. 7, pp. 1422–1430, 2017.

[36] P. Yeon, M. G. Kim, O. Brand, and M. Ghoovanloo, "Optimal design of passive resonating wireless sensors for wearable and implantable devices," *IEEE Sens. J.*, vol. 19, no. 17, pp. 7460–7470, 2019.

[37] Q. A. Huang, L. Dong, and L. F. Wang, "LC Passive Wireless Sensors Toward a Wireless Sensing Platform:

Status, Prospects, and Challenges," *J. Microelectromechanical Syst.*, vol. 25, no. 5, pp. 822–841, 2016.

[38] W. Jia *et al.*, "Passive Implantable Wireless Intracranial Pressure Monitoring Based on Near Field Communication," in *2019 IEEE Biomedical Circuits and Systems Conference (BioCAS)*, 2019, no. 61661166010, pp. 1–4.

[39] S. S. Karipott, B. D. Nelson, R. E. Guldberg, and K. G. Ong, "Clinical potential of implantable wireless sensors for orthopedic treatments," *Expert Rev. Med. Devices*, vol. 15, no. 4, pp. 255–264, 2018.

[40] A. Ben Amar, A. B. Kouki, and H. Cao, "Power approaches for implantable medical devices," *Sensors (Switzerland)*, vol. 15, no. 11, pp. 28889–28914, 2015.

[41] B. Shi, Z. Li, and Y. Fan, "Implantable Energy-Harvesting Devices," *Adv. Mater.*, vol. 30, no. 44, p. 1801511, Nov. 2018.

[42] K. Agarwal, R. Jegadeesan, Y. X. Guo, and N. V. Thakor, "Wireless Power Transfer Strategies for Implantable Bioelectronics," *IEEE Rev. Biomed. Eng.*, vol. 10, no. c, pp. 136–161, 2017.

[43] L. Yin *et al.*, "Materials, designs, and operational characteristics for fully biodegradable primary batteries," *Adv. Mater.*, vol. 26, no. 23, pp. 3879–3884, 2014.

[44] P. Zhang *et al.*, "Zn-Ion Hybrid Micro-Supercapacitors with Ultrahigh Areal Energy Density and Long-Term Durability," *Adv. Mater.*, vol. 31, no. 3, p. 1806005, Jan. 2019.

[45] W. He, C. Wang, H. Li, X. Deng, X. Xu, and T. Zhai, "Ultrathin and Porous Ni 3 S 2 /CoNi 2 S 4 3D-Network Structure for Superhigh Energy Density Asymmetric Supercapacitors," *Adv. Energy Mater.*, vol. 7, no. 21, p. 1700983, Nov. 2017.

[46] C. Yue, J. Li, and L. Lin, "Fabrication of Si-based three-dimensional microbatteries: A review," *Front. Mech. Eng.*, vol. 12, no. 4, pp. 459–476, 2017.

[47] J. I. Hur, L. C. Smith, and B. Dunn, "High Areal Energy Density 3D Lithium-Ion Microbatteries," *Joule*, vol. 2, no. 6, pp. 1187–1201, 2018.

[48] K. Sun, T. S. Wei, B. Y. Ahn, J. Y. Seo, S. J. Dillon, and J. A. Lewis, "3D printing of interdigitated Li-ion microbattery architectures," *Adv. Mater.*, vol. 25, no. 33, pp. 4539–4543, 2013.

[49] D. Qi, Y. Liu, Z. Liu, L. Zhang, and X. Chen, "Design of Architectures and Materials in In-Plane Micro-supercapacitors: Current Status and Future Challenges," *Adv. Mater.*, vol. 29, no. 5, p. 1602802, Feb. 2017.

[50] H. Li and J. Liang, "Recent Development of Printed Micro-Supercapacitors: Printable Materials, Printing Technologies, and Perspectives," *Adv. Mater.*, vol. 32, no. 3, p. 1805864, Jan. 2020.

[51] S. Li, Z. P. Guo, C. Y. Wang, G. G. Wallace, and H. K. Liu, "Flexible cellulose based polypyrrole–multiwalled carbon nanotube films for bio-compatible zinc batteries activated by simulated body fluids," *J. Mater. Chem. A*, vol. 1, no. 45, pp. 14300–14305, 2013.

[52] W. Lai *et al.*, "High performance, environmentally benign and integratable Zn//MnO2 microbatteries," *J.*

Mater. Chem. A, vol. 6, no. 9, pp. 3933–3940, 2018.

[53] M. Koo *et al.*, “Bendable inorganic thin-film battery for fully flexible electronic systems,” *Nano Lett.*, vol. 12, no. 9, pp. 4810–4816, 2012.

[54] L. Li *et al.*, “High-Performance Solid-State Supercapacitors and Microsupercapacitors Derived from Printable Graphene Inks,” *Adv. Energy Mater.*, vol. 6, no. 20, p. 1600909, Oct. 2016.

[55] D. Karnaushenko, T. Kang, V. K. Bandari, F. Zhu, and O. G. Schmidt, “3D Self-Assembled Microelectronic Devices: Concepts, Materials, Applications,” *Adv. Mater.*, vol. 32, no. 15, p. 1902994, Apr. 2020.

[56] F. Gadler *et al.*, “Economic impact of longer battery life of cardiac resynchronization therapy defibrillators in Sweden,” *Clin. Outcomes Res.*, vol. 8, pp. 657–666, 2016.

[57] J. Couch, A. Gilman, and W. Doyle, “Long-term Expectations of Vagus Nerve Stimulation: A Look at Battery Replacement and Revision Surgery,” vol. 78, no. 1, pp. 42–46, 2016.

[58] T. J. Oxley *et al.*, “Minimally invasive endovascular stent-electrode array for high-fidelity, chronic recordings of cortical neural activity,” *Nat. Biotechnol.*, vol. 34, no. 3, pp. 320–327, 2016.

[59] P. Anacleto, “Self-Folding 3D Micro Antennas For Implantable Medical Devices,” University of Minho, 2016.

[60] J. Fernandes, “Design, fabrication and integration of 3D micro-structures using self-folding techniques for ultra-miniaturization of smart microsystems,” University of Minho, 2019.

[61] P. M. Mendes, S. Sinaga, A. Polyakov, M. Bartek, J. N. Burghartz, and J. H. Correia, “Wafer-level integration of on-chip antennas and RF passives using high-resistivity polysilicon substrate technology,” in *2004 Proceedings. 54th Electronic Components and Technology Conference (IEEE Cat. No.04CH37546)*, 2004, vol. 2, pp. 1879–1884.

[62] P. M. Mendes, A. Polyakov, M. Bartek, J. N. Burghartz, and J. H. Correia, “Integrated chip-size antennas for wireless microsystems: Fabrication and design considerations,” *Sensors Actuators A Phys.*, vol. 125, no. 2, pp. 217–222, Jan. 2006.

[63] O. Jitkritsadakul, R. Bhidayasiri, S. K. Kalia, M. Hodaie, A. M. Lozano, and A. Fasano, “Systematic review of hardware-related complications of Deep Brain Stimulation: Do new indications pose an increased risk?,” *Brain Stimul.*, vol. 10, no. 5, pp. 967–976, 2017.

[64] A. M. Lozano *et al.*, “Deep brain stimulation: current challenges and future directions,” *Nat. Rev. Neurol.*, vol. 15, no. 3, pp. 148–160, 2019.

[65] J. Fernandes *et al.*, “Design and Performance Assessment of a Solid-State Microcooler for Thermal Neuromodulation,” *Micromachines*, vol. 9, no. 2, p. 47, 2018.

[66] W. Khan, Y. Jia, F. Madi, A. Weber, M. Ghovanloo, and W. Li, “Inductively coupled, mm-sized, single channel optical neuro-stimulator with intensity enhancer,” *Microsystems Nanoeng.*, vol. 5, no. 1, p. 23, Dec. 2019.

[67] P. Feng, P. Yeon, Y. Cheng, M. Ghovanloo, and T. G. Constandinou, “Chip-Scale Coils for Millimeter-Sized

Bio-Implants," *IEEE Trans. Biomed. Circuits Syst.*, vol. 12, no. 5, pp. 1088–1099, 2018.

[68] M. Zaeimbashi *et al.*, "NanoNeuroRFID: A Wireless Implantable Device Based on Magnetoelectric Antennas," *IEEE J. Electromagn. RF Microwaves Med. Biol.*, vol. 3, no. 3, pp. 206–215, 2019.

[69] T. C. Chang, M. J. Weber, J. Charthad, S. Baltsavias, and A. Arbabian, "End-to-end design of efficient ultrasonic power links for scaling towards submillimeter implantable receivers," *IEEE Trans. Biomed. Circuits Syst.*, vol. 12, no. 5, pp. 1100–1111, 2018.

[70] P. Anacleto, H. Dinis, J. Fernandes, and P. M. Mendes, "Design and Characterization of 3D Self-folded Micro Antennas for Implantable Microdevices," *IEEE Trans. Antennas Propag.*, vol. 68, no. 3, pp. 2031–2039, 2019.

[71] H. Dinis and P. M. Mendes, "A comprehensive review of powering methods used in state-of-the-art miniaturized implantable electronic devices," *Biosens. Bioelectron.*, vol. 172, no. October 2020, p. 112781, 2021.

CHAPTER 2 STATE-OF-THE-ART

Ever since Feynman's "There's Plenty of Room at the Bottom" lecture, in 1959 [1], researchers predicted that smart, integrated and miniaturized structures would be enabled by advances in materials science and micro and nanotechnologies. The development of smaller and smarter IMDs is a consequence of such advancements, and of a unique cooperation between industrial scientists and engineers, academia and medical professionals. It has led to the development of many different devices that save lives and improve the quality of life of countless patients suffering from various conditions.

This chapter presents a literature review of state-of-the-art IMDs with wireless power capabilities, ranging from energy harvesters to dedicated WPT sources. Followingly, state-of-the-art technologies which will be the foundation of the IMD of the future are presented.

2.1 Powering an implantable medical device

The urge to research new and reliable powering solutions for implantable devices to increase their lifespan and reduce their volume is evident. The interest in this field is proven by the amount of publications made available year after year. These solutions can be distinguished into two main groups: energy harvesting (EH), where the device gathers energy from the environment, thus being completely self-sustainable as long as the environment remains constant, and WPT, where there is a dedicated external source of energy that the IMD captures and uses. Figure 2.1 lists the different groups and subgroups of the most prominent alternative powering methods employed by IMDs found in the literature.

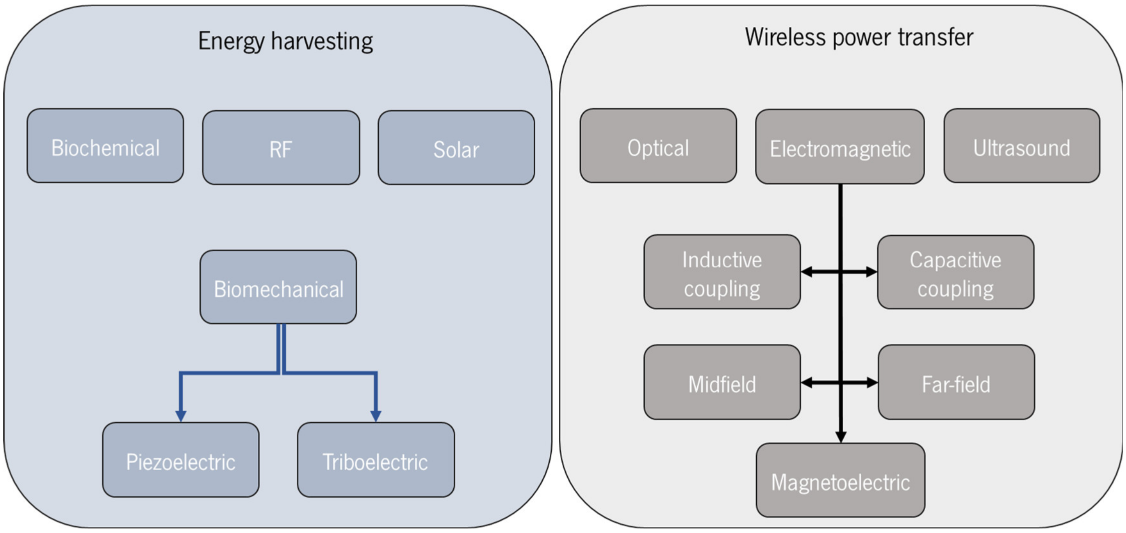

Figure 2.1 –Different powering methods that have been employed by state-of-the-art IMDs to replace batteries.

2.2 Energy harvesting

EH techniques consist of harvesting useful amounts of energy from the environment to power a device or charge a battery, having the potential to provide power to biomedical devices since they could yield unlimited energy, drastically increasing the devices' lifespan. However, harvesting useful amounts of energy from the environment can be challenging. The amount of available energy is often volatile and very limited, which imposes the need of special power management circuitry [2], [3]. Nevertheless, due to the constant reduction of electronic circuits' power demands, research in the field of EH is of high interest and the number of publications related to this topic increases every year [4].

Considering the most promising technologies, EH can be distinguished into four types: biomechanical, biochemical, radiofrequency (RF) and solar, and examples are shown in Figure 2.2.

Besides the EH methods mentioned above, other EH technologies such as thermoelectric (TE) EH have been reported. TE EH resorts to a Peltier device, which uses the Seebeck effect to generate electricity from a thermal gradient. Inside the human body, we can find small thermal gradients under the skin, as the skin's surface is colder due to exposure to the environment. Thermal energy harvesters have been reported in the literature mainly for wearable devices [5]–[7], but no miniaturized IMDs that employ this powering method were found. Additionally, hybrid solutions capable of harvesting solar and mechanical energy through fabrics have been proposed [8].

2.2.1 Biomechanical energy harvesting

The human body produces biomechanical energy in multiple ways, e.g. muscle movements, heartbeats, breathing, and deformation from large blood vessels, such as the aorta. Each of these actions generates a certain amount of power, and energy harvesters extract a fraction of this power for an IMD [16]. For example, blood flow has been used in [17] to drive an electromagnetic generator that could generate around 1 mW of electric power by using around 10% of the heart's hydraulic power output.

Piezoelectric materials produce electrical energy through mechanical deformation. They have been used in [9] to harvest energy from motions of the heart, lung and diaphragm (Figure 2.2 A) and achieved a power density of 0.18 $\mu W/cm^2$ in the heart. In [10], 3D piezoelectric polymers (Figure 2.2 B) were developed to harvest vibrational energy from the rat's movement and were implanted in its hind leg and generated voltages up to 2 mV.

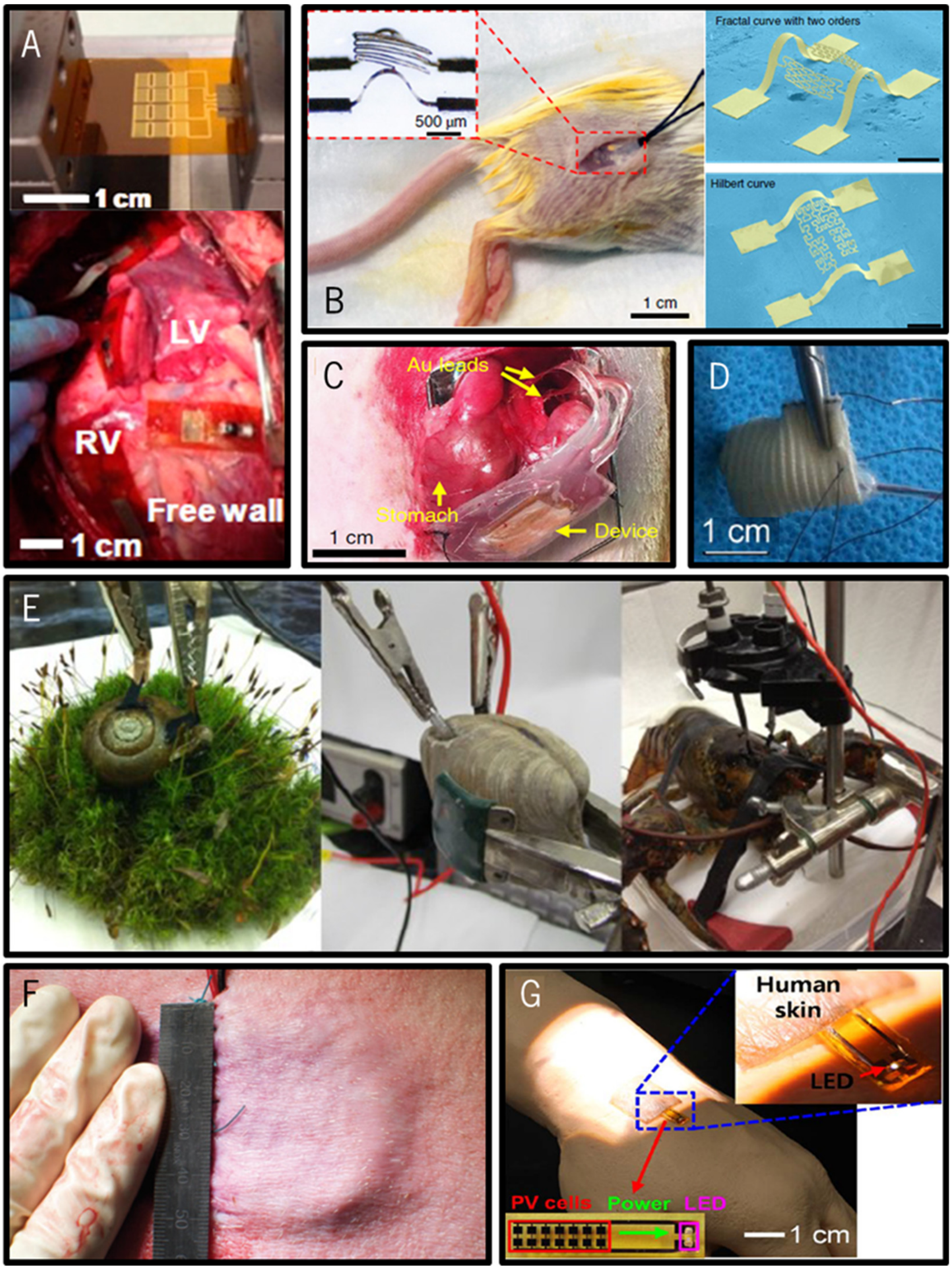

Figure 2.2 – Examples of energy harvesting solutions for IMDs. A) Piezoelectric generator in bending tests (top) and attached to a bovine heart (bottom) [9]. B) 3D polymer piezoelectric generator implanted in a rat (left) and additional designs (right). Scale bar 0.5 mm [10]. C) Triboeletric nanogenerator implanted in a rat stomach to power a vagus nerve stimulator for appetite control [11]. D) Glucose biofuel cell wrapped in a Dacron bag before implantation [12]. E) Glucose biofuel cells implanted in a snail (left), a clam (centre) and a lobster (right) [13]. F) Solar cell implanted in a pig to power a pacemaker [14]. G) Solar cell under an excerpt of human skin powering an LED [15].

Triboelectric (TrE) energy harvesters convert mechanical energy into electricity by the triboelectric effect and electrostatic induction. They are, thus, used to harvest biomechanical energy. In [18], a biodegradable TrE nanogenerator for the heart generated, *in vitro*, 3.2 μW/cm^2, while in [19] a power density of 11 μW/cm^2 was reported. In [20], 0.8 μW/cm^2 were harvested from a rat's breathing. Stomach movements were also used to power a vagus nerve stimulator for appetite control through TrE materials (Figure 2.2 C) with an achieved power density of around 40 μW/cm^2 [11].

2.2.2 Biochemical energy harvesting

Biological tissue requires energy to function, and glucose is an abundant fuel in living things. Enzyme-modified electrodes can be used to oxidize glucose or reduce oxygen to generate energy for IMDs. As fuels are naturally replenished by the organism, it is a potentially inexhaustible source of energy. The literature shows several examples of biofuel cells in diverse organisms such as rats (Figure 2.2 D) [12], cockroaches [21], snails, clams, and lobsters (Figure 2.2 E) [13], [22]. The rat-implanted biofuel cell achieved the highest power density, 193.5 μW/cm^2.

2.2.3 Solar energy

Solar energy is abundant and clean, and solar cell technology has been in development for a long time. Researchers have tried to use solar energy to power IMDs [23]. In [14] a solar cell implanted below 3 mm of skin achieved a 3500 μW/cm^2 power density and powered a pacemaker in a pig, and in [15] a reported power density of 8000 μW/cm^2 was achieved with 1.5 mm of human skin placed on top of the solar cell (Figure 2.2 G).

Very high power densities can be achieved with solar harvesters, but these are large devices (in the order of the square-centimetre) and, since power density decreases abruptly when the implantation depth increases [14], they require superficial implantation.

2.2.4 Radiofrequency energy harvesting

RF EH consists of harnessing EM waves that exist in the environment, generated by communication towers, for example. These waves have the potential to provide power for electronic devices. The quantity of available radiation, the efficiency of the power conversion system and the device's size constraints dictate whether this method suffices in powering a given application. Power densities in the range of

0.1-80 nW/cm^2 are available in the environment from mobile communication sources [24] which would be further attenuated by the air-skin interface and then by tissue propagation. Even though technological advances are constantly being made, typical ambient RF power densities cause some uncertainty about this powering method's suitability for IMDs.

2.3 Wireless power transfer

EH technologies are often incapable of providing the power levels that most IMDs require and, as such, dedicated power sources become a necessity. WPT technology has established itself as a reliable technology for powering IMDs, with inductive coupling being the most mature and accepted method. Nonetheless, as IMD miniaturization efforts progress, the need for new and improved powering schemes becomes evident [25]. The following sections report on a plethora of WPT methods that have been employed in state-of-the-art IMDs presented in the academic bibliography. As such, the devices that follow were selected to integrate this review based on their wireless powering mechanism, small size, full implantability and overall novelty and level of scientific breakthrough.

2.3.1 Inductive coupling

The near field is the region closest to an EM radiation source, and it is defined with the following equation:

$$\mathrm{NF} < \frac{2\mathrm{d}^2}{\lambda} \tag{2.1}$$

where d is the maximum linear dimension of the antenna and λ is the wavelength of the EM wave. In this region, it is possible to implement two WPT techniques: inductive coupling and capacitive coupling.

Inductive coupling (IC) is the oldest and most established WPT method, with proven results in FDA-approved implants. IC is based in electromagnetic induction, where a time-varying magnetic field generated in a transmission coil induces an electromotive force in a receiving coil, as represented in Figure 2.3.

The induced electromagnetic field ε at RX is given by:

$$\varepsilon = -\frac{d}{dt}\int_{\Sigma} \vec{B}\,.\,d\vec{A} \tag{2.2}$$

where Σ is the surface bounded by the RX, $\vec{B}$ is the magnetic flux density through RX and $d\vec{A}$ is the area vector element of surface Σ [26].

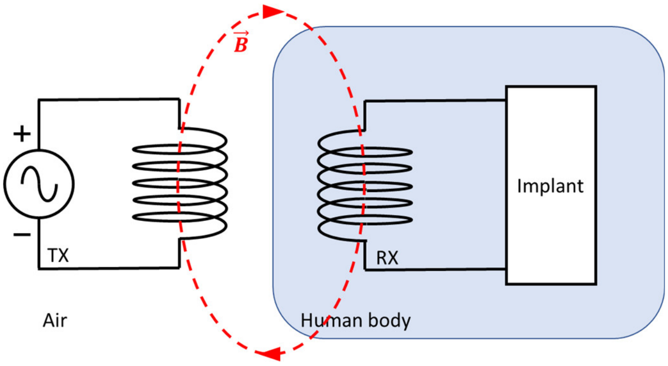

Figure 2.3 -Simplified schematic of an IC WPT method. An AC source in the TX side causes a current to flow through the TX coil. Consequently, a time-varying magnetic field **B** is generated by that coil which induces a current in the RX coil through electromotive forces, thus generating power for the implant.

From (2.2) it is possible to state that the amount of power transferred to the implant depends on the intensity of the magnetic field produced by the TX coil that reaches the RX coil. It can be improved by increasing the TX current, reducing the distance between the TX and RX coils, and guaranteeing proper alignment between the coils. Furthermore, increasing the field's frequency will generate a higher output in the implant's RX coil [26].

In [27] two leadless pacemakers were proposed. These devices (Figure 2.4 A) have coils fabricated in flexible polyimide with an area of 121 mm^2. One of them is tuned for 13.56 MHz IC WPT, while the other is tuned for 40.68 MHz, which achieve efficiencies of 0.03% and 0.005%, respectively, when 5 cm away from the TX coil. Each device was placed in a ventricle of a pig's heart and, due to their different WPT frequencies, the authors could select which one to activate and achieved biventricular pacing.

In [28] a wireless platform for local tissue oximetry through optoelectronics was reported (Figure 2.4 C). The device's coil has an area of 90 mm^2 and it is part of a polyimide substrate. It can receive 12 mW when placed 30 mm away from the TX coil with an efficiency of 0.3%. The operation of the IMD was verified in a rat model.

In [29] a mm-sized glucose sensor for artificial pancreas applications was reported (Figure 2.4 D). The device communicates to and is powered by a wearable transmitter at 900 MHz. A 1.8 mm^2 coil surrounding the rest of the device exhibits an efficiency of 0.1% at an implantation depth of 1.5 mm.

In [30], a 0.009 mm^3 neural stimulator, called the Microbead, was presented (Figure 2.4 E). The extremely small volume of this device allows for implantation with a 22G needle, and it has been shown to elicit EMG responses in a rat model. The CMOS RX coil has an area of 0.1 mm^2 and it can receive 55.5 μW at 1180 MHz with an efficiency of 0.002% when implanted 6.6 mm away from the TX coil.

In [31] the authors presented a small and lightweight optofluidic cuff system for pharmacological neuromodulation. This device is comprised of drug delivery and light stimulation capabilities which, together, achieved neuromodulation in a live rat. The device was implanted in a rat at a depth of 30 mm, and it was powered by a 13.56 MHz RF signal. The RX coil is wound around the device and has an area of 78.5 mm^2, and the device receives 15 mW from the TX coil.

In [32], an optogenetic stimulator is presented. Its coil has an area of 2 mm^2 and it was implanted in a rat. But, unlike conventional IC systems, there was no coil close to the IMD. Instead, the cage floor had a lattice of coils that coupled EM energy through the rat's tissue and into the implant. At 1.5 GHz, the IMD received an average of 10.65 mW from the transmitter with an efficiency of 0.33%.

Inductive coupling has been the backbone of WPT mechanisms for many years, allowing for high power levels to be delivered to devices located in biological tissue. However, exponential field decay and the influence of misalignments in link efficiency are limitations that may restrict the use of this technology in some applications.

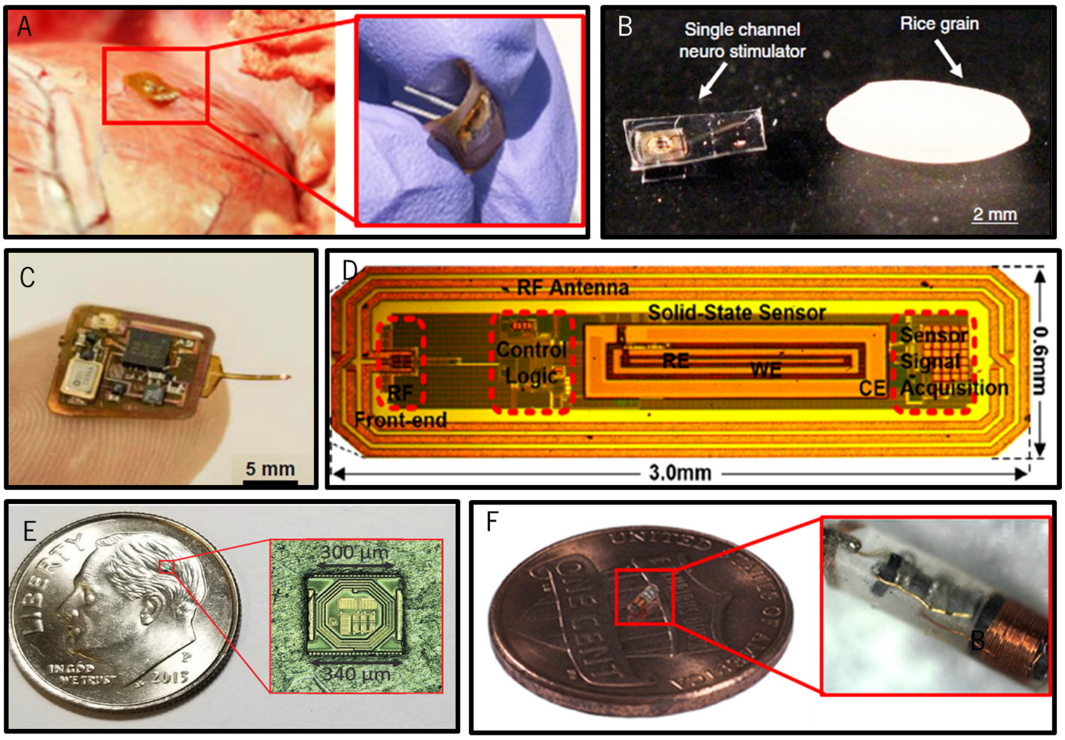

Figure 2.4 -Small IMDs powered with IC WPT. A) Leadless pacemaker implanted in a pig's heart. Inset: detailed view of the device displaying its flexibility and the electrodes (device size: 11x11 mm^2) [27].B) mm-sized neural stimulator [33]. C) Optoelectronic subdermal implant for tissue oximetry monitoring [28]. D) Needle-injectable glucose monitor [29]. E) Microbead 0.009 mm^3 neural stimulator [30]. F) A 0.45 mm^3 neural stimulator [34].

2.3.2 Capacitive coupling

Capacitive coupling (CC) is the counterpart to IC, as it is based on the electric field coupling between two conductors that form the forward and reverse current paths. WPT across the tissue layers occurs when a second pair of conductors that form the RX part of the system are placed close to the TX pair. In this scenario, two capacitors are formed between the RX and TX coil pairs, and displacement and conduction currents are drawn from the AC source. Conduction current occurs in the tissue due to the electric field generated between the plates and should be minimized as it translates into losses [26], [35]. An illustration of CC WPT is provided in Figure 2.5.

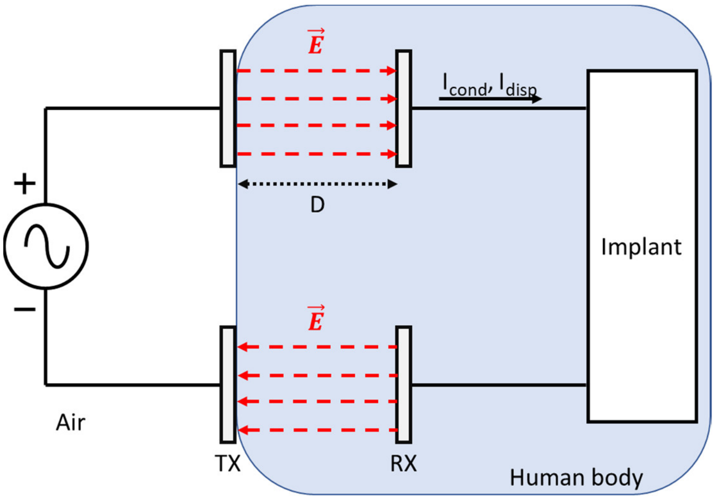

Figure 2.5 - Simplified representation of the CC WPT method. The TX conductor pair and the RX conductor pair form capacitors through which an AC displacement current can flow and power the IMD [26].

Conduction current and displacement current are given by the following equations, respectively:

$$\mathrm{I_{disp}} = \varepsilon_0 \varepsilon_\mathrm{r}(\omega)\mathrm{A}\frac{\partial \vec{\mathrm{E}}}{\partial \mathrm{t}} \tag{2.3}$$

$$\mathrm{I_{cond}} = \frac{\mathrm{V(t)}\sigma(\omega)\mathrm{A}}{\mathrm{D}} \tag{2.4}$$

where ε_0 is the permittivity of free space, $\varepsilon_r(\omega)$ and $\sigma(\omega)$ are the frequency-dependent relative permittivity and conductivity of the biological tissue located between the RX and TX plates. These plates have areas of A and are separated by distance D [26].

From (2.3) and (2.4) it is possible to see that the power transfer can be improved by increasing the electric field strength (either by increasing the transmitter's voltage or reducing the TX-RX distance D), by increasing the operating frequency, and by increasing the area A of the conductor plates.

In [36] CC technology is tested as the power delivery method to an IMD using a metal stent as the receiving electrode pair. The authors reported efficiencies of 2.6% at 260 MHz for an implantation depth of 15 mm inside muscle tissue which resulted in a total of around 1.4 mW of power at the implant. The RX stent (Figure 2.6 A) is 83 mm long and has a 4 mm diameter.

In [35] flexible patches for CC WPT are presented (Figure 2.6 B). Three different RX patch dimensions have been studied, but here only the smaller one (20x10 mm^2) is considered. It achieves its maximum efficiency of 35% at 130 MHz and an implantation depth of 2 mm for a total patch area of 400 mm^2 where the separation between RX patches still needs to be accounted for. The power delivered with this link was 90 mW when a non-human primate model was used for RX implantation under the skin.

In [37] 400 mm^2 patches for IMD CC are reported (Figure 2.6 C). The devices were tested in beef with a TX and RX separation of 2 mm. At 120 kHz the link achieved an efficiency of 10%, delivering 75 mW to the RX load. The total area of the RX is 800 mm^2 without accounting for RX plate distance.

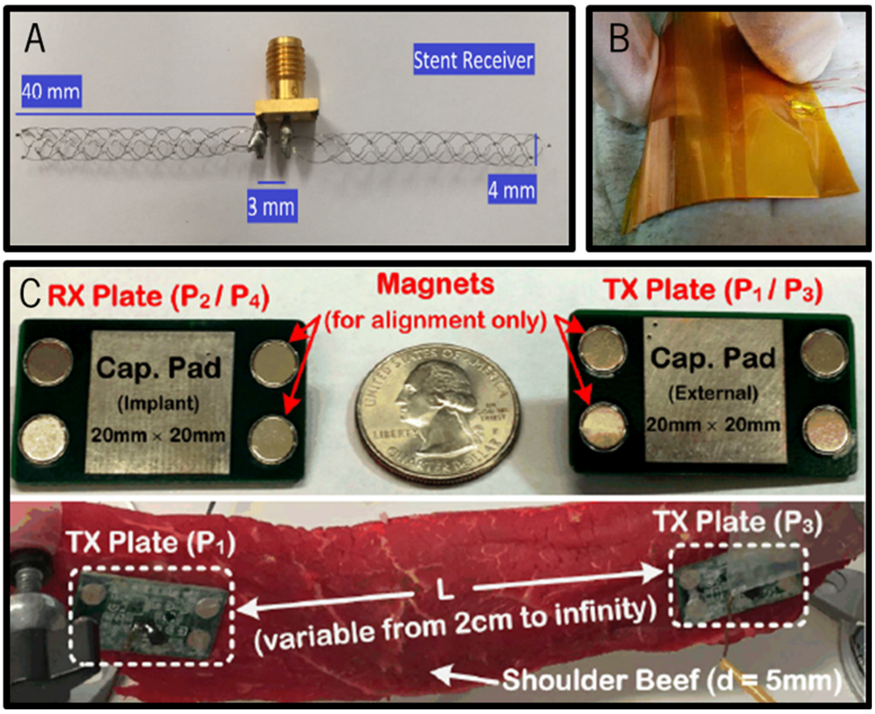

Figure 2.6 – Examples of capacitive coupling devices reported in the literature. A) Stent used as RX conductors [36]. B) Flexible CC patches [35]. C) TX and RX patches used for CC WPT (top) and layout of the TX patches in beef model [37].

Capacitive coupling WPT methods have received increased attention in the last years, and it is a promising technology, although for a restricted set of situations. Large receiver dimensions pose the main obstacle for implementing of this technology to its use in miniaturized IMDs. Furthermore, the fact that it relies on electric fields makes it susceptible to breaking SAR limits, and extreme care needs to be taken when designing a CC WPT link.

2.3.3 Midfield

The near field's exponential decay may render IC unsuitable for powering a miniaturized device placed deep in the body. According to [38], power transfer in the midfield (MF) region can surpass the challenges mentioned above. The MF region, located around a wavelength away from the source, allows power flow lines to be manipulated with an interference, focusing them in a specific spot [39]. This method builds on the limitations of IC, and achieves better efficiencies powering miniature IMDs at high implantation depths by combining the near-field inductive and the far-field radiative modes of a transmitter at the low-GHz frequency range [26]. Figure 2.7 A exemplifies a midfield WPT for a cardiac IMD and demonstrates the magnetic field coupling with air and tissue, where the field tends to concentrate on the implant. The interference that creates this field pattern is presented in Figure 2.7 B.

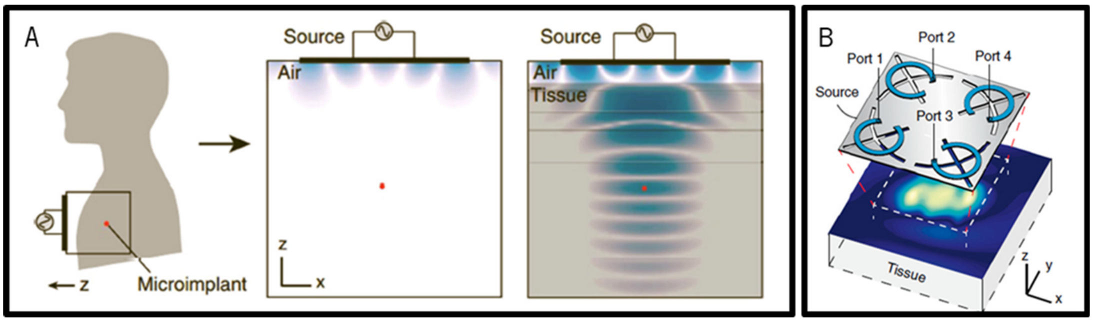

Figure 2.7 – A) Midfield powering scheme of a microimplant placed in the heart (left). Magnetic field distribution in air (center) and tissue (right). B) Patterned plate responsible for the interference that shapes the magnetic field distribution inside the tissue [38].

In [39] a miniaturized device with a coil, an RF-DC converter and an LED was designed to experimentally validate the power transfer efficiency (Figure 2.8 A). After encapsulation, it had a 12 mm^3 volume. With 800 mW output from the phased surface, 0.45 mW were delivered to the device when it was implanted 4.2 cm deep into multilayered porcine tissue, corresponding to an efficiency of 0.056%.

In [38] a catheter-implantable wireless cardiac pacing device (Figure 2.8 B) is presented. It has a cylindrical shape with a diameter of 2 mm, 3.5 mm height, and weighs 70 mg. It consists of a power receiving coil, RF-DC converter, electrodes, and an IC for pulse control. The cardiac pacing device was inserted into a rabbit heart as shown on the right side of Figure 2.8 B and achieved cardiac pacing. A probe to measure the MF WPT link efficiency was also developed by the authors. Its coil had a diameter of 1 mm and, when implanted 5 cm deep in a pig's brain, it received 195 μW of power from the transmitter at 1.6 GHz, corresponding to an efficiency of 0.04%.

In [40] the authors propose a 46 mm^2 antenna for MF WPT to power endoscopic capsules. In a porcine model, an efficiency of 0.03% was achieved at 1.2 GHz when the receiving antenna was placed 58 mm away from the transmission one, with 50 mm corresponding to tissue and 8 mm to air gaps. Unlike previous works that are mentioned in this review, the authors have not attempted to focus the transmitted fields and doing so could result in an increased efficiency.

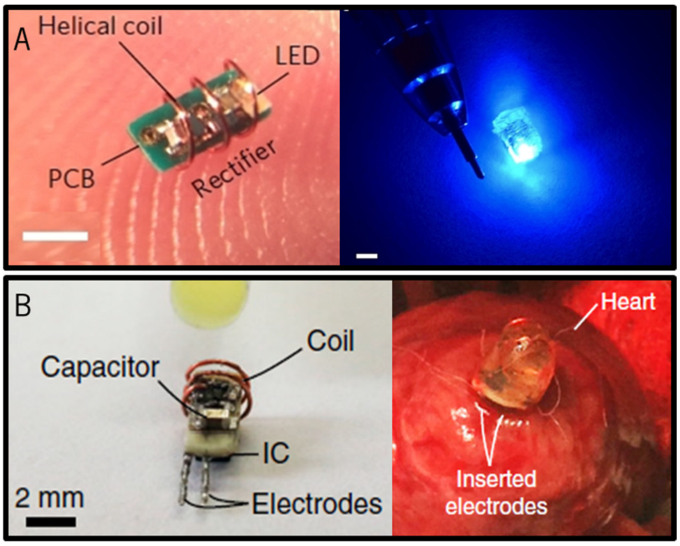

Figure 2.8 – Midfield-powered IMDs. A) Miniaturized MF WPT receiver (scale bar: 1 mm) [39]. B) MF-powered cardiac pacemaker with the detail of its implantation in a rabbit's heart (right) [38].

MF WPT has proven to be capable of powering small and deep-implanted IMDs. However, a drawback of this technique is that it requires an external component to be aligned with the implant for proper operation, like IC solutions.

2.3.4 Far field

Far field (FF) occurs when the receiving antenna is placed at a long-distance R from the receiver such that $R \geq 2D^2/\lambda$, where D is the largest dimension of the transmission antenna and λ the wavelength at the operating frequency. In the FF regime, the radiated fields propagate as a plane-wave, as illustrated in Figure 2.9.

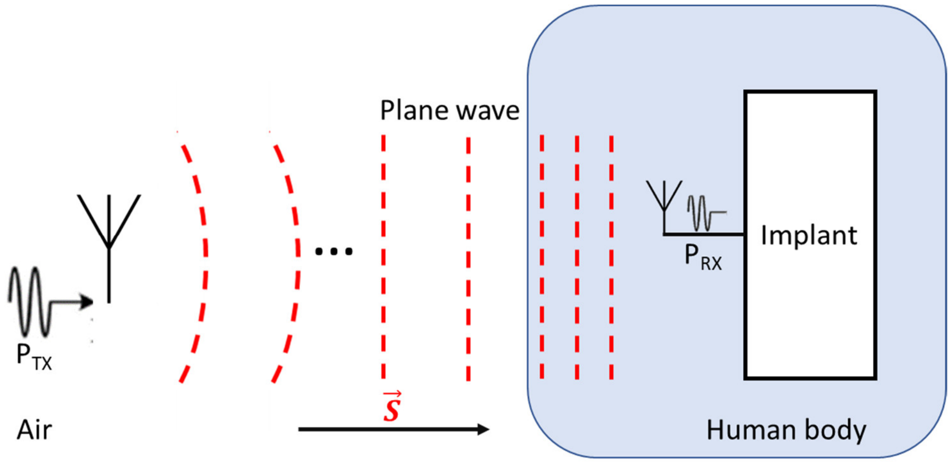

Figure 2.9 - Representation of far field WPT. A transmitter placed a long distance from the implant emits a RF wave that propagates through air and then through the human body, being received by the antenna of the implant.

The power received by the implant, P_R, can be calculated using Friis radio link formula, given by:

$$P_R = \frac{G_T G_R \lambda_0^2}{(4\pi d)^2}(1 - |S_{11}|^2)(1 - |S_{22}|^2)e_p \times P_T \tag{2.5}$$

where P_T is the power output of the TX antenna, G_T and G_R are the gains of the transmitter and receiver antennas, d is the distance between them and e_p is the polarization mismatch between the antennas. This equation gives the maximum achievable power at the receiver, as several other parameters such as the propagation medium's properties will factor into the received power [26].

In [41] the authors present a stretchable implant for neuromodulation applications. Figure 2.10 shows the implant and its target location in the rat. The device is powered in the far-field at 2.34 GHz and its reception antenna has an area of 9 mm^2. The design is relatively unaffected by physiological antenna strains, as an exaggerated experimental strain resulted in just a 12% efficiency decrease. The rat-implanted IMD's LED could produce 100 μW of optical power 20 cm away from a transmitter with a 2 W power output, resulting in an efficiency of 0.005%. Nevertheless, it is important to consider that the efficiency figure already includes the efficiencies from the RF-DC converter and the LED, thus the WPT link efficiency is higher than the value that was reported.

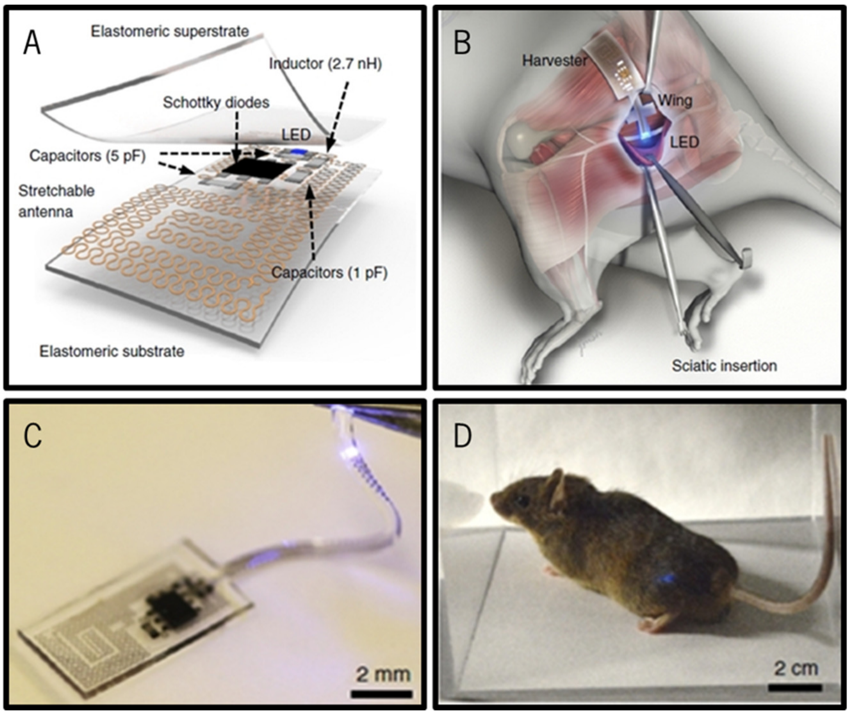

Figure 2.10 – A) Exploded view of the neuromodulator. B) Target implant location. C) Photograph of the device operating with FF WPT. D) Photograph of the IMD implanted in a rat [41].

FF WPT allows for truly untethered power link designs, with transmitters being placed at a considerable distance from the implant and the patient. This comes at the cost of link efficiency, which is lost due to, for example, free-space propagation losses.

2.3.5 Ultrasound

Low wave velocity and consequent improved efficiency, combined with low propagation loss and the ability to focus energy in specific spots [42], make ultrasounds (US) an appealing WPT approach. Furthermore, the FDA-defined maximum allowed power via US is around two orders of magnitude higher than that of RF waves [43].Here, a piezoelectric transducer (PZT) converts the source's AC signal into surface vibration which result in acoustic pressure that propagate in a medium. Conversely, at the IMD's side another PZT converts the acoustic waves into an electric signal that powers the device, as illustrated in Figure 2.11.

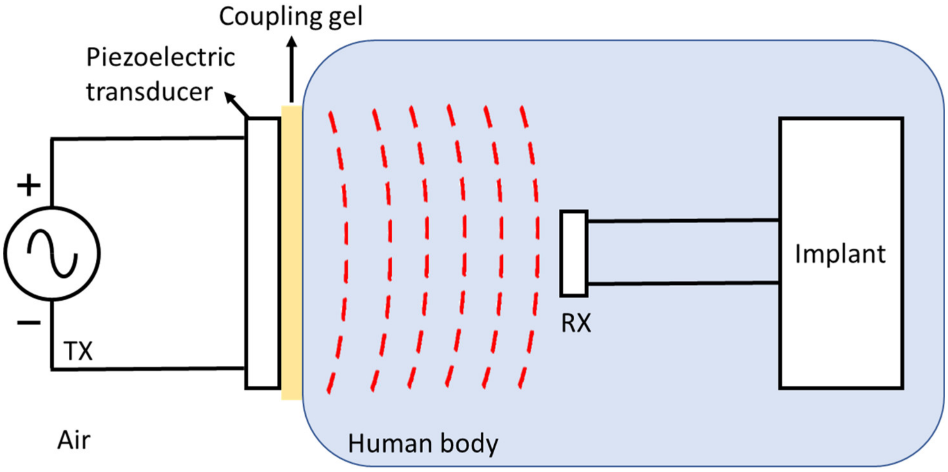

Figure 2.11 - Illustration of US WPT for IMDs. A transmitting piezoelectric transducer (PZT) is excited by an electrical AC signal. It produces a mechanical wave that couples with and propagates inside biological tissue until the implant's PZT converts the mechanical wave into useful electrical power.

The power transfer efficiency of a US WPT link depends on the transducer losses, the receiver's area, the link distance, and mechanical wave absorption in tissues and reflections in tissue interfaces [26].

In [42] a peripheral nervous system single-neuron recorder is presented (Figure 2.12 A). It consists of a piezoelectric crystal with an area of 0.56 mm^2 for powering and communication purposes, a transistor and two recording electrodes. The whole device measures around 0.8 x 3 x 1 mm^3. The device's operation is based on the signal reflected by its PZT, which varies with the electrical activity of the neuron. The IMD was validated with ENG and EMG signals from the peripheral nervous system of rats. Due to its operation method, no power and efficiency values were reported.

In [44] is presented an implantable microprobe for electrolytic ablation which has a volume of 54 mm^3 (Figure 2.12 B). The device is powered through an 8 mm^2 PZT at 650 kHz, achieving an efficiency of 0.02%. *In vitro* and *ex vivo* tests were performed to validate the operation of the IMD, and its ablation capabilities were verified.

In [45] a 0.8 mm^3 US-powered neural recorder was presented (Figure 2.12 C). Using a 1.78 MHz US link, a 0.56 mm^2 PZT receives at least 37.7 µW from the transmitter at a depth of 50 mm. No efficiency values are reported.

A micro-light source for photodynamic therapy powered by US WPT is reported in [46]. The IMD has a PZT transducer with an area of 4 mm^2 and, at a carrier frequency of 720 kHz, it can generate 48 µW of power with a link efficiency of 0.03% at a depth of 10 cm. The authors also designed a larger one and tested both of them *in vitro* and *in vivo* for cancer therapy with light stimulation, achieving results comparable to those reported using external light sources.

In [47] is presented a 39 mm^3 neural stimulator (Figure 2.12 D). This IMD has a PZT with an area of 2.72 mm^2 which, at 1.3 MHz, received 7.9 mW of power from an external transmitter through 10.5 cm of castor oil with a link efficiency of 0.04%.

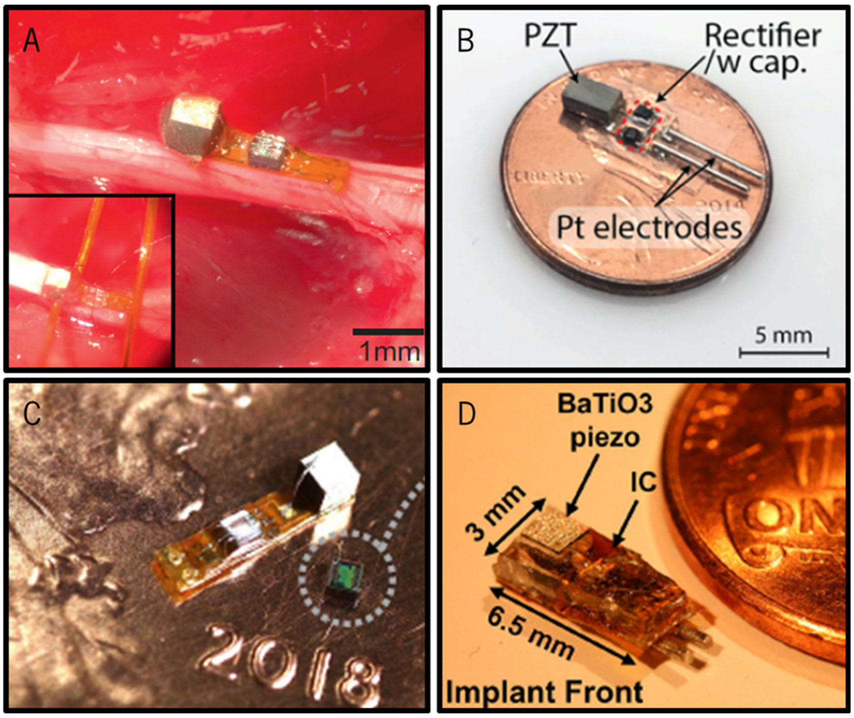

Figure 2.12 – State-of-the-art US-powered IMDs. A) Neural dust single-neuron recorder anchored to the sciatic nerve of a rat [42]. B) Microprobe for electrolytic ablation [44]. C) Sub-mm^3 free-floating neural recorder [45]. D) mm-sized peripheral nerve electrical stimulator [47].

US can also be used together with other technologies. In [48], the authors relied on US waves to induce micrometer-scale displacements of a triboelectric membrane under porcine tissue, which generated electrical energy that an implant could use. The reported device had dimensions in the centimeter range, but it is another promising potential future application of US WPT for IMDs.

US WPT has been proposed to overcome some limitations of RF-based power transmission. By having smaller wavelengths and slower propagation speeds in biological tissue, energy loss is reduced and better coupling with a small receiver is possible, which results in higher system efficiency. Nevertheless, US transmitters need to be placed in direct contact with skin to couple the waves with tissue, resulting in less freedom of movement for the patient or test subject. Furthermore, the high efficiency that was reported in the bibliography is boosted due to the US waves propagating through a single tissue type. In a real biomedical application, the waves' propagation path will include several tissue interfaces (e.g. skin-fat, fat-muscle) and possibly even bone or liquids, which cause severe attenuation, thus lowering the efficiency of the US link [49]. Finally, US WPT links are susceptible to efficiency drops due to misalignment between TX and RX PZTs.

2.3.6 Optical waves

Another method of wirelessly transmitting power is found in the bibliography, and it resorts to optical waves (OW). Optical charging integrates photovoltaic cells with the biomedical device, as represented in Figure 2.13 [50]. Furthermore, optical waves do not interfere with nearby communication systems, unlike RF waves. The link's power transfer efficiency depends on the implantation depth, *i.e.*, the distance that light must propagate through tissue, the type of tissue it must propagates through (since scattering and absorption are dependent on tissue type and wavelength of the light [51]), and the efficiency of the implant's photovoltaic cell.

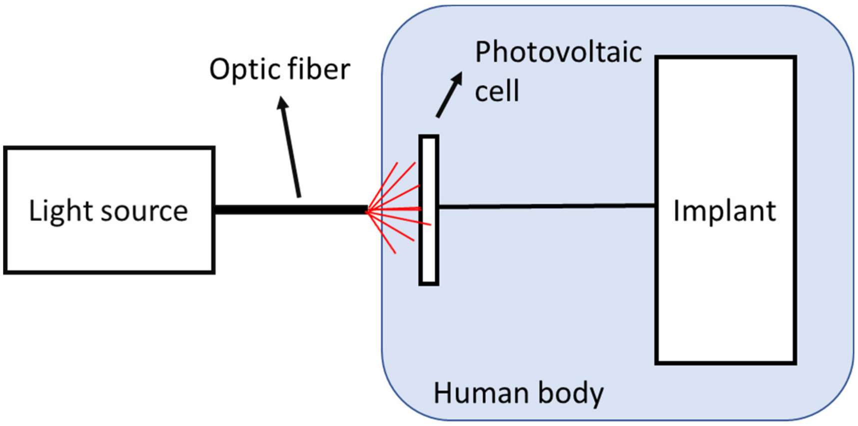

Figure 2.13 - Illustration of optical wave WPT mechanism, where an optic signal generated by a light source is guided to the skin's surface by an optic fibre. The light then propagates through the tissues, reaching a photovoltaic cell integrated in the implantable device and is converted into electrical power.

In [52], a bioresorbable PV device is presented. The WPT link is established with a wavelength of 780 nm, providing 64 µW to the device, but no overall link efficiency data is available. Each PV cell composing the PV device is 0.39 x 0.41 mm^2, while the whole implant is around 75 mm^2. The device's operation was validated in a rat, where it was implanted and used to power an LED.

In [53] a OW WPT system is employed to charge a pacemaker's battery. The reported results indicate that a pacemaker can be powered for 85 hours with 60 minutes of recharging time using this method. The implanted PV cell has an area of 90 mm^2 and produces 4.2 mW for the implant at a link efficiency of 16.3% with a 750 nm wavelength laser light source.

In [54] is presented a diamond encapsulated photovoltaic (PV) cell for transdermal power delivery. The PV cell has an area of 2.25 mm^2 and, when implanted under 2 mm of pig skin, can receive 117 μW for a potential IMD. Integration of this PV cell with an IMD was not presented, neither was the efficiency of the WPT link when implanted, but the device's small size and potential for use in subcutaneous IMDs is promising.

OW have proven capable of providing power to IMDs. Still, from the literature review, it is possible to conclude that this method, much like CC, is viable for low implantation depths. In the literature search, no small IMDs were found with a direct application of this WPT technique, as opposed to the remaining methods, hinting towards the embryonic stage of this technology.

2.3.7 Magnetoelectric

A magnetoelectric (ME) transducer converts energy from the magnetic domain to the electric domain and vice versa. Two different physical effects (piezoelectric and magnetostrictive) can be used to obtain an equivalent ME effect. A magnetostrictive material couples mechanical strain and magnetic field, while a piezoelectric material couples mechanical strain with the electric field. By linking both materials, a coupling between magnetic field and electric field can be achieved [55]. Figure 2.14 presents a schematic representation of the ME effect. As an incident magnetic field strains the magnetostrictive material, the piezoelectric material is also strained and generates an electric field used to power an IMD.

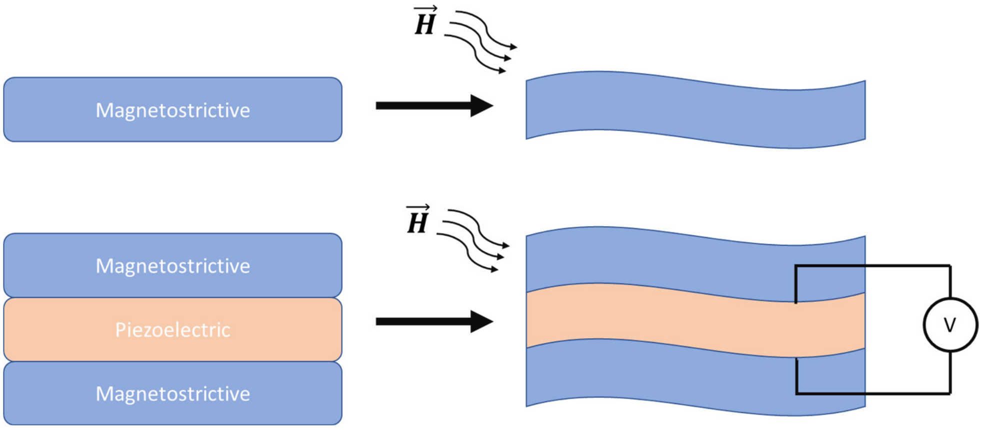

Figure 2.14 - Schematic representation of the ME effect produced by a sandwich-shaped transducer comprised of a piezoelectric material between two layers of a magnetostrictive material.

Despite being a relatively new technology that is in its early stages of development for IMD applications, publications where ME WPT is proposed for IMDs have been found in the literature [55], [56], and in [57] a neurostimulator powered by ME WPT is presented. The device has a total volume of

8.3 mm^3 and has a 8 mm^2 ME film consisting of two overlapping layers of lead zirconate titanate (PZT) and Metglas. To demonstrate the ME film's compatibility with implantation, it was packaged and tested in air and agar, a phantom that replicates the brain's mechanical properties. The film generated 160 µW at a 30 mm distance from the TX coil with a 0.008% efficiency. The IMD's operation capability was verified in a muscle tissue sample by activating ion channels.

2.3.8 Electrodynamic wireless power transfer

An additional WPT method is electrodynamic wireless power transfer (EWPT), where a low frequency (under 1 kHz) magnetic field is used to move a magnetic structure that, in turn, changes the magnetic flux of a coil in the implant, thus producing electrical power [58]. This is represented in Figure 2.15. Alternatively, an external rotating magnet can be used to generate the magnetic flux in the implanted coil, thus eliminating the need for the implanted permanent magnet [59].

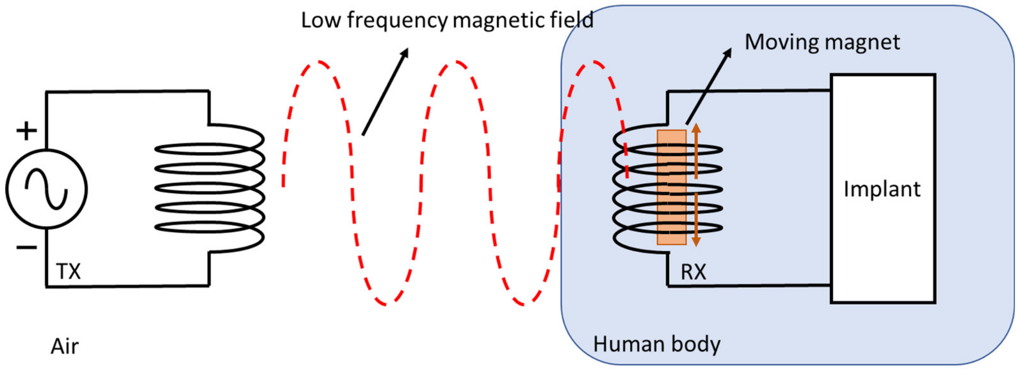

Figure 2.15 – Schematic representation of EWPT. A low-frequency magnetic field is generated by the external coil, and it causes a permanent magnet to move in the vicinity of an implant's coil. Consequently, the electric current generated in the coil is used to power the implant.

EWPT is a recent technology and as such, as far as we know, it has not yet been implemented in a miniaturized IMD for WPT purposes, unlike the previously cited works. At the time of writing this chapter, EWPT has been demonstrated to be a viable WPT solution [60]. Additionally, miniaturized [58] and bioresorbable [59] receivers have also been reported. Given its potential as a viable WPT technology for IMDs in the near future, since using a low-frequency magnetic field allows more efficient transmission of power through biological media [60], it was deemed important to approach EWPT in this review.

2.3.9 Choosing a suitable WPT technology

The previous sections presented state-of-the-art IMDs whose power demands are met with WPT mechanisms. These include ultrasounds, optical waves and RF, in which are included inductive and capacitive coupling, midfield and far-field transfer. The previously reported devices' characteristics are summarized in Table 2.1.

Inductive coupling can provide high power levels for coils with areas in the 100-mm^2 range, with reported efficiencies ranging from 0.3% to 0.002%. In [29] and [30], two coils with extremely small areas have been used to successfully power IMDs, albeit at small implantation depths. Despite its popularity and potential, this method has drawbacks that must be considered when developing a WPT solution. For example, to avoid coil decoupling due to misalignment, TX and RX coils' rigorous positioning is required. Moreover, the range of inductive coupling complies with exponential decay, meaning that the external coil must be close to the implant to maintain an acceptable power transfer efficiency [26], thus limiting the implantation depth of an IMD.

Capacitive coupling is, by far, the WPT technology that allows for the most power to be delivered to the implantable device and with one of the highest efficiencies. Still, these data alone are of little meaning. One must consider the overall size of the required RX pads, which are too large for miniaturized IMD applications. Furthermore, very shallow implantation depths have been reported. The power transfer capability of a CC system can be improved by increasing the electric field strength (by increasing the excitation voltage or reducing TX-RX separation), the rate of change of electric field (increasing the TX frequency), or the magnitude of the electric field (higher conductor area) [26]. All these requirements appear to be incompatible with deep-implanted miniaturized IMDs, as the TX-RX separation will be large, and an increased electric field strength or frequency will result in higher tissue losses and lower input power limit. As such, CC deems itself extremely valuable for subcutaneous implants, but not practical, at least in this stage of development, for deep-implanted IMDs.

Midfield regime power transfer devices boast larger link distances than IC ones in general, allowing greater implantation depths. Nevertheless, efficiency is lower than that of inductive coupling. Similarly to the latter, careful alignments between equipment are required, which must be accounted for in the design stages of such a WPT system. Additionally, this WPT technology requires an interference plate to be worn by the patient to concentrate power at the IMD, which can be cumbersome.

Far-field WPT provides, as expected, the largest link ranges at the expense of link efficiency, which allows for a completely untethered system to be developed. However, low power densities and link efficiencies are obtainable. In the literature there are multiple far-field powering methods for electronic devices. Still, very few of them applied for IMDs, most likely because IC has proven to be enough thus far, and the poor link efficiencies become a bottleneck in this technology. Nevertheless, as devices get smaller and more efficient, and increased implantation depth becomes necessary, FF WPT may receive increased attention in upcoming years.

Ultrasound links have proven to be a new and valuable WPT method for IMDs. Small RX dimensions allied with reasonable efficiencies at considerable implantation depths make it an appealing and promising approach for present and future IMDs. Nevertheless, it is essential to bear in mind that all the reported studies occurred in a homogenous propagation medium. US waves are not efficient when propagating through interfaces of tissues with different impedances, such as different organs and muscle, therefore a reduced efficiency is expected when these devices are tested in more realistic environments. Finally, the transmitting US transducer needs to be placed in direct contact with the skin of the subject due to the air-skin impedance mismatch, which can become a nuisance.

Optical links have been reported to achieve high efficiency and power delivery while operating through a thin section of skin, and proved capable of powering biomedical devices, thus making this a WPT method to be considered. A small OW WPT PV cell was presented in [54] which could generate enough power for a miniaturized IMD. However, no experimental validation of its use in an implant has been performed, which indicates that this technology is still in its early stages. Nevertheless, extremely shallow implantation depths have been reported, and only skin has been considered, which has little interaction with the wavelengths used in the selected papers. The inclusion of different tissues in the propagation path may lead decreased efficiency due to higher propagation distance and absorption in various tissues [61], rendering this technology more suitable for subdermal implants.

Magnetoelectric WPT is a relatively new technology that is in its early stages of development. The prospect of using a magnetic field to induce a mechanical acoustic wave that generates electrical power is appealing, as magnetic fields are not absorbed in the biological tissue and the wavelength of acoustic waves inside tissue is much smaller than that of EM waves, leading to smaller receivers [55]. Even so, the only application of this technology on a prototype IMD that was found when writing the present review reported results comparable to those of FF WPT, with slightly higher efficiency albeit for a much shorter distance. Nevertheless, the efficiency is likely to increase with improved transducers in the future. Hence, once the technology matures, ME WPT may become a prominent WPT technology.

Recently there have been efforts to integrate energy harvesting and wireless power transfer to power electronic devices [62]–[64]. With these works, it is possible to conceive wearable generators that can simultaneously scavenge ambient energy (e.g. body motions, body heat, and ambient solar radiation) and wirelessly transmit the energy to power implantable devices. Although the energy efficiency of the combination of EH and WPT is expected to be low, this symbiotic mechanism presents significant potential as the power requirement of IMDs also becomes lower.

The findings of the presented literature review and discussion are summarized in the following pages. Table 2.2 shows a list of pros and cons of the different WPT methods and Figure 2.16 proposes a graphical representation of the comparison between them as previously discussed.

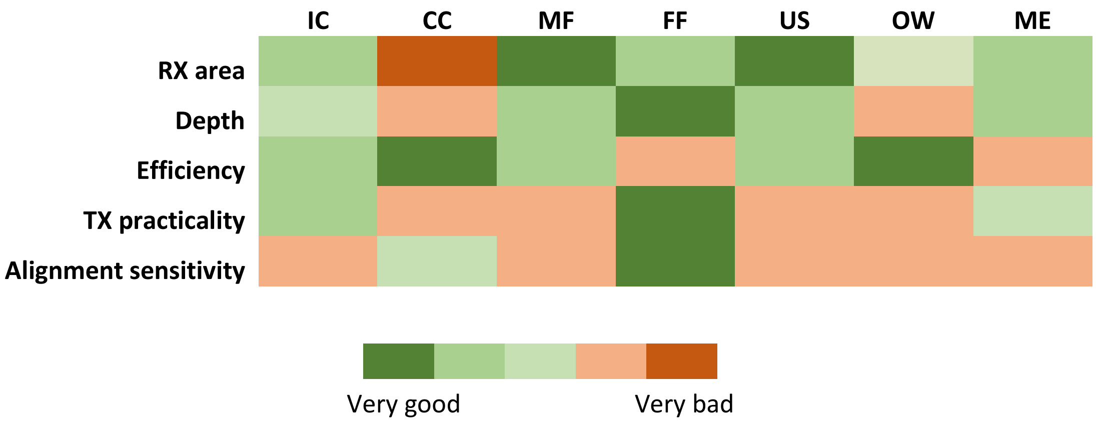

Figure 2.16 - Comparison of key parameters between WPT methods.

Table 2.1 – Summary of important data from state-of-the-art IMD WPT techniques.

Ref.	**Type**	**Distance (mm)**	**Frequency (MHz)**	**Antenna area (mm^2)**	**Power @ implant (μW)**	**Efficiency (%)**
[28]	IC	30.0	13.56	90.0	12000	0.300
[27]	IC	50.0	13.56	121.0	–	0.030
[30]	IC	4.6	1180.00	0.9	55.5	0.002
[29]	IC	1.5	900.00	1.8	5	0.100
[31]	IC	–	13.56	78.5	15000	–
[32]	IC	(a)	1500.00	2.0	10650	0.330
[35]	CC	2.0	130.00	400.0 (b)	90000	35.000
[37]	CC	2.0	0.12	800.0 (b)	75000	10.000
[36]	CC	15.0	260.00	83 mm, 2 mm radius (c)	1378	2.600
[39]	MF	42.0	1600.00	1.8	450	0.056
[38]	MF	50.0	1600.00	3.1	195	0.040
[40]	MF	58.0	1200.00	46.2	123	0.030
[41]	FF	200.0 (d)	2340.00	9.0	100	0.005 (e)
[42]	US	8.8	1.85	0.6	–	–
[47]	US	105.0	1.30	2.7	7900	0.040
[45]	US	50.0	1.78	0.6	37.7	–
[46]	US	100.0	0.72	4.0	108	0.030
[44]	US	–	0.65	8.0	450	0.020
[54]	OW	2.0	980 nm	2.3	117	–
[53]	OW	3.0	750 nm	90.0	4200	16.300
[52]	OW	4.0	780 nm	75.0	64	–
[57]	ME	30	–	8	160	0.008

(a) Energy is coupled through the whole mouse. Depends on its stance.

(b) Doesn't include the necessary area between electrodes.

(c) The electrodes are the stent itself.

(d) Air and mouse tissue.

(e) Efficiency calculated with optical power of the LED. Real value is higher.

Table 2.2 - Summary of pros and cons of each WPT method according to the literature review

	IC	**CC**	**MF**	**FF**	**US**	**OW**	**ME**
Pros	Efficiency Small RX Well established	Delivered power Efficiency	Efficiency Small RX	High depth TX practicality	High depth Small RX High efficiency	High efficiency	Low absorption Small RX
Cons	Low depth Misalignment	Low depth High RX area TX practicality	Misalignment TX practicality	Efficiency High absorption	Misalignment Losses in interfaces Losses in bone	Low depth Absorption in tissue TX practicality Misalignment	Misalignment Early development Efficiency

Figure 2.17 presents the link efficiency as a function of TX-RX distance and RX area, and Figure 2.18 is a plot of the power delivered to the reviewed IMDs (normalized and in a logarithmic scale) as a function of the same variables. The first shows that the link efficiency depends on the WPT technique, as MF and US WPT have similar efficiencies for the same RX areas but at very different distances. Meanwhile, Figure 2.18 conveys that higher power levels delivered to the IMD are achieved with bigger RX areas or at shorter distances between TX and RX.

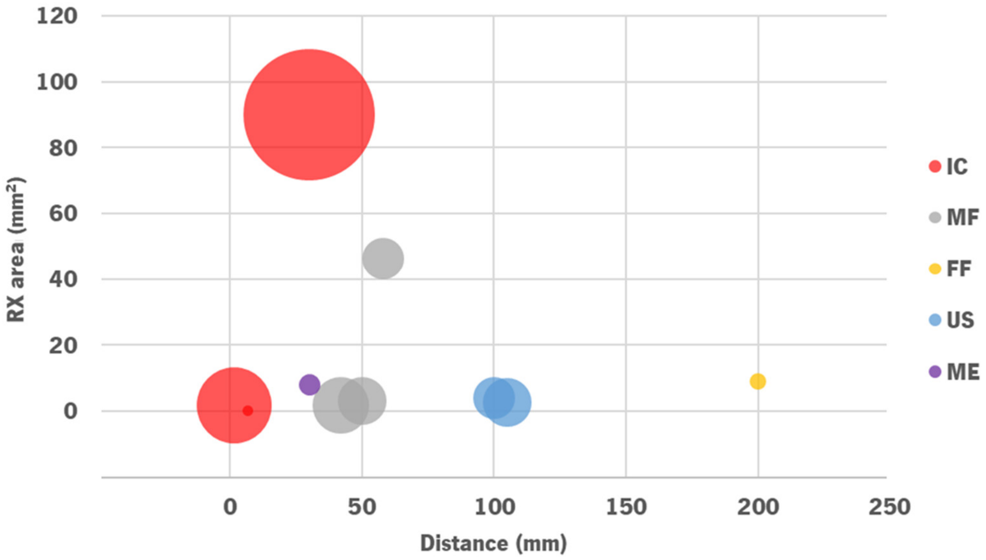

Figure 2.17 - Reviewed IMD's efficiency (represented by the area of the circles) as a function of distance and receiver area. Optical and Capacitive Coupling were excluded for clarity of presentation due to their high efficiencies.

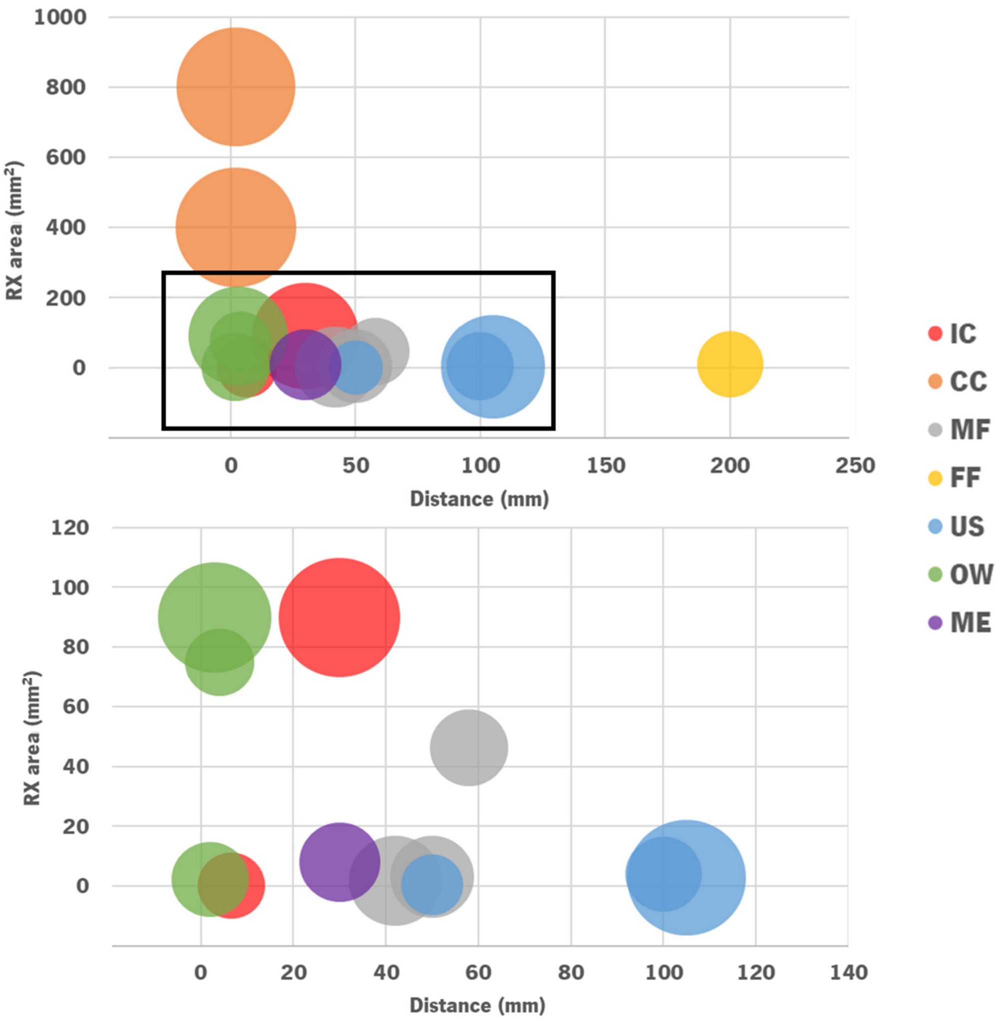

Figure 2.18 - Power delivered to the reviewed IMD (represented by the area of the circles) as a function of distance and receiver area. The power level is normalized and presented in a logarithmic scale. The graphic displayed in the bottom is a detailed view of the high-density area delimited by the rectangle in the full graphic.

Choosing the best WPT technique for a given application may become a complex task, given the large volume of information available. Naturally, the most suitable WPT technique for a given application is not the same as for a different one since each application's restrictions, goals and objectives may vary. This is easily visualised in Figure 2.17 and Figure 2.18, where different WPT techniques occupy distinct areas of the plots. Nevertheless, this chapter summarized the information of the best IMDs reported in the literature and analysed it to facilitate the aforementioned choice given the critical parameters of the desired outcome. Finally, the diagram presented in Figure 2.19 can be used as a guide or as an example of a WPT technique selection procedure.

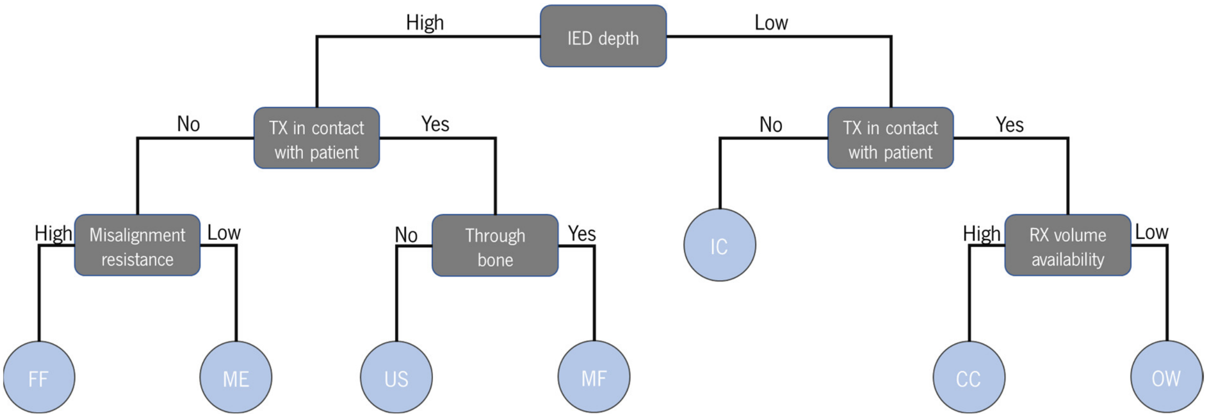

Figure 2.19 - Example of WPT technique selection according to design constraints.

2.4 Closing remarks

New applications in the human body for bioelectronics and biosensors are being enabled by the evolution of microfabrication techniques and microelectronics. These propelled the development of miniaturized IMDs which are more efficient and more capable than ever before. Powering these devices, however, is a technological hurdle that is yet to be surpassed. Batteries have not accompanied the downsizing of the IMDs and are not suitable for extremely small devices which are meant to be used in places of the human body without significant volume availability. Consequently, alternative powering methods such as EH and WPT become a necessity. The first, however, has also not matured enough to be useful in the described scenario. From the presented review, it was possible to conclude that WPT is currently the most promising powering method for IMDs, and several different WPT technologies are available. However, choosing one above all others is not possible, as the choice is heavily dependent on the design constraints that the IMD's application presents.

2.5 References

[1] R. Feynman, "There's Plenty of Room at the Bottom." 1959.

[2] M. Rasouli and L. Phee, "Energy sources and their development for application in medical devices," *Expert Rev. Med. Devices*, vol. 7, no. 5, pp. 693–709, 2010.

[3] N. S. Hudak and G. G. Amatucci, "Small-scale energy harvesting through thermoelectric, vibration, and radiofrequency power conversion," *J. Appl. Phys.*, vol. 103, no. 10, p. 101301, May 2008.

[4] D. Jiang *et al.*, "A 25-year bibliometric study of implantable energy harvesters and self-powered implantable

medical electronics researches," *Mater. Today Energy*, vol. 16, p. 100386, Jun. 2020.

[5] A. Nozariasbmarz *et al.*, "Review of wearable thermoelectric energy harvesting : From body temperature to electronic systems," *Appl. Energy*, vol. 258, no. October 2019, p. 114069, 2020.

[6] J. Al-Nabulsi, S. El-Sharo, N. Salawy, and H. Al-Doori, "Methods of energy generation from the human body: a literature review," *J. Med. Eng. Technol.*, vol. 43, no. 4, pp. 255–272, 2019.

[7] X. Huang *et al.*, "Materials Strategies and Device Architectures of Emerging Power Supply Devices for Implantable Bioelectronics," *Small*, vol. 16, no. 15, p. 1902827, Apr. 2020.

[8] J. Chen *et al.*, "Micro-cable structured textile for simultaneously harvesting solar and mechanical energy," *Nat. Energy*, vol. 1, no. 10, p. 16138, Oct. 2016.

[9] C. Dagdeviren *et al.*, "Conformal piezoelectric energy harvesting and storage from motions of the heart, lung, and diaphragm," *Proc. Natl. Acad. Sci.*, vol. 111, no. 5, pp. 1927–1932, Feb. 2014.

[10] M. Han *et al.*, "Three-dimensional piezoelectric polymer microsystems for vibrational energy harvesting, robotic interfaces and biomedical implants," *Nat. Electron.*, vol. 2, no. 1, pp. 26–35, 2019.

[11] G. Yao *et al.*, "Effective weight control via an implanted self-powered vagus nerve stimulation device," *Nat. Commun.*, vol. 9, no. 1, p. 5349, Dec. 2018.

[12] A. Zebda *et al.*, "Single Glucose Biofuel Cells Implanted in Rats Power Electronic Devices," *Sci. Rep.*, vol. 3, no. 1, p. 1516, 2013.

[13] E. Katz, "Implantable biofuel cells operating in vivo: Providing sustainable power for bioelectronic devices: From biofuel cells to cyborgs," in *2015 6th International Workshop on Advances in Sensors and Interfaces (IWASI)*, 2015, pp. 2–13.

[14] A. Haeberlin *et al.*, "Successful pacing using a batteryless sunlightpowered pacemaker," *Europace*, vol. 16, no. 10, pp. 1534–1539, 2014.

[15] K. Song, J. H. Han, H. C. Yang, K. Il Nam, and J. Lee, "Generation of electrical power under human skin by subdermal solar cell arrays for implantable bioelectronic devices," *Biosens. Bioelectron.*, vol. 92, no. November 2016, pp. 364–371, 2017.

[16] B. Shi, Z. Li, and Y. Fan, "Implantable Energy-Harvesting Devices," *Adv. Mater.*, vol. 30, no. 44, p. 1801511, Nov. 2018.

[17] S. H. Kim, C. H. Yu, and K. Ishiyama, "Rotary-Type Electromagnetic Power Generator Using a Cardiovascular System As a Power Source for Medical Implants," *IEEE/ASME Trans. Mechatronics*, vol. 21, no. 1, pp. 122–129, 2016.

[18] Q. Zheng *et al.*, "Biodegradable triboelectric nanogenerator as a life-time designed implantable power source," *Sci. Adv.*, vol. 2, no. 3, pp. 1–10, 2016.

[19] H. Ouyang *et al.*, "Symbiotic cardiac pacemaker," *Nat. Commun.*, vol. 10, no. 1, p. 1821, Dec. 2019.

[20] Q. Zheng *et al.*, "In vivo powering of pacemaker by breathing-driven implanted triboelectric nanogenerator,"

Adv. Mater., vol. 26, no. 33, pp. 5851–5856, 2014.

[21] M. Rasmussen, R. E. Ritzmann, I. Lee, A. J. Pollack, and D. Scherson, "An implantable biofuel cell for a live insect," *J. Am. Chem. Soc.*, vol. 134, no. 3, pp. 1458–1460, 2012.

[22] Q. Xu, F. Zhang, L. Xu, P. Leung, C. Yang, and H. Li, "The applications and prospect of fuel cells in medical field: A review," *Renew. Sustain. Energy Rev.*, vol. 67, no. 2017, pp. 574–580, 2017.

[23] L. M. Wangatia, S. Yang, F. Zabihi, M. Zhu, and S. Ramakrishna, "Biomedical electronics powered by solar cells," *Curr. Opin. Biomed. Eng.*, vol. 13, pp. 25–31, 2020.

[24] Y. Luo, L. Pu, G. Wang, and Y. Zhao, "RF Energy Harvesting Wireless Communications: RF Environment, Device Hardware and Practical Issues," *Sensors*, vol. 19, no. 13, p. 3010, Jul. 2019.

[25] H. Dinis, I. Colmiais, and P. M. Mendes, "Extending the limits of wireless power transfer to miniaturized implantable electronic devices," *Micromachines*, vol. 8, no. 12, 2017.

[26] K. Agarwal, R. Jegadeesan, Y. X. Guo, and N. V. Thakor, "Wireless Power Transfer Strategies for Implantable Bioelectronics," *IEEE Rev. Biomed. Eng.*, vol. 10, no. c, pp. 136–161, 2017.

[27] H. Lyu *et al.*, "Synchronized Biventricular Heart Pacing in a Closed-chest Porcine Model based on Wirelessly Powered Leadless Pacemakers," *Sci. Rep.*, vol. 10, no. 1, p. 2067, Dec. 2020.

[28] H. Zhang *et al.*, "Wireless, battery-free optoelectronic systems as subdermal implants for local tissue oximetry," *Sci. Adv.*, vol. 5, no. 3, p. eaaw0873, Mar. 2019.

[29] M. Mujeeb-U-Rahman, M. H. Nazari, M. Sencan, and W. Van Antwerp, "A Novel Needle-Injectable Millimeter scale Wireless Electrochemical Glucose Sensing Platform for Artificial Pancreas Applications," *Sci. Rep.*, vol. 9, no. 1, p. 17421, Dec. 2019.

[30] A. Khalifa *et al.*, "The Microbead: A 0.009 mm3 Implantable Wireless Neural Stimulator," *IEEE Trans. Biomed. Circuits Syst.*, vol. 13, no. 5, pp. 971–985, 2019.

[31] Y. Zhang *et al.*, "Battery-free, fully implantable optofluidic cuff system for wireless optogenetic and pharmacological neuromodulation of peripheral nerves," *Sci. Adv.*, vol. 5, no. 7, p. eaaw5296, Jul. 2019.

[32] K. L. Montgomery *et al.*, "Wirelessly powered, fully internal optogenetics for brain, spinal and peripheral circuits in mice," *Nat. Methods*, vol. 12, no. 10, pp. 969–974, 2015.

[33] W. Khan, Y. Jia, F. Madi, A. Weber, M. Ghovanloo, and W. Li, "Inductively coupled, mm-sized, single channel optical neuro-stimulator with intensity enhancer," *Microsystems Nanoeng.*, vol. 5, no. 1, p. 23, Dec. 2019.

[34] D. K. Freeman *et al.*, "A Sub-millimeter, Inductively Powered Neural Stimulator," *Front. Neurosci.*, vol. 11, no. NOV, p. 659, Nov. 2017.

[35] R. Jegadeesan, K. Agarwal, Y. X. Guo, S. C. Yen, and N. V. Thakor, "Wireless Power Delivery to Flexible Subcutaneous Implants Using Capacitive Coupling," *IEEE Trans. Microw. Theory Tech.*, vol. 65, no. 1, pp. 280–292, 2017.

[36] A. Aldaoud *et al.*, “Near-field wireless power transfer to stent-based biomedical implants,” *IEEE J. Electromagn. RF Microwaves Med. Biol.*, vol. 2, no. 3, pp. 193–200, 2018.

[37] R. Erfani, F. Marefat, A. M. Sodagar, and P. Mohseni, “Modeling and Experimental Validation of a Capacitive Link for Wireless Power Transfer to Biomedical Implants,” *IEEE Trans. Circuits Syst. II Express Briefs*, vol. 65, no. 7, pp. 923–927, 2018.

[38] J. S. Ho *et al.*, “Wireless power transfer to deep-tissue microimplants,” *Proc. Natl. Acad. Sci.*, vol. 111, no. 22, pp. 7974–7979, Jun. 2014.

[39] D. R. Agrawal *et al.*, “Conformal phased surfaces for wireless powering of bioelectronic microdevices,” *Nat. Biomed. Eng.*, vol. 1, no. 3, p. 0043, Mar. 2017.

[40] A. Abid *et al.*, “Wireless Power Transfer to Millimeter-Sized Gastrointestinal Electronics Validated in a Swine Model,” *Sci. Rep.*, vol. 7, no. 1, p. 46745, Sep. 2017.

[41] S. Il Park *et al.*, “Soft, stretchable, fully implantable miniaturized optoelectronic systems for wireless optogenetics,” *Nat. Biotechnol.*, vol. 33, no. 12, pp. 1280–1286, Nov. 2015.

[42] D. Seo *et al.*, “Wireless Recording in the Peripheral Nervous System with Ultrasonic Neural Dust,” *Neuron*, vol. 91, no. 3, pp. 529–539, 2016.

[43] J. Charthad, M. J. Weber, T. C. Chang, and A. Arbabian, “A mm-Sized Implantable Medical Device (IMD) With Ultrasonic Power Transfer and a Hybrid Bi-Directional Data Link,” *IEEE J. Solid-State Circuits*, vol. 50, no. 8, pp. 1741–1753, 2015.

[44] A. Kim *et al.*, “An Ultrasonically Powered Implantable Microprobe for Electrolytic Ablation,” *Sci. Rep.*, vol. 10, no. 1, p. 1510, Dec. 2020.

[45] M. M. Ghanbari *et al.*, “A Sub-mm3 Ultrasonic Free-Floating Implant for Multi-Mote Neural Recording,” *IEEE J. Solid-State Circuits*, vol. 54, no. 11, pp. 3017–3030, 2019.

[46] A. Kim *et al.*, “An Implantable Ultrasonically-Powered Micro-Light-Source (µLight) for Photodynamic Therapy,” *Sci. Rep.*, vol. 9, no. 1, p. 1395, Dec. 2019.

[47] J. Charthad *et al.*, “A mm-Sized wireless implantable device for electrical stimulation of peripheral nerves,” *IEEE Trans. Biomed. Circuits Syst.*, vol. 12, no. 2, pp. 257–270, 2018.

[48] R. Hinchet *et al.*, “Transcutaneous ultrasound energy harvesting using capacitive triboelectric technology,” *Science (80-.).*, vol. 365, no. 6452, pp. 491–494, Aug. 2019.

[49] G. Pinton, J.-F. Aubry, E. Bossy, M. Muller, M. Pernot, and M. Tanter, “Attenuation, scattering, and absorption of ultrasound in the skull bone,” *Med. Phys.*, vol. 39, no. 1, pp. 299–307, 2011.

[50] A. Ben Amar, A. B. Kouki, and H. Cao, “Power approaches for implantable medical devices,” *Sensors (Switzerland)*, vol. 15, no. 11, pp. 28889–28914, 2015.

[51] S. L. Jacques, “Optical properties of biological tissues: a review,” *Phys. Med. Biol.*, vol. 58, no. 11, pp. R37–R61, Jun. 2013.

[52] L. Lu *et al.*, “Biodegradable Monocrystalline Silicon Photovoltaic Microcells as Power Supplies for Transient Biomedical Implants,” *Adv. Energy Mater.*, vol. 8, no. 16, p. 1703035, Jun. 2018.

[53] A. Saha, S. Iqbal, M. Karmaker, S. F. Zinnat, and M. T. Ali, “A wireless optical power system for medical implants using low power near-IR laser,” *Proc. Annu. Int. Conf. IEEE Eng. Med. Biol. Soc. EMBS*, pp. 1978–1981, 2017.

[54] A. Ahnood *et al.*, “Diamond encapsulated photovoltaics for transdermal power delivery,” *Biosens. Bioelectron.*, vol. 77, pp. 589–597, 2016.

[55] T. Rupp, B. D. Truong, S. Williams, and S. Roundy, “Magnetoelectric Transducer Designs for Use as Wireless Power Receivers in Wearable and Implantable Applications,” *Materials (Basel).*, vol. 12, no. 3, p. 512, Feb. 2019.

[56] M. Zaeimbashi *et al.*, “NanoNeuroRFID: A Wireless Implantable Device Based on Magnetoelectric Antennas,” *IEEE J. Electromagn. RF Microwaves Med. Biol.*, vol. 3, no. 3, pp. 206–215, 2019.

[57] Z. Yu *et al.*, “An 8.2mm Implantable Neurostimulator with Magnetoelectric Power and Data Transfer,” in *2020 IEEE International Solid- State Circuits Conference - (ISSCC)*, 2020, pp. 510–512.

[58] N. Garraud, D. Alabi, J. D. Varela, D. P. Arnold, A. Garraud, and I. M. Group, “Microfabricated Electrodynamic Wireless Power Receiver for Bio-Implants and Wearables,” pp. 34–37, 2018.

[59] Q. Guo *et al.*, “A Bioresorbable Magnetically Coupled System for Low-Frequency Wireless Power Transfer,” *Adv. Funct. Mater.*, vol. 29, no. 46, p. 1905451, Nov. 2019.

[60] N. Garraud, A. Garraud, D. Munzer, M. Althar, and D. P. Arnold, “Modeling and experimental analysis of rotating magnet receivers for electrodynamic wireless power transmission,” *J. Phys. D. Appl. Phys.*, vol. 52, no. 18, p. 185501, May 2019.

[61] A. N. Bashkatov, E. A. Genina, and V. V. Tuchin, “Optical Properties of Skin, Subcutaneous, and Muscle Tissues: a Review,” *J. Innov. Opt. Health Sci.*, vol. 04, no. 01, pp. 9–38, Jan. 2011.

[62] Y. Chen, Y. Cheng, Y. Jie, X. Cao, N. Wang, and Z. L. Wang, “Energy harvesting and wireless power transmission by a hybridized electromagnetic-triboelectric nanogenerator,” *Energy Environ. Sci.*, vol. 12, no. 9, pp. 2678–2684, 2019.

[63] G. Chen, Y. Li, M. Bick, and J. Chen, “Smart Textiles for Electricity Generation,” *Chem. Rev.*, vol. 120, no. 8, pp. 3668–3720, 2020.

[64] N. Zhang *et al.*, “Photo-Rechargeable Fabrics as Sustainable and Robust Power Sources for Wearable Bioelectronics,” *Matter*, vol. 2, no. 5, pp. 1260–1269, 2020.

CHAPTER 3 ELECTROMAGNETIC FIELDS AND BIOLOGICAL TISSUE

Electromagnetic fields in the GHz range produce low-energy photons and, therefore, under ordinary conditions, their energy is too low to break chemical bonds, excite neutrons or ionize biological molecules. Consequently, they are often referred to as nonionizing radiation [1].

Although living organisms have thrived in natural EM environments, they are nowadays subjected to a plethora of human-made EM fields, which are used for communication, industry, and medical applications, among others. Besides their primary goals, these fields can also produce secondary effects that may influence the vital activities of an organism. These effects may or may not manifest themselves immediately after exposure and depend on many physical and biological factors [1].

The interaction of EM fields with biological tissues has long been a subject of scientific study, ever since their use in therapeutic applications. Since then, the knowledge on these interactions has increased massively, but this field is still far from being fully understood. The widespread use of EM sources in telecommunications (Wi-Fi, Bluetooth, 5G, WPT technologies, etc) has increased attention to the lack of understanding of the mechanism of interaction between EM waves and biological tissues [1].

3.1 Maxwell's equations

Maxwell's work was based on the vast knowledge developed by Gauss, Ampere, Faraday, and others. Maxwell's equations may describe the characteristics and behaviour of EM fields at the macroscopic levels. They provided a unification of the state of EM science at that time and hypothesized the existence of the electrical displacement current, which led Hertz to discover EM propagation [2].

EM waves propagate in biological tissues, and this interaction can be described by this set of four equations. Nevertheless, given the complexity and nonhomogeneous nature of biological tissues, it is not trivial to entirely characterize the propagation of EM waves in this medium. Fortunately, modern computation techniques allow for very accurate approximations to be made with complex simulation methods.

Maxwell's equations, in their differential form, are presented [2]:

$$\nabla \times \boldsymbol{H} = \boldsymbol{J} + \frac{\partial \boldsymbol{D}}{\partial t} \tag{3.1}$$

$$\nabla \times \boldsymbol{E} = -\frac{\partial \boldsymbol{B}}{\partial t} \tag{3.2}$$

$$\nabla \cdot \boldsymbol{B} = 0 \tag{3.3}$$

$$\nabla \cdot \boldsymbol{D} = \rho \tag{3.4}$$

The quantities in these equations are defined as follows:

- $\boldsymbol{H}$ is the magnetic field, in Ampere per meter (A/m);
- $\boldsymbol{J}$ is the electric current density, in Ampere per meter squared (A/m^2);
- $\boldsymbol{D}$ is the electric flux density, in Coulomb per meter squared (C/m^2);
- $\boldsymbol{E}$ is the electric field, in Volt per meter (V/m);
- $\boldsymbol{B}$ is the magnetic flux density, in Weber per meter squared (Wb/m^2); and
- ρ the electric charge density, in Coulomb per meter cubed (C/m^3).

Equation 3.1 describes that a circulating magnetic field is produced by an electric field that changes with time or by an electric current. Equation 3.2 states that variations of a magnetic field over time generate a circulating electric field. Equation 3.3 illustrates that there is no divergence of the magnetic field, as no magnetic monopoles (therefore sources or sinks) exist. Equation 3.4 defines that the divergence of the electric field is caused by the presence of charges (which act as sources or sinks) [3].

Maxwell's constitutive equations are defined as [2]:

$$\boldsymbol{B} = \mu \boldsymbol{H} \tag{3.5}$$

$$\boldsymbol{D} = \varepsilon \boldsymbol{E} \tag{3.6}$$

$$\boldsymbol{J} = \sigma \boldsymbol{E} \tag{3.7}$$

where μ is the permeability in Henry per meter (H/m), ε the permittivity in Farad per meter (F/m), and σ the conductivity (Ω^{-1}m^{-1}) of the propagation medium.

The conductivity of free space (vacuum) is 0 Ω^{-1}m^{-1}, and its permittivity and permeability are, respectively, given by [1]:

$$\varepsilon_0 = 8.854 \times 10^{-12} \text{ F/m} \tag{3.8}$$

$$\mu_0 = 4\pi \times 10^{7} \text{ H/m} \tag{3.9}$$

The relative permittivity and permeability of free space are both 1. Biological entities such as cells, tissues or organs have a relative permeability of 1, except for those containing ferromagnetic particles, such as red blood cells and the liver. However, the relative permittivity varies significantly between tissue types and with the temperature of the tissue and the frequency of the EM wave [1].

In a lossy material, such as biological tissue, the wave is attenuated as it propagates through the tissue. The magnitude of the propagating wave as a function of distance and time can be described as [4]:

$$E(z,t) = E_0 e^{-\alpha z} sin(\omega t - \beta z - \phi) \tag{3.10}$$

The attenuation constant α (Np/m) shows how quickly the wave is attenuated as it propagates through the medium. The electric field inside the medium can be expressed as a function of the propagation distance by $E_0 e^{-\alpha z}$, where E_0 is the magnitude of the incident field at the body surface, and z is the propagation distance, as exemplified in Figure 3.1.

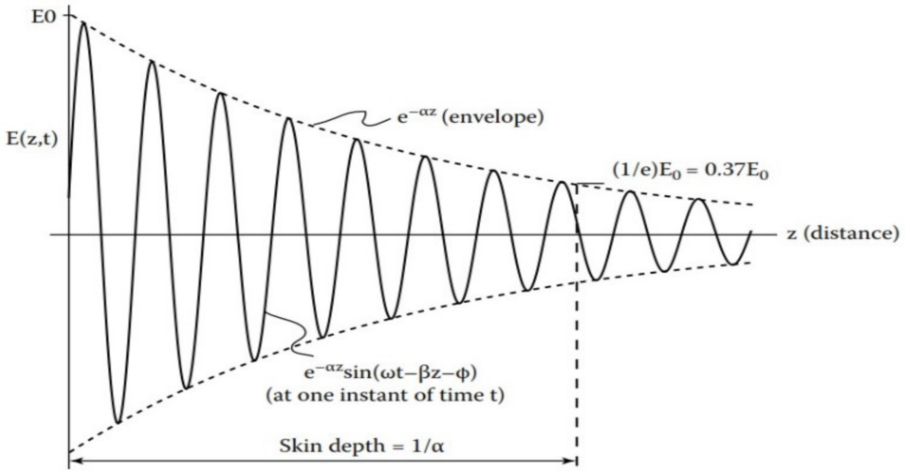

Figure 3.1 Magnitude of the wave $\boldsymbol{E}(z,t)$ travelling through a medium. The peak magnitude of this wave in a lossy material decreases exponentially as a function of distance travelled z. Its envelope is given by $e^{-\alpha z}$ [4].

The attenuation constant α is dependent on the field's frequency and the material's permittivity and conductivity, and can be calculated as [5]:

$$\alpha = \omega \left\{ \frac{\mu\varepsilon'}{2} \left[\sqrt{1 + \left(\frac{\varepsilon''}{\varepsilon'}\right)^2} - 1 \right] \right\}^{\frac{1}{2}} \text{ Np/m} \tag{3.11}$$

and the phase constant β is given by:

$$\beta = \omega \left\{ \frac{\mu\varepsilon'}{2} \left[\sqrt{1 + \left(\frac{\varepsilon''}{\varepsilon'}\right)^2} + 1 \right] \right\}^{\frac{1}{2}} \text{ rad/m} \tag{3.12}$$

From the attenuation constant, α, it is possible to determine the penetration depth, or skin depth, δ, which is the depth of tissue by which the electric field amplitude is reduced by e^{-1} (63%) [5]:

$$\delta = \frac{1}{\alpha} \tag{3.13}$$

For the propagation of a wave, it is also possible to define a phase velocity, which is the velocity at which a fixed phase point on the wave travels in a medium with relative permittivity ε_r and relative permeability μ_r, as:

$$v_p = \frac{1}{\sqrt{\mu\varepsilon}} = \frac{1}{\sqrt{\mu_r\mu_0\varepsilon_r\varepsilon_0}} = \frac{1}{\sqrt{\mu_r\varepsilon_r}\sqrt{\mu_0\varepsilon_0}} = \frac{c}{\sqrt{\mu_r\varepsilon_r}} \tag{3.14}$$

where $c = 2.998 \times 10^8$ m/s is the speed of light.

Finally, the wavelength of the wave is given by:

$$\lambda = \frac{c}{f\sqrt{\mu_r\varepsilon_r}} \tag{3.15}$$

3.2 Dielectric properties of biological tissues

The permeability of biological media is, for all practical purposes, equal to that of free space, as previously mentioned. Therefore, the interaction of microwaves with this media may be considered solely as the influence of electric fields. In that scenario, an energy exchange occurs between the microwave and the medium's free charges and structures with asymmetrical charge distributions (dipoles). The energy exchange can also induce dipoles.

The relative permittivity ε_r of a medium is a complex quantity [6]:

$$\varepsilon_r = {}^{\varepsilon}/_{\varepsilon_0} = \varepsilon_r' - j\varepsilon_r'' \tag{3.16}$$

As an electric field oscillates in the tissue, the dipoles rotate keep aligned with the field. The rotation of the dipoles is hindered by the frictional resistance of the viscous biological medium, and it relates to the imaginary part of the permittivity, ε_r''. The larger the imaginary part, the higher the losses in the medium, since more energy is being expended by the dipole through motions, resulting in a temperature increase of the medium and an greater attenuation of the electric field [6].

The conductivity σ of the medium can be related to ε_r'' [6]:

$$\varepsilon_r'' = \frac{\sigma}{\omega\varepsilon_0} \tag{3.17}$$

and the loss tangent is given by [6]:

$$\tan\delta = \frac{\varepsilon_r''}{\varepsilon_r'} = \frac{\sigma}{\omega\varepsilon_0\varepsilon_r'} \tag{3.18}$$

Databases of tissue electrical properties, such as IT'IS Foundation [7], usually provide the loss tangent $(tan\,\delta)$ and the real part of the relative permittivity ε_r'.

A biological tissue's permittivity and conductivity vary with frequency, and this variation is exemplified in Figure 3.2, where a muscle-like tissue's properties are presented.

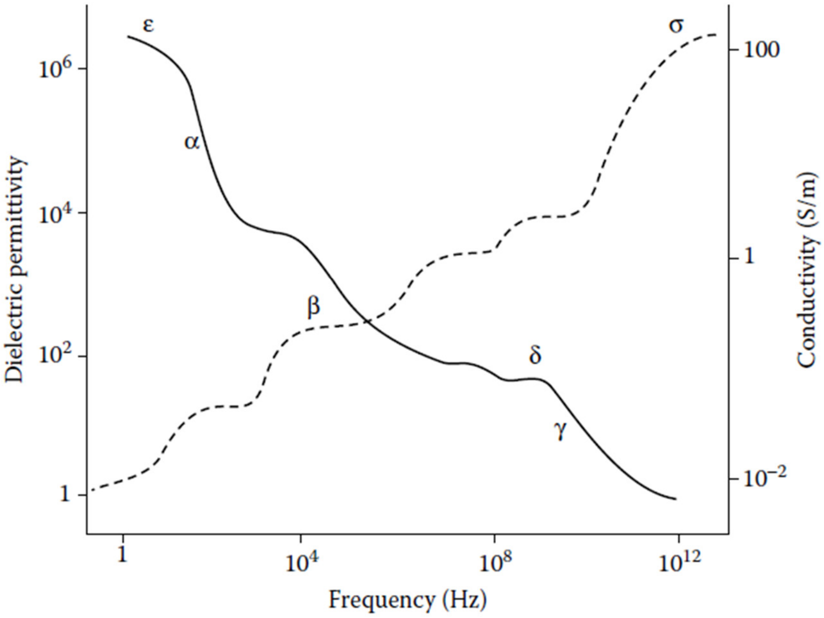

Figure 3.2 – Dielectric constant and conductivity over a wide frequency range of a tissue with muscle-like properties, where different dispersion regions can be identified [1].

At low frequencies, biological tissues exhibit very high dielectric constants due to the cell's membrane capacitance. An applied electric field at these frequencies causes charges to accumulate at the boundaries of the membranes. As frequency increases, the membrane becomes progressively more short-circuited, allowing for more current conduction. As such, the conductivity increases with frequency. For even higher frequencies, water molecules' rotational and vibrational properties become the most significant factor and viscous loss occurs, thus leading to higher conductivities [1]. It is, therefore, possible to distinguish three dispersion regions in the graphic:

- Alpha dispersion - variability of frequency of the cell membrane capacitance; very high dielectric constant and low conductivity;
- Beta dispersion - Relaxation due to the charging of cell membranes; and
- Gamma dispersion - dielectric relaxation of free water; high conductivity and lower dielectric constant [8].

3.3 Radiofrequency field coupling to biological systems

The interaction of time-varying EM fields with biological systems depends on the EM energy source's configuration and the field's frequency. These factors dictate the penetration and deposition of power, the induction of electric and magnetic fields, and the absorption of EM energy in biological tissue. The location of the radiation source relative to the biological medium is also important, as it dictates what kind of interaction the radiated waves have with the tissue [1].

3.3.1 Coupling in the near field

The use of RF radiation for wireless communication leads to frequent exposure of human bodies to RF waves in the near-field zone, especially with smartphones, as the reactive near-field distance is approximately 5 cm for a dipole antenna at 2400 MHz [1]. The fields in the near-field of an antenna are quasistatic [9], therefore they must be analysed as such.

A sphere of radius r, permittivity ε and conductivity σ is in the near field of a source that generates an external applied uniform electric field $\boldsymbol{E}$ polarized in the x direction. As such, a uniform induced electric field $\boldsymbol{E_E}$, also polarized in the x direction, appears inside the sphere due to the incident electric field $\boldsymbol{E_1}$ [1]:

$$\boldsymbol{E_E} = \left(\frac{\omega \varepsilon_0}{\sigma}\right) \boldsymbol{E_1} \tag{3.19}$$

The interaction of time-varying electric fields with biological tissues results in the flow of current in the tissue, the generation of electric dipoles, and the reorientation of the dipoles already present in the tissue [10]. As seen in the previous equation, the induced electric field inside the sphere is independent of its size r. On the other hand, the amplitude of the induced electric field relates to the amplitude of the incident field by a factor that depends on the conductivity of the tissue, σ.

The magnetic permeability of biological tissues is generally 1, as previously mentioned, and the magnetic field inside the body is equal to the one outside. As such, an incident magnetic field $\boldsymbol{H_1}$ generates an electric field $\boldsymbol{E_H}$ inside the body whose magnitude is given by [1]:

$$\boldsymbol{E_H} = \left(\frac{\omega r \mu}{2}\right) \boldsymbol{H_1} \tag{3.20}$$

The incident magnetic field induces an electric field that varies with the distance from the centre of the body, r, and results in circulating electric currents [10].

When both quasistatic electric and magnetic fields are present, the ratio between the electrically and the magnetically induced electric fields is a function of body size r and the incident field ratio ($\boldsymbol{E_1}/\boldsymbol{H_1}$) [1]:

$$\frac{\boldsymbol{E_E}}{\boldsymbol{E_H}} = \left(\frac{2\varepsilon_0}{\sigma \mu_0 r}\right) \cdot \left(\frac{\boldsymbol{E_1}}{\boldsymbol{H_1}}\right) \tag{3.21}$$

3.3.2 Coupling in the far field

In the far field, the propagating radiated RF energy has a planar wavefront and the electric and magnetic fields are related through a factor η, the intrinsic impedance of the medium [1].

At boundaries between different propagation mediums, RF energy is either reflected or transmitted. For a plane wave that is travelling in medium 1 with intrinsic impedance η_1 that impinges normally on medium 2 with intrinsic impedance η_2, thse reflection and transmission coefficients, R and T, are given by [1]:

$$R = \frac{\eta_2 - \eta_1}{\eta_2 + \eta_1} \tag{3.22}$$

$$T = \frac{2\eta_2}{\eta_2 + \eta_1} \tag{3.23}$$

$$T = 1 + R \tag{3.24}$$

In terms of power, the fraction of the incident power that is reflected is R^2, and the fraction of transmitted power is [1]:

$$T^2 = (1 - R^2) \tag{3.25}$$

For media with similar intrinsic impedances, most of the power is transmitted, while for media with very different intrinsic impedances, most of the power is reflected at the interface.

As the wave propagates through a tissue, RF energy is extracted from the wave and deposited in the tissue, resulting in a power density reduction as the field propagates. This reduction is quantified by the penetration depth which, in terms of power, is the depth at which the power has been reduced by a factor of e^{-2}. Penetration depth is dependent on the permittivity of the medium and the frequency of the RF wave, as seen in equations 3.11 and 3.13.

A propagation medium with a curved surface, e.g., the human head, can enhance coupling at great depths inside the body. Suppose the largest dimension of the medium is similar to the wavelength of the incident RF field. In that case, energy deposition and distribution will be influenced by the surface curvature of the body [1]. An example of this is provided in Figure 3.3, where an EM wave field impinges on a sphere and a cube of permittivity 9. As it can be seen, the electric field distribution inside the sphere generates hotspots inside the homogenous tissue which don't occur with planar surfaces.

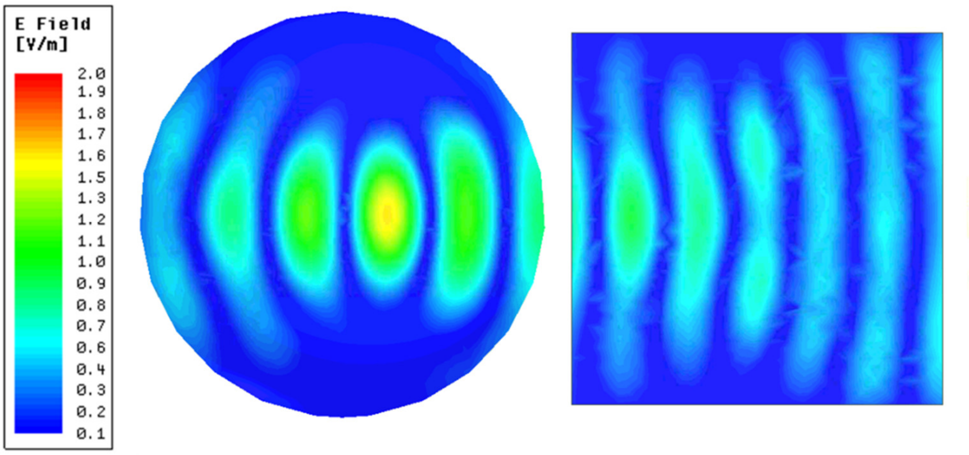

Figure 3.3 - Cross-section of the electric field distribution inside a sphere and a cube with permittivity 9. Both bodies are radiated by a 2 GHz plane wave. It is possible to distinguish a hotpot in the spherical volume due to its shape, which doesn't happen in the object with a planar surface.

3.4 Interference between co-polar coherent fields

Assuming two sources in free-space at distances r_1 and r_2 from a superposition point P, the electric field components of the two waves in P after traveling distances r_1 and r_2 are [11]:

$$E_1 = E_{01} \sin(k_w r_1 - \omega t) \tag{3.26}$$

$$E_2 = E_{02} \sin(k_w r_2 - \omega t) \tag{3.27}$$

where $k_w = {}^{2\pi}/_{\lambda}$.

The amplitude E_{0r} of the electric field component of the resultant wave in P is [11]:

$$E_{0r} = \sqrt{E_{01}^2 + E_{02}^2 + 2E_{01}E_{02}\cos\varphi} \tag{3.28}$$

where [11]:

$$\varphi = \frac{2\pi}{\lambda}(r_1 - r_2) \tag{3.29}$$

At locations P where $\varphi = 2\pi n$ (n = 0, 1, 2, 3, ...) [11]:

$$E_{0r} = |E_{01} + E_{02}| \tag{3.30}$$

Considering now N polarized coherent electromagnetic sources of the same polarization and frequency. At the location of constructive interference, the electric field amplitude of the waves emitted by these sources are E_{01}, E_{02}, ... E_{0N}. The resulting electric field becomes [11]:

$$E_{0r} = E_{01} + E_{02} + E_{03} + \cdots + E_{0N} \tag{3.31}$$

Consequently, for N identical sources [11]:

$$E_{0r} = NE_{0s} \tag{3.32}$$

The same conclusion can be drawn with magnetic field components [11]:

$$H_{0r} = NH_{0s} \tag{3.33}$$

Therefore, the average power of the EM wave from each of the identical sources is, at the point P of constructive interference:

$$S_{0s} = \frac{1}{2}(E_{0s} \times H_{0s}^*) \tag{3.34}$$

and the average power of the resulting wave is:

$$S_{0r} = \frac{1}{2}(E_{0r} \times H_{0r}^*) = \frac{1}{2}(NE_{0s} \times NH_{0s}^*) = \frac{N^2}{2}(E_{0s} \times H_{0s}^*) = N^2 S_{0s} \tag{3.35}$$

As such, when N identical sources are used, the average power at constructive interference locations increases by the N^{th} power.

3.5 Biological effects of EM exposure

It is important to distinguish between biological and health effects of EM exposure. A biological effect occurs when the external EM field causes a physiological change in a living system. Such a change may or may not lead to a health effect. This happens when physiological change is outside the normal range that the human body can compensate for and correct. Health effects are, usually, the result of accumulated biological effects over time [5].

The interaction of EM energy with biological systems can be studied at two levels: macroscopically (objects and whole body), and microscopically (cells, membranes and molecules). Nevertheless, interaction at the two levels cannot be considered independently. The effects of the interaction of EM energy with biological tissues is a result of three phenomena [5]:

- The penetration of EM waves into the biological medium and its propagation inside it;
- The interaction of the waves with the tissues (primary interaction); and
- The secondary effects due to the primary interaction.

Examples of the interaction of EM waves with biological tissue at the molecular and cellular level will be described here, along with the effect this interaction bears in tissues and living organisms.

Critical biomolecules for biological function are either electrically charged or polarized [11]. When exposed to an external polarized EM field, a coherent oscillation will be induced on each of these molecules. This oscillation is most noticeable on free ions, resulting in irregular gating of electrosensitive ion channels on the cell membranes [11]. Panagopoulos *et al* [11] theorised that the oscillation of free ions located in the vicinity of ion channels could exert enough force on said channels to disrupt normal functioning.

In the case of extremely low-frequency waves, such as power line signals (50 Hz), a field with $5\ \text{mV/m}$ can potentially disrupt normal cell function. For high-frequency signals, the scope of this thesis, extremely high field intensities would be required to produce the same effect (for a 1 GHz signal, $\boldsymbol{E_0}$ would have to be $100.000\ \text{V/m}$). Nevertheless, when high-frequency fields are pulsed in telecommunication applications, the $\boldsymbol{E_0}$ may also be very low. For example, for a pulse frequency of 217 Hz, used in GSM communication, $\boldsymbol{E_0}$ is around $20\ \text{mV/m}$ [11]. The result of the irregular gating of the ion channels is the disruption of the cell's electrochemical balance, which can potentially lead to a plethora of secondary effects [11].

The collision rates of molecules inside the biological medium can also be affected by a polarized electric field. Considering a chemical reaction that occurs, for example, in the cell membrane between a protein and an ion, the rate at which this reaction occurs is proportional to the flow of ions that collide with the protein and carry enough energy to start the reaction. By introducing an external influence on the flow of the ions, the reaction rate is tampered with, which influences the normal behaviour of the cell [12]. Additionally, the collision angle between two molecules often dictates if a reaction does or does not happen. In the case of proteins, this angle can be minimal. By orienting all molecules according to an external polarized field, this mechanism is influenced [12].

Modified biological activity does not necessarily translate into observable biological or health effects, as cells/tissues/organisms are gifted with adaptive mechanisms that can handle disruptions. Nevertheless, these may not be completely effective, as the organism could be under additional stress [11].

The previous findings were considered with extremely-low-frequency fields, which occur with telecommunication applications, for example, both due to the pulsing of the high-frequency carrier waves, and the fact that biological tissues are placed in the near field of mobile phone antennas.

An example of a macroscopic effect of RF exposure is the microwave-induced auditory effect, where humans perceive pulse-modulated fields with frequencies between 200 MHz and 6.5 GHz. The pulsed signals have been described as clicks, pops or buzzes, depending on the modulation characteristics [10].

In [13], microwave-hearing is attributed to the rapid expansion of water present in the tissue, and consequent acoustic wave generation, due to the local heating of the tissue, which even though it is very little (in the order of the microdegrees), the rate of heating is high (in the order of the 1 $^{\circ}C\ s^{-1}$). Behaviour changes have also been extensively reported, but these were attributed to thermal effects [14].

When one reviews the literature regarding the biological and health effects of EM exposure, it is expected that by the end of the process, a conclusion can be made regarding the topic. However, such is not the case here. Different studies produced disparate results. While some authors argue that EM exposure is responsible for several ailments and biological alterations, other authors claim that no convincing and accurate data exists to lead to such conclusions and that the observed effects are mainly due to thermal mechanisms.

In her extensive literature review, Sage [15] summarizes a series of scientific articles in which several biological effects occurs under continuous and pulsed RF radiation, such as damage to DNA, chromosome aberrations, the expression of specific genes, induced responses in nervous tissue cells, reduced immune function, changes in the integrity of the blood-brain barrier, reduced fertility, higher cancer incidence, learning deficit, and sleep disruption.

Others question such results, especially when considering the low intensity of the fields. Chou [16] collected a series of papers where reported non-thermal effects were related to temperature increase due to artifacts in the experiments. For example, behaviour studies in rats concluded that RF exposure at low level induced behaviour changes due to non-thermal effects. It has been later shown that the local heating in the rats' legs was very high when they were drinking from a metallic nozzle, thus provoking the behaviour changes. Adair *et al* [14] state that tissue heating is an important effect of RF exposure of biological organisms and that it has been unequivocally demonstrated. They then also agree with the previous author, in the regards that most papers claiming non-thermal effects are reporting on artifacts and not accurate data, further adding that, at the time of writing of the paper, controversial claims of non-thermal effects of modulated RF signals are not substantiated experimentally nor have they been independently replicated.

The best example of the duality of available results was found in Kato's book [17], where the author reviewed the literature to find that, for example: carcinogenesis does not seem to be affected by mobile phone signals; no concrete evidence shows that microwave exposure changes the microscopic anatomy of regions of the brain; contradicting results have been obtained regarding non-thermal effects on the blood-brain barrier, even though studies reporting an effect were later reproduced and did not observe that same effect; neurotransmitter function in the CNS is only altered under high exposure levels, i.e. due to the thermal impact; the effects on nerves are caused primarily by heating, similarly to hormones.

The International Committee on Electromagnetic Safety (ICES) Technical Committee TC95, which was responsible for the IEEE C95.1 EM exposure guidelines [18], reports that they have considered studies that link EM waves with adverse health effects when developing the safety guidelines. Some of their conclusions can be highlighted:

- The World Health Organization (WHO) analysed the 2002 International Agency for Research on Cancer report that linked exposure to ELF magnetic fields to childhood leukaemia, and concluded that the evidence is not strong enough to be considered causal;
- At higher frequencies, brain cancer has been associated with the use of mobile phones, but the epidemiologic evidence did not provide sufficient basis for concluding that brain cancer in adults is positively associated with mobile phone use and, consequently, RF exposure;
- The WHO indicated that no adverse health effects have been linked to mobile phone use;
- The International Agency for Research on Cancer (IARC) classified RF EM fields as possibly carcinogenic to humans, under Group 2B, which is used when causal association is considered credible, but when chance, bias or inaccuracies cannot be ruled out with confidence; and
- The International Commission on Non-Ionizing Radiation Protection (ICNIRP) Standing Committee on Epidemiology concluded that evidence accumulates against the hypothesis that mobile phone use causes brain tumours in adults, and that no plausible biophysical mechanisms have explained the hypothesized effects at low-level exposure.

Consequently, ICES concluded that only the established mechanisms of electrostimulation for signals of frequencies between 0 Hz and 100 kHz and tissue heating between 100 kHz to 300 GHz needed to be considered to provide a valid basis for the exposure safety guideline they developed [18], which will be further explained in a following section of this chapter.

As a closing remark for this section, to the best of our knowledge it is impossible to present a clear and scientifically bulletproof conclusion to this topic. The mechanisms that can possibly yield non-thermal effects were presented, and examples of such effects were provided. On the other hand, claims that such effects are not proven at low exposure levels have also been reported. The only topic in which there is a consensus is the occurrence of thermal effects in biological tissue due to high-frequency exposure, and electrostimulation in low-frequency exposure, which are the parameters by which safety exposure limits and guidelines base themselves. Thus, following these safety guidelines is the best one can do when designing a system that exposes biological tissue to EM radiation.

3.6 Safety electromagnetic exposure standards

Exposure standards are adopted standards of personal protection that refer to maximum levels to which whole or partial body exposure is permitted from EM field sources. Examples of such standards are given by the Institute of Electrical and Electronics Engineers (IEEE) (Standard C95.1-2005) [19], International Commission on Non-Ionizing Radiation Protection (ICNIRP) [10], and U. S. Federal Communications Commission (FCC) [20]. These standards were developed independently and constitute the foundations to most national exposure limits, except for China, Russia and some Easter European countries [12].

As stated in the IEEE C95.1-2005 documentation [19]: “The purpose of this standard is to provide exposure limits to protect against established adverse effects to human health induced by exposure to RF electric, magnetic and electromagnetic fields over the frequency range of 3 kHz to 300 GHz”, while ICNIRP (1998) states that it aims to “establish guidelines for limiting EMF exposure that will provide protection against known adverse health effects” [10].

The exposure standards began with a comprehensive and critical scientific review of available literature by a panel of experts who evaluated the literature, determined threshold levels, identified safety factors and derived the exposure limits. For example, IEEE C95.1-2005 was developed according to a literature database of 3676 papers, which were summarized in a collection of 12 reviews. The standard itself is a 250-page document with 1143 references. ICNIRP was developed with a similar extensive review [12].

IEEE C95.1-2019 [18] and ICNIRP (1998) cover the frequency range up to 300 GHz. Updates have been issued to both standards as time went by. For example, in 2010 ICNIRP applied a new set of guidelines to electric and magnetic fields from 1 Hz to 100 kHz and revised the existing guidelines up to 10 MHz [21].

The institutions that create the guidelines keep a close watch on studies regarding the safety of EM exposure, to keep the standards up to date. For example, the ICNIRP recently reviewed two major studies regarding the carcinogenicity of mobile phones and base stations in rats [22]. Both studies concluded that male rats had increased cancer rates under exposure, and one of them also concluded that the effect was not registered in female rats or mice. In both cases, the ICNIRP found significant weaknesses such as "lack of blinding, difficulty interpreting statistical data and a failure to account for chance", thus ruling out the results as meaningful for concluding on RF fields and carcinogenesis.

3.6.1 Dosimetry

It is essential to distinguish between exposure (fields measured outside the body) and dose (induced fields within the body) when assessing exposure to RF fields.

Exposure measurements are [12]:

- External field strength – electric field (V/m), magnetic field (A/m), or magnetic flux density $\boldsymbol{B}$ (T). External field strength is usually more useful in the lower end of the frequency range, where exposures occur in the near field of the sources and the electric and magnetic fields are essentially independent; and
- Incident power density, $\boldsymbol{S}$ (W/m^2) – useful in the far-field of radiators, where exposure consists of EM fields propagating through space.

Dose measurements are [12]:

- Current density within the body $\boldsymbol{J_i}$ (A/m^2) – mainly useful at low frequencies. It is related to the *in situ* internal electric field strength $\boldsymbol{E_i}$ (V/m) by Ohm's law (equation 3.7);
- Contact current $\boldsymbol{J}$ (A) – current passed into the body through contact with an external charged objected; and

- Specific absorption rate (SAR) (W/kg) – SAR is a measure of the energy deposition rate in the body. Given its importance in the scope of this thesis, it will be detailed in a separate section, which follows.

3.7 Specific absorption rate

SAR is a measurement of how much energy from the RF wave is absorbed by the tissue, therefore it is a great way to assess thermal effects. SAR cannot be measured directly, but it is related to the RMS of the local electric field strength E [12]:

$$SAR = \frac{\sigma E^2}{\rho} \tag{3.36}$$

where σ (S/m) is the conductisvity and ρ is the mass density of the tissue.

SAR can be defined at single points in space, and it is averaged over a defined mass (for example, a cube of 1 gram of tissue), or over the whole body. Whole-body SAR is significant at estimating elevations of the core body temperature. The whole-body SAR of an organism will be highest at a particular resonant frequency range, which is a function of the body size and its orientation relative to the incident fields. For an average human, peak whole-body SAR occurs at 60-80 MHz. Local (or spatial) peak SAR is used when absorption takes place in a confined body region (e.g. when estimating head exposure to a mobile phone's radiation) [5].

The biological effects of RF exposure are typically correlated to induced increases in tissue temperature, and SAR allows evaluating that parameter. Considering that SAR is a measurement of the power absorbed by a given mass of tissue [23]:

$$SAR = \frac{dP}{dm} \tag{3.37}$$

and, considering and homogenous medium with specific heat c (J/kg K), a form of the calometry law comes as [23]:

$$\frac{\mathrm{d}Q}{\mathrm{d}t} = mc\frac{\mathrm{d}T}{\mathrm{d}t} \tag{3.38}$$

The term dQ/dt is the wave power transformed into an incremental amount of heat dQ within the tissue of mass m that produces a temperature increase dT during the time dt. Combining the two previous equations [23]:

$$SAR = c\frac{\mathrm{d}T}{\mathrm{d}t} \tag{3.39}$$

However, the use of SAR for the evaluation of the effects of human exposure to EM fields is not free of criticism, and some authors point to issues and considerations they believe should be addressed that are not covered by this parameter. For example, Panagopoulos et al [23] raise some concerns about the sole use of SAR as a criterion to decide whether or not an RF signal will cause harm, as the authors base themselves on the studies indicating that the interaction of specific biomolecules and EM waves is what dictates the biological effect of the exposure. Nevertheless, this discussion dwells on the subject previously discussed about the uncertainty in this matter. In their excellent bibliographical reviews, independent organizations (IEEE and ICNIRP) came up with very similar exposure safety guidelines, and until solid evidence is provided against them, such guidelines should be followed.

3.8 Guidelines

The exposure limits are defined differently according to the frequency of the applied EM field. For the most recent IEEE standard at the time of writing of this thesis, IEEE C95.1-2019 [18]:

- 0 Hz to 5 MHz: electrostimulation is the primary concern, therefore the maximum *in situ* electric field or magnetic field are the controlling criteria, which vary with body region.
- 5 MHz to 300 GHz: only thermal effects apply, and SAR and power density incident on the body are the controlling parameters; and
- 100 kHz to 5 MHz: both electrostimulation and thermal effects can occur, therefore protection against both is provided by two separate sets of limits.

The tables that follow were adapted from IEEE C.95.1-2019 [18], and they provide the Dosimetric Reference Limits (DRLs) and Exposure Reference Levels (ERLs) for whole-body and local exposures in restricted and unrestricted environments for the frequency range of 100 kHz to 6 GHz.

Table 3.1 - DRLs (100 kHz to 6 GHz) [18].

Conditions	**Unrestricted environment SAR (W/kg)** ^{a}	**Restricted environment SAR (W/kg)** ^{a}
Whole-body exposure	0.08	0.4
Local exposure (head and torso) ^{b}	2	10
Local exposure (limbs and pinnae) ^{b}	4	20

^{a} SAR is averaged over 30 min for whole-body exposure and 6 min for local exposure.

^{b} Averaged over a 10 g mass of tissue in the shape of a cube.

Table 3.2 - Local exposure ERLs (100 kHz to 6 GHz) in unrestricted environments [18].

Frequency range (MHz)	**Electric field strength (V/m)** ^{a,b,c}	**Magnetic field strength (A/m)** ^{a,b,c}	**Power density S (W/m2)** ^{a,b,c}	
			S_E	S_H
0.1 – 1.34	1373	$36.4/f_M$	5000	$500000/\ f_M{}^{2}$
1.34 – 30	$1842/f_M$	$36.4/f_M$	$9000\ f_M{}^{2}$	$500000/\ f_M{}^{2}$
30 – 100	61.4	$353/f_M{}^{1.668}$	10	$47000000\ f_M{}^{3.336}$
100 – 400	$21.2\ f_M{}^{0.232}$	$0.056 f_M{}^{0.232}2$	$1.19\ f_M{}^{0.463}$	
400 - 2000	-	-	$1.19\ \ f_M{}^{0.463}$	
2000 - 6000	-	-	40	

Note 1 – Below 6 GHz, portable devices are typically tested for DRL compliance (SAR).

Note 2 – S_E and S_H are plane-wave-equivalent power density values based on electric or magnetic field strength, respectively.

^{a} Determined in air at the location of the body surface.

^{b} Spatial and temporal peaks averaged over 6 min.

^{c} f_M is the frequency in MHz.

In scenarios where medical implants are present in the body, extra caution is advised, as extremely high local fields can occur, which may not be detectable in a 10-g averaged SAR [18]. ICNIRP even suggest that, in such cases, the time average of the SAR should be under 1 minute, and with a smaller averaging mass to try to detect the localized exposure [24].

When the exposure happens in the near field of the EM radiation source, SAR is also well correlated with temperature increase, as stated in [12].

In the presence of different fields at several frequencies for which there are different values of the ERL, the percentage of the ERL incurred within each frequency interval must be determined, and the sum of all percentages must not exceed 100 %.

Table 3.3 - Local exposure ERLs (100 kHz to 6 GHz) in restricted environments [18].

Frequency range (MHz)	**Electric field strength (V/m)** ^{a,b,c}	**Magnetic field strength (A/m)** ^{a,b,c}	**Power density S (W/m2)** ^{a,b,c}	
			S_E	S_H
0.1 – 1	4119	$36.4/f_M$	45 000	$500\,000/{f_M}^2$
1 – 30	$4119/f_M$	$36.4/f_M$	$9\,000\,{f_M}^2$	$500\,000/{f_M}^2$
30 – 100	137.3	$36.4/f_M$	10	$500\,000/{f_M}^2$
100 – 400	$47.3{f_M}^{0.232}$	$0.125{f_M}^{0.232}$	$5.93\ {f_M}^{0.463}$	
400 - 2000	-	-	$5.93\ {f_M}^{0.463}$	
2000 - 6000	-	-	200	

Note 1 – Below 6 GHz, portable devices are typically tested for DRL compliance (SAR).

Note 2 – S_E and S_H are plane-wave-equivalent power density values based on electric or magnetic field strength, respectively.

^{a} Determined in air at the location of the body surface.

^{b} Spatial and temporal peaks averaged over 6 min.

^{c} f_M is the frequency in MHz.

Local exposures to pulsed RF fields of frequencies from 100 kHz to 300 GHz have a specific set of limits in both restricted and unrestricted environments. Peak power density limits are provided as follows to prevent high local exposure [18].

The total incident energy density of a pulse train in any period of 100 ms is [18]:

$$\sum_{i=1}^{n}\left(S_{ipeak} \times \tau_i\right) \text{ (J/m}^2\text{)} \tag{3.40}$$

where:

- n is the number of pulses in the 100 ms period;
- S_{ipeak} is the average (temporal) power density, averaged over τ_i, of the ith pulse (W/m^2); and
- τ_i is the width (s) of the ith pulse (or a partial pulse width if any 100 ms period captures only a portion of a pulse).

Compliance is established with [18]:

$$\sum_{i=1}^{n}\left(S_{ipeak} \times \tau_i\right) \leq \frac{ERL_{local} \times t_{avg}}{5} \text{ (J/m}^2\text{)} \tag{3.41}$$

where:

- t_{avg} is 6 min; and
- ERL_{local} is the ERL for a local exposure at a given frequency shown in Table 3.2 and Table 3.3.

The summation on the left side of (3.41) applies to any 100 ms of exposure.

This guideline is also equivalent to limiting the specific absorption (SA) (J/kg) below 6 GHz to one-fifth of what is allowed for a continuous field [18]:

$$\sum_{i=1}^{n}\left(SAR_{ipeak} \times \tau_i\right) \leq \frac{DRL_{local} \times t_{avg}}{5} \text{ J/kg} \tag{3.42}$$

where:

- SAR_{ipeak} is the temporal peak SAR (W/kg) of the ith pulse;
- t_{avg} is 6 min; and
- DRL_{local} is the SAR limit shown in Table 3.1.

With the previous equations, it is possible to conclude that using pulsed signals with the intent of powering an implantable device would result in a smaller amount of energy being delivered to the device throughout the exposure rather than when a continuous wave is used. However, since the instantaneous power of a pulsed wave can be higher than that of a continuous one, a pulsed WPT can be used when the power delivered by the continuous wave is insufficient to, for example, polarize the diodes of the implant's RF-DC module. Nonetheless, special care must be given when designing such an application, as pulsed waves may elicit abnormal biological effects [25].

For frequencies below 30 GHz, two effects of high peak energy deposition were reported: microwave hearing and the stun reaction (loss of consciousness). Due to these effects, IEEE C.95.1-2019 [18] states that the peak power density limits should be further limited for local exposures in both restricted and unrestricted environments for pulsed RF fields, as previously noted.

3.9 Closing remarks

The interaction of EM waves and biological tissue is a complex and demanding field that has been studied ever since the use of this radiation has been proposed for therapeutic purposes. As seen in this chapter, there is not yet a consensus amongst academics of what the consequences of the aforementioned interaction are for the human body. Some suggest EM waves can contribute to a plethora of health problems, others refute these claims.

In this chapter it was not possible to draw an unquestionable conclusion about the effects of EM radiation on our health. However, several independent organizations have thoroughly studied the available literature and developed standards based on scientific evidence which scientists and engineers must abide by when developing EM applications.

From the analysis presented in this chapter, some conclusions were drawn about WPT link parameters that can be manipulated to increase the power delivered to an IMD safely. According to [18] and equation 3.41, the use of pulsed fields is not beneficial to the subject at hand, as the total energy delivered to the IMD over the averaging time is one-fifth of the energy provided by a continuous wave. Pulsed signals can be of interest when high power is required to polarize electronic components of the implant (e.g., a rectifier's diodes), but since that is not the scope of this thesis, pulsed signals will not be explored. On the other hand, it is known that the SAR is calculated in small predefined volumes of the propagation medium with the electric field intensity in that volume. Together with the knowledge that the EM wave attenuates as it propagates over the tissues, it is expected that the maximum SAR occurs near the surface of the medium. With this in mind, it becomes apparent that if the EM fields come from different locations around the medium, multiple SAR hotspots will occur, but it is likely that they won't be higher than the SAR on the surface. Finally, knowing that the constructive superposition of several coherent polarized fields can significantly increase the power in the medium, the multiple EM fields should originate power hotspots inside the medium, which could be used to power an IMD. Consequently, the use of multiple transmitters is of high interest and will be implemented and tested in the following chapters.

3.10 References

[1] J. Lin, *Electromagnetic Fields in Biological Systems*, 1st ed. Boca Raton, FL: CRC Press, 2012.

[2] D. Pozar, *Microwave engineering*, 4th ed. Hoboken, NJ: John Wiley and Sons, Inc., 2011.

[3] D. Fleisch, *A Student's Guide to Maxwell's Equations*, 1st ed. New York: Cambridge University Press, 2008.

[4] F. Ulaby, E. Michielssen, and U. Ravaioli, *Fundamentals of Applied Electromagnetics*, 6th ed. Prentice Hall, 2010.

[5] R. W. Y. Habash, *Bioeffects and therapeutic applications of electromagnetic energy*, 1st ed. Boca Raton, FL: CRC Press, 2007.

[6] S. Baranski and P. Czerski, *Biological effects of microwaves*. Dowden, Hutchinson & Ross, 1986.

[7] IT'IS Foundation, "Dielectric Properties." [Online]. Available: https://itis.swiss/virtual-population/tissue-properties/database/dielectric-properties/. [Accessed: 31-Jan-2020].

[8] J. Lin, *Electromagnetic Interaction with Biological Systems*, 1st ed. New York: Plenum Press, 1989.

[9] C. A. Balanis, *Antenna Theory: Analysis and Design*, 3rd ed. New Jersey: John Wiley and Sons, Inc., 2005.

[10] International Commission on Non-Ionizing Radiation Protection (ICNIRP), *ICNIRP Guidelines for Limiting Exposure To Time-Varying Electric, Magnetic and Electromagnetic Field (up to 300 GHz)*, vol. 74, no. 4. 1998.

[11] D. J. Panagopoulos, O. Johansson, and G. L. Carlo, "Polarization: A Key Difference between Man-made and Natural Electromagnetic Fields, in regard to Biological Activity," *Sci. Rep.*, vol. 5, no. September, pp. 1–10, 2015.

[12] B. Greenebaum and F. Barnes, *Bioengineering and Biophysical Aspects of Electromagnetic Fields*, 4th ed. Boca Raton, FL: CRC Press, 2019.

[13] K. R. Foster and R. Glaser, "Thermal mechanisms of interaction of radiofrequency energy with biological systems with relevance to exposure guidelines," *Health Phys.*, vol. 92, no. 6, pp. 609–620, 2007.

[14] E. R. Adair and R. C. Petersen, "Biological effects of radio-frequency/microwave radiation," *IEEE Trans. Microw. Theory Tech.*, vol. 50, no. 3, pp. 953–962, 2002.

[15] C. Sage, "An Overview of Radiofrequency / Microwave Radiation Studies Relevant to Wireless Communications and Data," *Proceeding nternational Conf. Cell Tower Siting–Lingking Sci. Public Heal.*, pp. 513–521, 2000.

[16] C. K. Chou, "A need to provide explanations for observed biological effects of radiofrequency exposure," *Electromagn. Biol. Med.*, vol. 34, no. 3, pp. 175–179, 2015.

[17] M. Kato, *Electromagnetics in Biology*, 1st ed. Japan: Springer, 2006.

[18] Institute of Electrical and Electronics Engineers (IEEE), *IEEE standard for safety levels with respect to human exposure to electric, magnetic, and electromagnetic fields, 0 Hz to 300 GHz*, vol. 2019. 2019.

[19] IEEE Standards Association, *IEEE Standard for Safety Levels With Respect to Human Exposure to Radio Frequency Electromagnetic Fields, 3 kHz to 300 GHz*, vol. 2005, no. April. 2006.

[20] FCC, "OET bulletin 65: Evaluating compliance with FCC guidelines for human exposure to radiofrequency electromagnetic fields," vol. 65, 1997.

[21] International Commission on Non-Ionizing Radiation Protection (ICNIRP), "Guidelines for limiting exposure to time-varying electric and magnetic fields (1 Hz TO 100 kHz)," *Health Phys.*, vol. 99, no. 6, pp. 818–836, 2010.

[22] ICNIRP, "ICNIRP Note - Critical Evaluation Of Two Radiofrequency Electromagnetic Fields Animal Carcinogenicity Studies Published In 2018," *Health Phys.*, vol. 118, no. 00, p. 1, Aug. 2019.

[23] D. J. Panagopoulos, O. Johansson, and G. L. Carlo, "Evaluation of Specific Absorption Rate as a Dosimetric Quantity for Electromagnetic Fields Bioeffects," vol. 8, no. 6, 2013.

[24] Z. Sienkiewicz, E. Van Rongen, R. Croft, G. Ziegelberger, and B. Veyret, "A closer look at the thresholds of thermal damage: workshop report by an ICNIRP task group," *Health Phys.*, vol. 111, no. 3, pp. 300–306, 2016.

[25] S. Romanenko, R. Begley, A. R. Harvey, L. Hool, and V. P. Wallace, "The interaction between electromagnetic fields at megahertz, gigahertz and terahertz frequencies with cells, tissues and organisms: Risks and potential," *J. R. Soc. Interface*, vol. 14, no. 137, 2017.

CHAPTER 4 MULTITRANSMITTER WIRELESS POWER TRANSFER

State-of-the-art wireless power transfer solutions for implantable devices have been presented in Chapter 2. Despite the countless differences between the reported devices, whether in application or WPT method, they share a common feature: a single power transmission path is used between the source and the target.

The human body is a lossy medium which hinders WPT endeavours to devices implanted within it, as considerable losses occur. As a consequence, temperature can increase in the tissue, and therefore SAR must be closely monitored to ensure the safety of the patient. It is possible to affirm that, if extremely high SAR and its consequent biological effects were not a problem, simply increasing the transmitter's power output would be sufficient to meet the power demands of all devices. As such is not possible, then SAR regulation is the metric which limits the amount of power that can be transferred. Figure 4.1 presents the SAR inside a cylinder of human head phantom (ε_r=40 and σ=1.4 S/m [1]) when radiated by a dipole antenna placed one wavelength away and emitting 30 dBm of power at a frequency of 2 GHz.

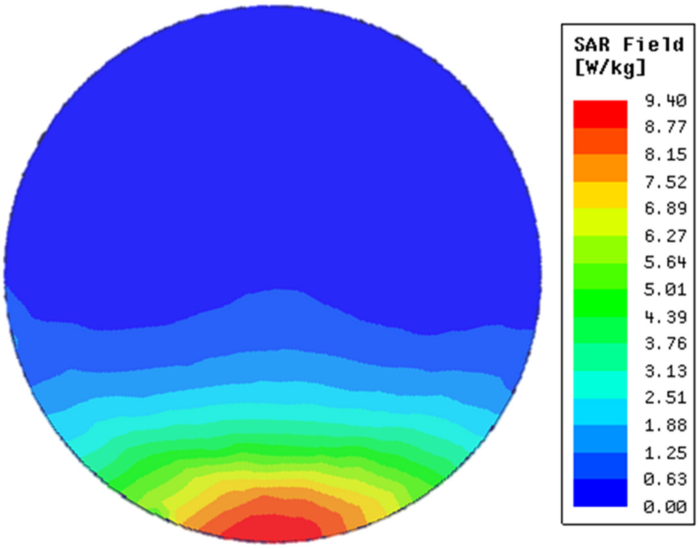

Figure 4.1 – SAR distribution inside a human head phantom (ε_r=40 and σ=1.4 S/m) radiated by a 2 GHz dipole placed 15 cm south of the phantom. It is visible that the highest SAR is located directly above the dipole's position.

As it can be seen, the highest SAR value occurs in the surface of the phantom, and it decreases with depth. Nevertheless, a huge portion of the volume's surface registers extremely low SAR levels, which indicates that an additional antenna could be used to transmit power through that direction, making use of multiple paths for energy inside the human body. Additionally, the signals transmitted by the antennas can be tuned to interact in a coherent manner at the region of the implant. With this, more power can potentially be delivered to the implant with the same maximum SAR value, as power is distributed throughout the tissue rather than being concentrated in a single path.

4.1 Proof of concept

The use of multiple transmitters to make the most out of the available biological medium volume presented itself as an interesting idea to be applied in the biomedical field. A first approach to the use of multiple transmitters is hereby proposed, simulated, and experimentally validated to assess its usefulness and practicality.

Operation frequencies in the low-GHz frequency range provide a good compromise between antenna size and signal attenuation while propagating in tissues [2], [3]. An HFSS model consisting of a cylinder with the dielectric properties of human head at 2 GHz [1] was designed, and two 2 GHz half-wavelength dipole antennas were placed one wavelength away from the center of the head phantom, both at a 60° angle from the symmetry plane, as shown in Figure 4.2.

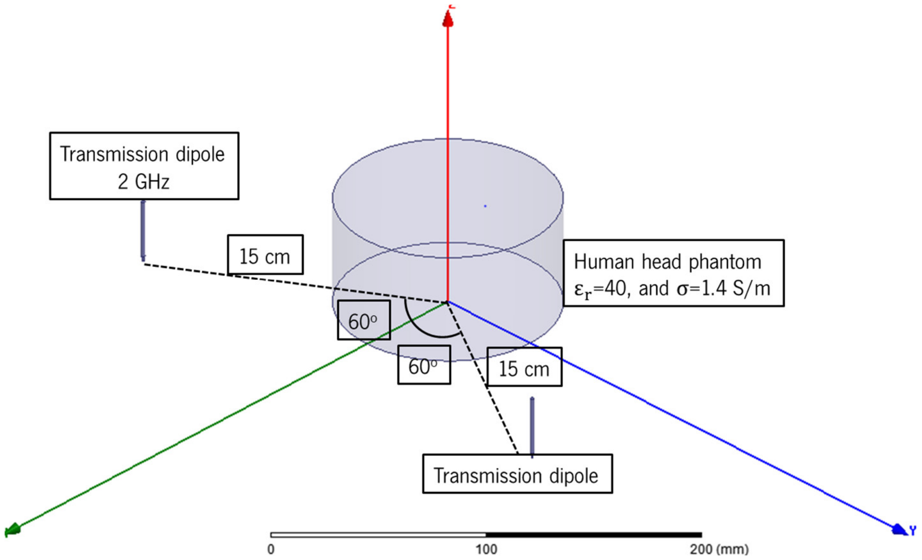

Figure 4.2 – HFSS model of the proposed multipath approach. A cylinder of human head phantom (ε_r=40 and σ=1.4 S/m) is placed 15 cm away from two dipoles that are 120 degrees apart from each other and operating at 2 GHz.

The model was simulated with either both dipoles activated, or only one of them. To keep comparisons as fair as possible, the output power of the transmitting antennas was adjusted so that the maximum SAR value on the human head phantom was the same in both scenarios. For one active transmission antenna an output power of 10.2 W resulted in a maximum SAR_{10g} value of 9.4 W/kg (SAR averaged over 10 g of tissue). With this, a maximum Poynting's vector magnitude of 10.9 W/m^2 was registered at the selected interest region, given by the square highlighted in Figure 4.3. For two transmission antennas, outputs of 11.2 W per antenna resulted in the same maximum SAR value, as confirmed by Figure 4.3 A and Figure 4.3 B. This increase in power per antenna for the same SAR_{10g} indicates that the signals from the two antennas destructively recombine in the maximum SAR regions. In this scenario, a maximum Poynting vector magnitude of 41.2 W/m^2 was registered in the same region of interest, an increase of nearly four-fold in available power in the same region.

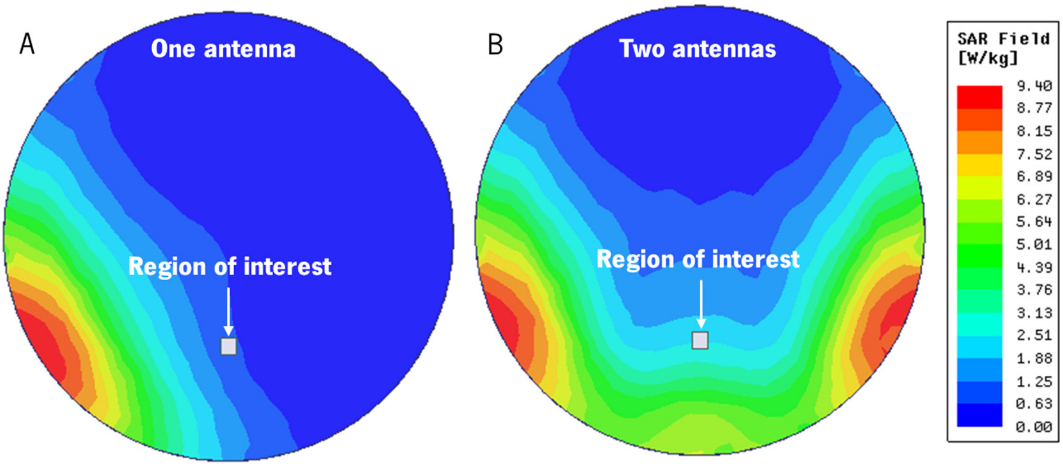

Figure 4.3 - Distribution of 10-g averaged SAR over the human body phantom for A) one transmission dipole radiating 10.2 W of power, and B) two dipoles radiating 11.2 W each. The maximum SAR_{10g} value is the same in both scenarios even though approximately twice as much power is being transmitted in B) since multiple propagation paths are being used.

A two-fold increase in received power was easily anticipated, as the total power being transmitted by the antennas has approximately doubled (from one antenna transmitting 10.2 W to two antennas at 11.2 W each). The remaining increase in available power occurs because the fields transmitted by each antenna meet and combine inside the head phantom, as shown in Figure 4.4, resulting in a four-fold increase of power, which is in accordance to equation (3.35).

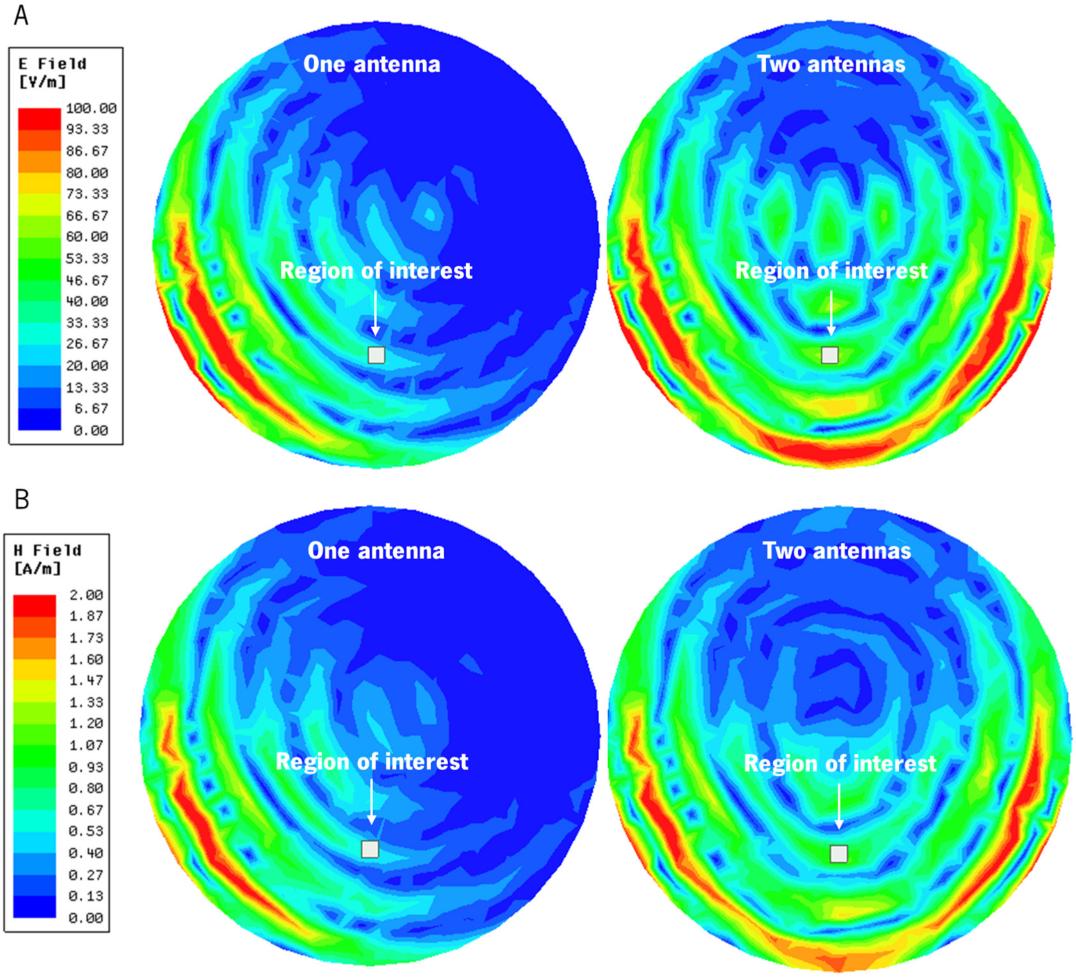

Figure 4.4 – A) Electric field and B) Magnetic field distribution in the human brain phantom for one and two transmitting antennas. When two transmitters are used, an increase in both field's intensity is registered at the interest region, as well as most of the studied area.

From the previous figure, it is possible to see that, at the region of interest, the E-field increases from around 30 V/m when one antenna is used to around 60 V/m when two antennas are transmitting. The H-field presents a similar behavior, increasing from around 0.6 A/m to 1.2 A/m. When using two transmission antennas, both the E-field and the H-field double in value in the region of interest. As available power is a product of these fields, it quadruples without increasing the maximum SAR_{10g}, since the maximum SAR_{10g} occurs in locations closer to the transmission antennas.

To validate the simulated results, the experimental setup of Figure 4.5 was developed. A LabView script running on a PC controlled the placement of a receiving dipole antenna in a 2D area inside the liquid phantom through two stepper motors, while simultaneously controlling a VNA. The RF management and amplification block were responsible for allowing easy commutation from operation with one or two transmitting antennas. The power measurement was performed inside an anechoic chamber to reduce interference from external elements.

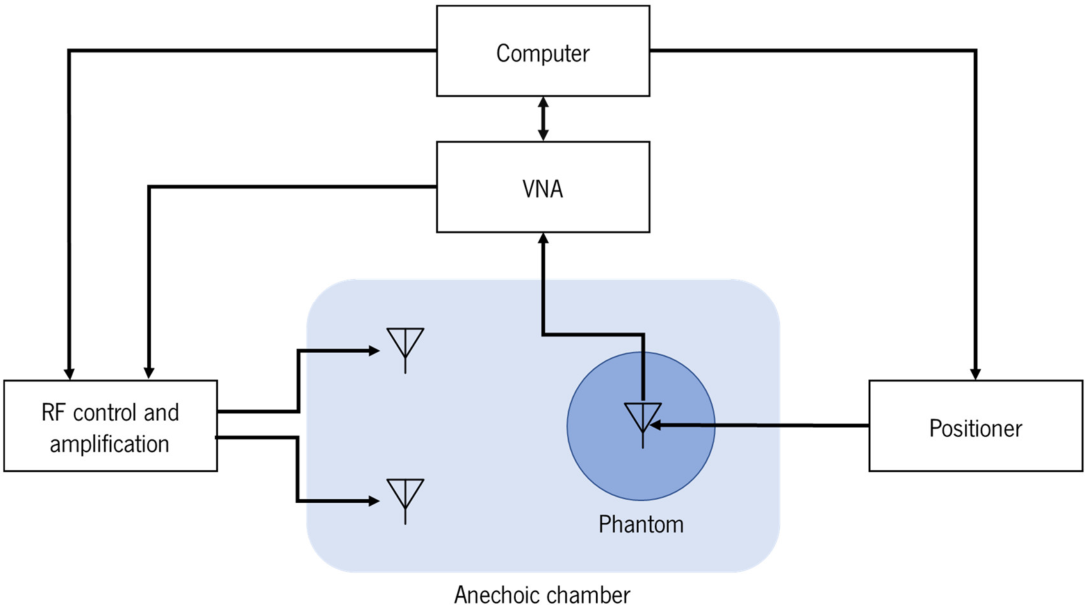

Figure 4.5 - Experimental setup for power measurement inside a liquid phantom. A Labview script controls the VNA, the RF control and amplification block, and the antenna positioner. The RF control and amplification block amplifies the RF signal generated by the VNA, and feeds it to either one or two transmission antennas.

The RF control and amplification block is made up of a splitter (Mini-Circuits ZAPD-2-272-S+) and two 10-W power amplifiers (Mini-Circuits ZHL-10W-2G+). The VNA is a Keysight E5071C.

For the single-path scenario, the VNA was connected directly to the power amplifier's input. In the multi-path scenario, the signal from the VNA passed through the splitter, which sent half the original power to each path, but the same total power. The measurement results are presented in Figure 4.6.

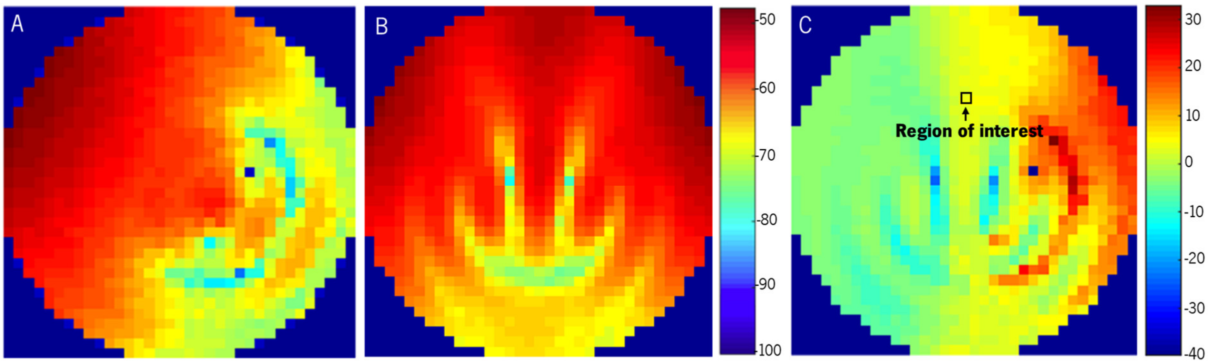

Figure 4.6 - Power distribution inside the human brain phantom for A) one transmitting antenna, B) two transmitting antennas (scale in dBm), and C) difference of A and B, where a clear increase of power availability over most of the volume is verified (scale in dB).

Analyzing the region of interest, which coincides with the one from the simulation, it is possible to determine that there is an approximately 3.0 dB power increase in the two antennas versus the single antenna scenario. This means that the available power in the interest region doubles, even though each antenna is transmitting half the power as in the single-transmitter scenario.

The possibility of combining the use of two antennas with beamforming principles also became an interesting opportunity. As such, the RF control and amplification block of the previous system was adapted to allow the relative phase of the signals in two antennas to be modified. The schematic of Figure 4.7 represents the updated block.

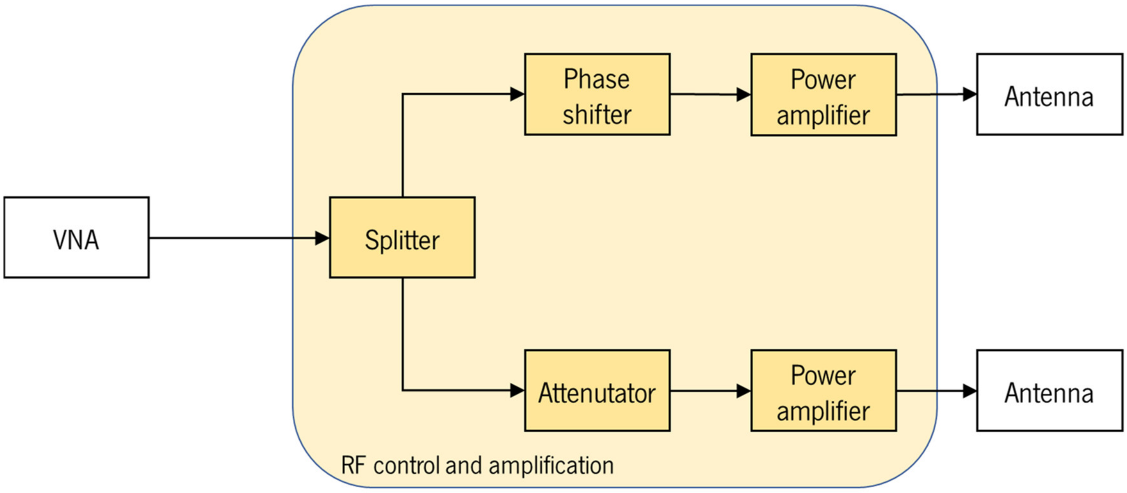

Figure 4.7 - Schematic representation of the RF control and amplification block and its input and outputs.

The signal generated in the VNA was passed through a splitter (Mini-Circuits ZAPD-2-272-S+), and one of the resulting channels was connected to a phase shifter (Peregrine Semiconductor PE44820), while the other went through an attenuator in order to compensate for the power loss that the phase shifter adds to the first channel. Then, the signals from both channels were amplified (Mini-Circuits ZHL-10W-2G+) and directed to the antennas. With this setup, the phase difference between the two channels could be manipulated by the phase shifter. Figure 4.8 presents the power distribution inside the phantom for two transmitters with the same phase and with a 60-degree phase difference. As it can be seen, the location of the hot and cold spots shifted due to the different phases, as expected. With this, it is possible to conclude that the power distribution inside the phantom can be controlled with phase adjustments.

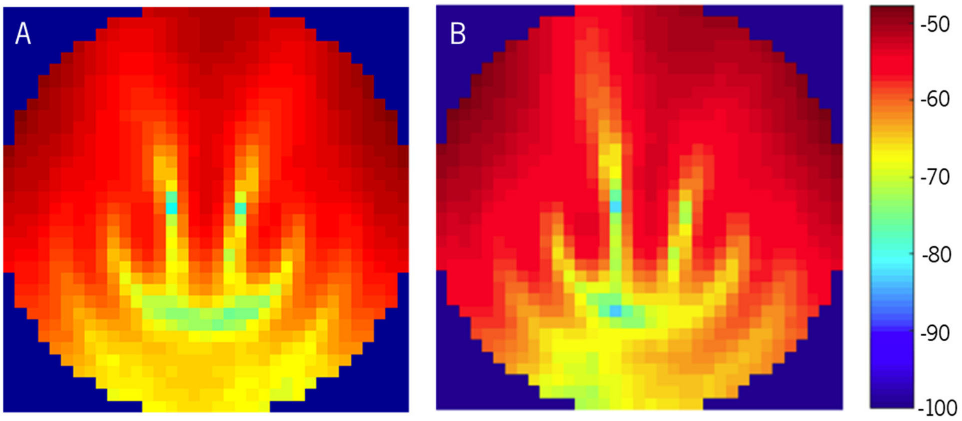

Figure 4.8 - Power distribution inside the phantom with A) two transmitters sending signals with the same phase and B) with a 60 degree phase difference (scale in dBm).

Having achieved promising results using two transmitters, naturally the development of this idea progressed towards a more mature state. Increasing the number of transmitters presented itself as an immediate improvement to this system. Furthermore, being able to control the phase of the transmitted signals was an interesting opportunity to increase the power delivered to an implant. The development of a system with multiple transmitters and increased control over the transmitted signals is presented in the following sections.

4.2 Multitransmitter WPT

Transmitting power to an implantable device through different paths in the tissue has demonstrated to be a feasible approach with potential to increase the power delivered to a device, which can enable a multitude of applications that have so far been prohibitive due to volume and power constraints.

4.2.1 Number of transmitters

The development of the multitransmitter system started by determining an adequate number of transmitters to be used. If too few transmitters are used, then the available volume for energy propagation is not fully taken advantage of. On the opposite hand, if too many transmitters are used, they will be placed close together, and consequently their propagation paths can conflict, increasing the SAR and limiting their power output. Furthermore, system costs have also to be considered, as using more transmitters will inherently result in higher costs.

To determine the number of transmitters, it was considered that the power would be transmitted in one hemisphere of the phantom, i.e., the antennas would be equally distributed over 180 degrees. If the architecture of the system were to change (for example, if the full 360 degrees were used) then a new analysis could be performed to assess if more transmitters would be a useful addition.

A multi-layer human head phantom model was designed in HFSS, as shown in Figure 4.9. The layers' properties are specified in

Table 4.1. The use of the multi-layer model is justified by the increased accuracy it provides, given the importance of the task in hand.

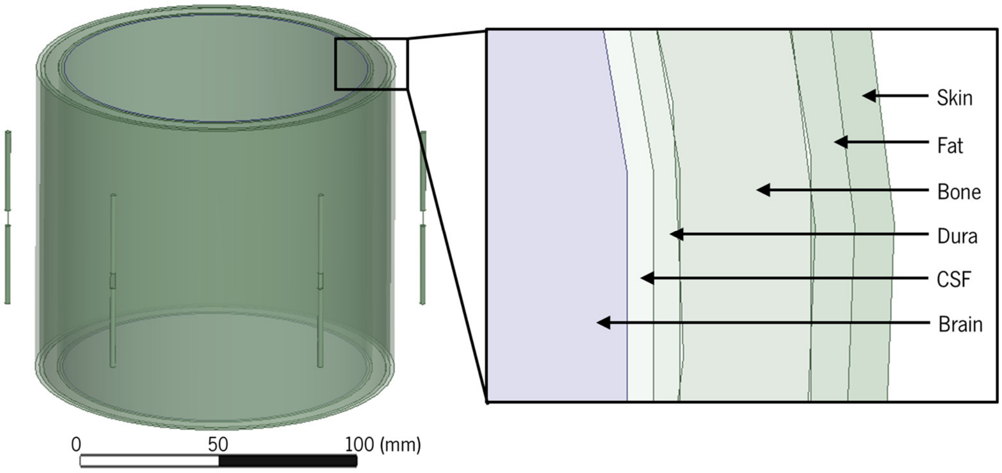

Figure 4.9 - Multi-layered human head model, with four transmitters around it. The inset details the layers' composition.

Table 4.1 - Dimension and dielectric properties at 2 GHz of the layers that constitute the multi-layered model [4], [5].

	Skin	**Fat**	**Bone**	**Dura**	**CSF**	**Brain**
ε_r	38.6	11.0	19.1	42.6	66.9	36.7
σ (S/m)	1.3	0.2	0.7	1.4	3.1	1.0
ρ (g/L)	1100.0	1100.0	1850.0	1030.0	1030.0	1030.0
Thickness (mm)	1.5	1.5	5.0	1.0	1.0	55.0

The number of antennas surrounding the phantom was varied across models to determine a good configuration. Sets of four, five, six, seven and eight antennas were used, and the SAR was evaluated in two scenarios. First, each of the antennas transmits 1 W of power (Figure 4.10). In the second scenario, the transmitted power was set so that the maximum SAR_{10g} would be 10 W/kg, and the power availability in the brain phantom was calculated through the magnitude of the Poynting vector (Figure 4.11).

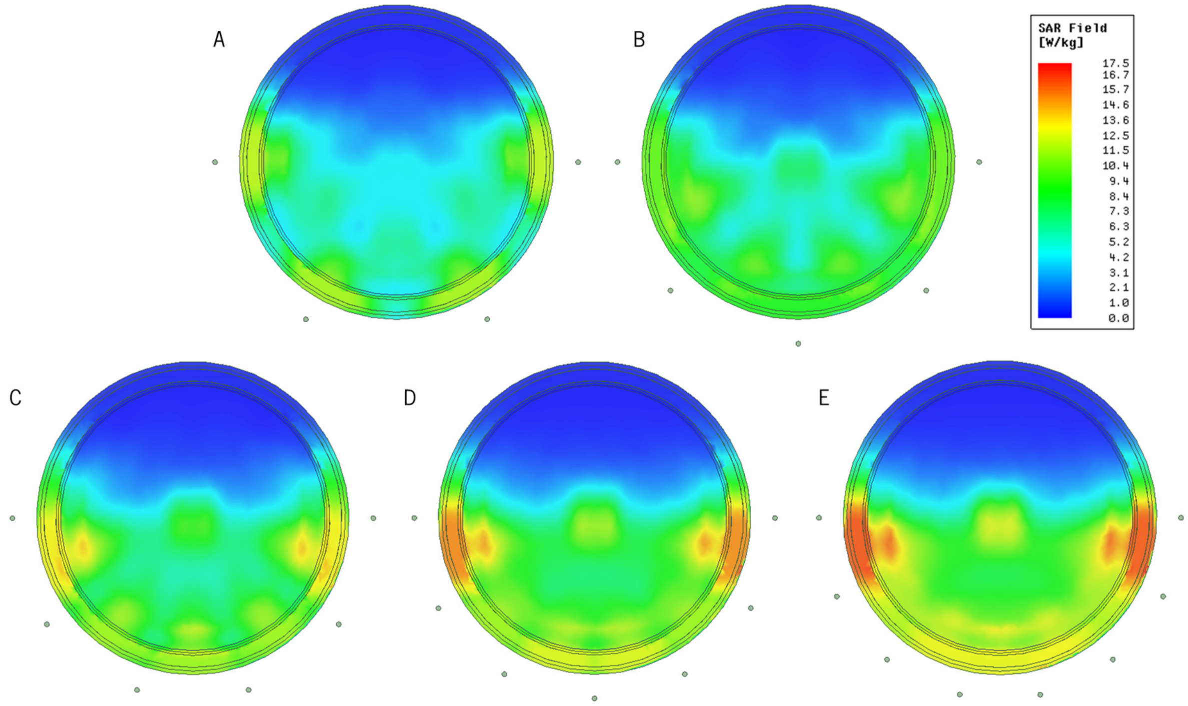

Figure 4.10 – SAR_{10g} distribution in the multi-layered model for A) four, B) five, C) six, D) seven and E) eight antennas. The power transmission per antenna is 1 W.

When the same power is transmitted in all antennas (Figure 4.10), it is possible to observe that the SAR_{10g} increases with the increase in transmitters, as these become closer to one another, hinting that too many would hinder the system's performance, as neighbouring antennas would send energy through the same path. It is also noticeable that the higher the number of antennas, the more power is available deep within the tissue, which is due both to the increased total power being transmitted and the constructive interaction between the different signals inside the tissue.

In the second study, the Poynting vector's magnitude in the brain was calculated for variable antenna numbers and power but keeping the maximum SAR_{10g} the same in all scenarios (Figure 4.11). From the results, it can be stated that a higher number of antennas results in a smaller maximum power, but a more uniform distribution over the southern hemisphere of the brain phantom, since the maximum power is higher for fewer antennas, but cold spots are more prevalent.

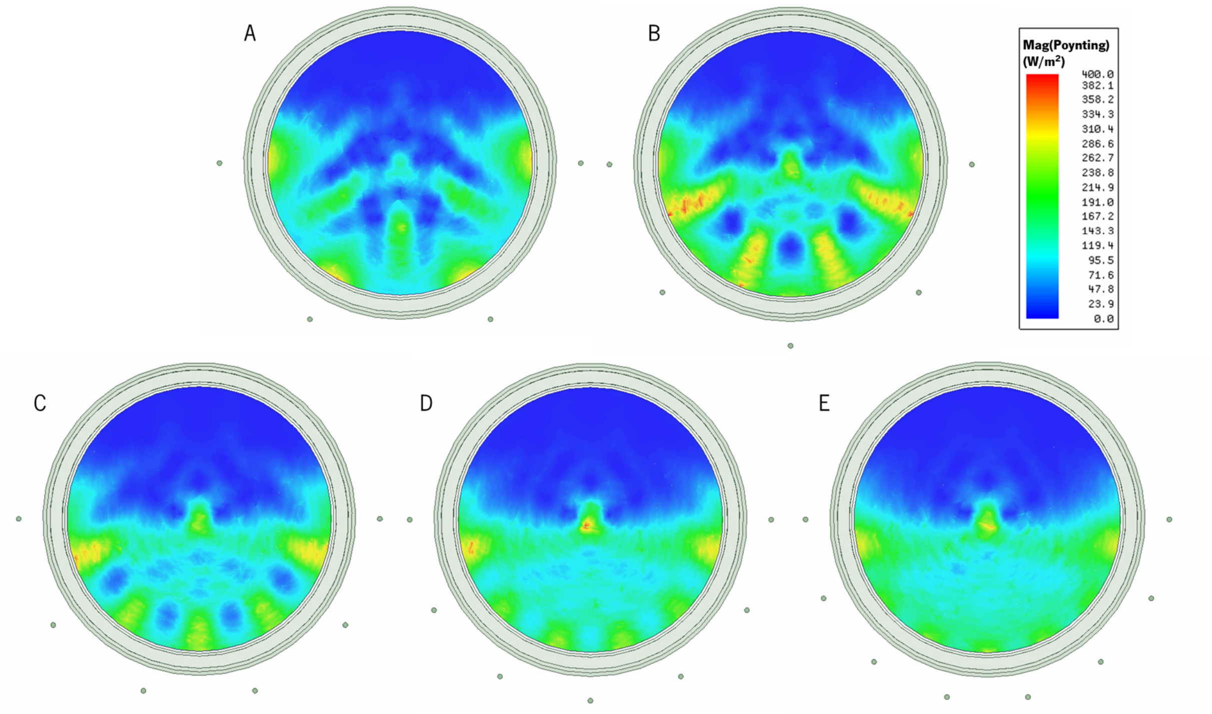

Figure 4.11 – Magnitude of the Poynting vector inside the brain tissue for four antennas radiating A) 0.9 W each, B) five antennas radiating 0.89 W each, C) six antennas radiating 0.65 W each, D) seven antennas radiating 0.58 W each, and E) eight antennas radiating 0.52 W each. The SAR_{10g} is 10 W/kg in all the scenarios.

Gathering the findings of the two previous analysis, the decision on the number of transmitters to use in the system was made. On one hand, fewer antennas keep the SAR lower for the same power, which means that the antennas are not sharing the same energy propagation path. On the other hand, the distribution of power in the phantom becomes less uniform. Even so, and especially considering that the objective of the system is to concentrate power on a given spot and not spreading it equally across the entire volume, this analysis suggests using fewer antennas, eliminating the seven and eight antenna scenarios where SAR is much higher. Removing the SAR from the equation and looking simply at the power distribution, which was done in the second analysis, indicates again that more antennas lead to a more uniform power distribution, but fewer antennas lead to higher power levels inside the brain as is visible in Figure 4.11 A-C. Again, as power focusing is a goal, the seven and eight transmitter scenario becomes dispensable, even more so bearing in mind that the higher the number of transmitters, the higher the cost of the system will be.

In conclusion, six transmitters will be considered for developing the system, since it will then be possible to use all six or a smaller number through deactivation of channels. A case could be made in favour a system for only four transmitters, but future variations on the arrangement of antennas could benefit from having more transmitters (*e.g.,* if the whole circumference of the phantom were used), and deactivating some channels is a simple task, while adding channels to the system would require significant cost and effort.

4.2.2 Tracking: principle of operation

With the use of multiple transmitters proving to be a promising approach to increase the power transmitted to an implant, this will be the base of the developed WPT system. Borrowing concepts from radar theory, by controlling the phase difference between the transmitters' signals it is possible to concentrate power in certain areas of the brain volume, thus allowing for an even higher increase in power availability for the implant.

Focusing power at the implant, hereby referred to as tracking, is not a simple task, however, especially considering that the implantation environment is highly inhomogeneous and anisotropic. Furthermore, it varies greatly between individuals and application. Consequently, a feedback must be provided by the implant for tracking and power focusing to be possible. Inspired by the work presented in [4], the implanted device will send a short duration, low power RF signal, hereby called beacon. The biological tissues will interact with it, and each of the transmitter antennas will receive the beacon with a relative phase difference that can be calculated. The phase difference at each transmitter antenna will be due to the different path the signal travels between the implant and the receivers, and the interactions of the signal with the medium along its propagation.

By taking the measured beacon phase differences at each antenna, it is possible to transmit power to the implant with each antenna transmitting an RF signal with the conjugate value of the measured phase.

Considering the beacon signal $S(t)$ transmitted by the implant:

$$S(t) = A_0 \cos(\omega_0 t + \varphi_t) \tag{4.1}$$

where A_0 is the amplitude, ω the angular frequency and φ_t the phase. After transit time T_i, the signal received by power transmission antenna i is given by:

$$S_{r,i}(t) = A_1 \cos(\omega_0 (t - T_i) + \varphi_t) = A_1 \cos(\omega_0 t - \omega_0 T_i + \varphi_t) \tag{4.2}$$

After performing phase-conjugate operation, the powering signal transmitted by antenna i is:

$$P_i(t) = A_2 \cos(\omega_0 t + \omega_0 T_i - \varphi_t) \tag{4.3}$$

On its way to the beacon's source, there is also a transit time T_i, and the signal reaching the implant is:

$$P_r(t) = A_3\,cos(w_0(t - T_i) + \omega_0 T_i - \varphi_t) = A_3 \cos(\omega_0 t - \varphi_t) \qquad (4.4)$$

Therefore, there is no difference between the beacon signal and the powering signal at the implant location, except for the phase reversal. As such, the total signal returned to the beacon's source is the coherent addition of the signals transmitted by the various power transmission antennas [5].

For example, in a two-transmitter scenario, if the first transmitter, T1, receives the implant's beacon with phase 0 (reference signal), and T2 receives it with phase j, power transmission is performed by sending the power signals with phases 0 and -j, respectively. According to the self-phasing technology theory [5], the components of the fields of each transmission antenna will recombine with the same phase at the location of the beacon's source, i.e. the implant, thus creating a power hotspot in this location.

The principle of operation is demonstrated in Figure 4.12, where several power transmitters T are randomly placed around a receiver R and E-field plots are presented. When the receiver transmits a beacon (A), it propagates through the medium and reaches each of the transmitters with a different phase. Then, all the transmitters start sending power with a phase delay according to the received beacon and it culminates in a power hotspot in the receiver (B), which is not observed when the transmitters are all in-phase (C).

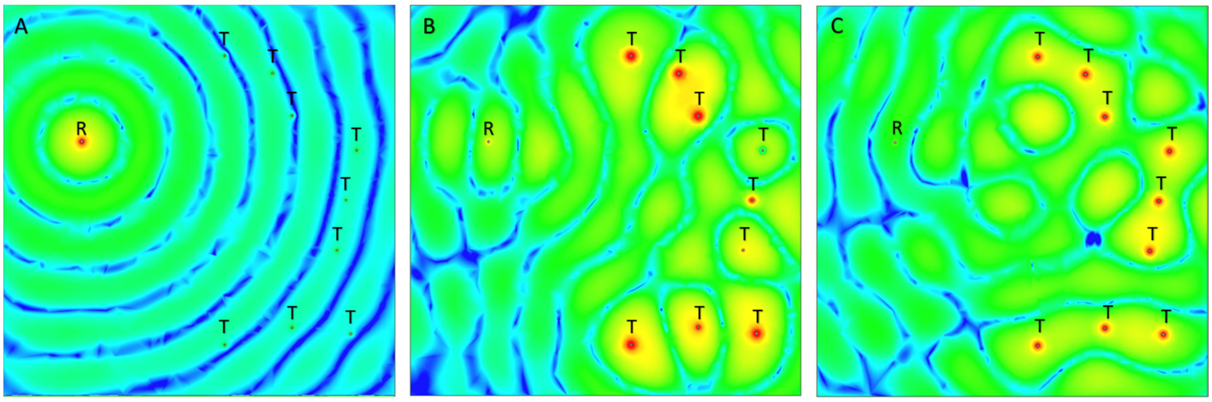

Figure 4.12 - Visualization of the principle of operation of the proposed device. A) Several transmitters are scattered around a receiver, which transmits a beacon signal that reaches the transmitters at different phases. B) The transmitters then transmit with the opposing phase and the waves interact constructively at the location of the beacon's source. C) When the transmitters emit signals with the same phase, the hotspot is not verified in the receiver's location.

4.2.3 System adaptability

In order to verify the adaptability of the system, and thus its potential tracking capabilities, an HFSS simulation was performed where six antennas were placed around a water volume, as shown in Figure 4.13. Water is commonly used as a first approach to a body phantom, as biological tissues are mainly composed of water, and this medium is going to be used for the system's validation measurements.

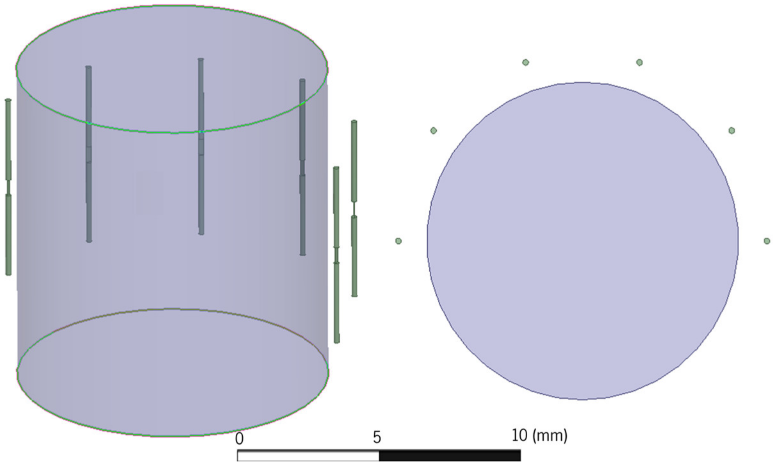

Figure 4.13 - Water phantom model with six transmitters placed 15 mm cm away from the surface. Each transmitter is equally spaced from one another across one hemisphere of the phantom.

Figure 4.14 demonstrates interest points that represent possible implant locations, and the distribution of the Poynting vector's magnitude inside the phantom when the transmitted signals' phase is the same across all six antennas. As it can be seen, there are locations inside the phantom where the available power is very little, due to destructive recombination of the power signals.

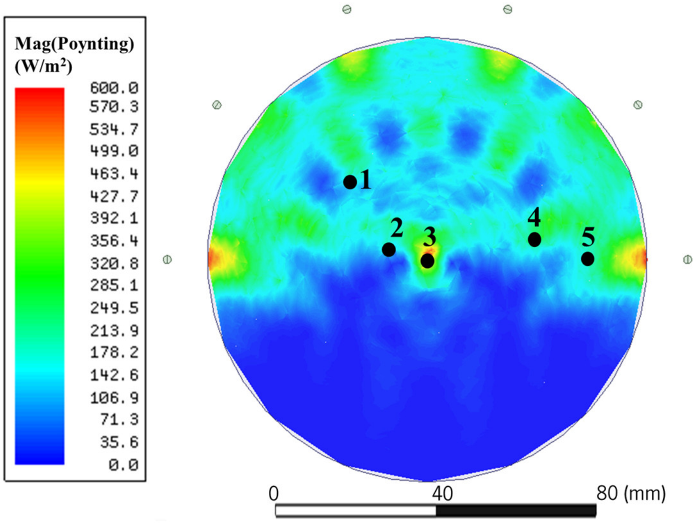

Figure 4.14 - Poynting vector magnitude inside the phantom for six transmitters emitting power with the same phase. Five points of interest are identified for possible implant location.

The tracking of the implanted device is performed as previously detailed. In the simulation environment, an antenna is placed at each interest point to provide the beacon for the phase adjustment of the transmission antennas and consequent focusing of the transmitted power. Figure 4.15 presents the Poynting vector's magnitude in the phantom for each of the five interest points along the path. As it can be seen, the power distribution varies drastically in each case and, unlike what happened when no tracking was used (Figure 4.14), points P1 and P2 were no longer located in a "cold" region, as the recombination of the transmitted power signals was such that the maximum possible amount of power was made available at each point. In Table 4.2 are displayed the values of the Poynting vector's magnitude in each point for a single transmitter, and six transmitters with and without tracking. The transmitted power by each antenna was the same in all scenarios. The one-antenna scenario resorts to the antenna on the right-hand side of the phantom, closest to P5.

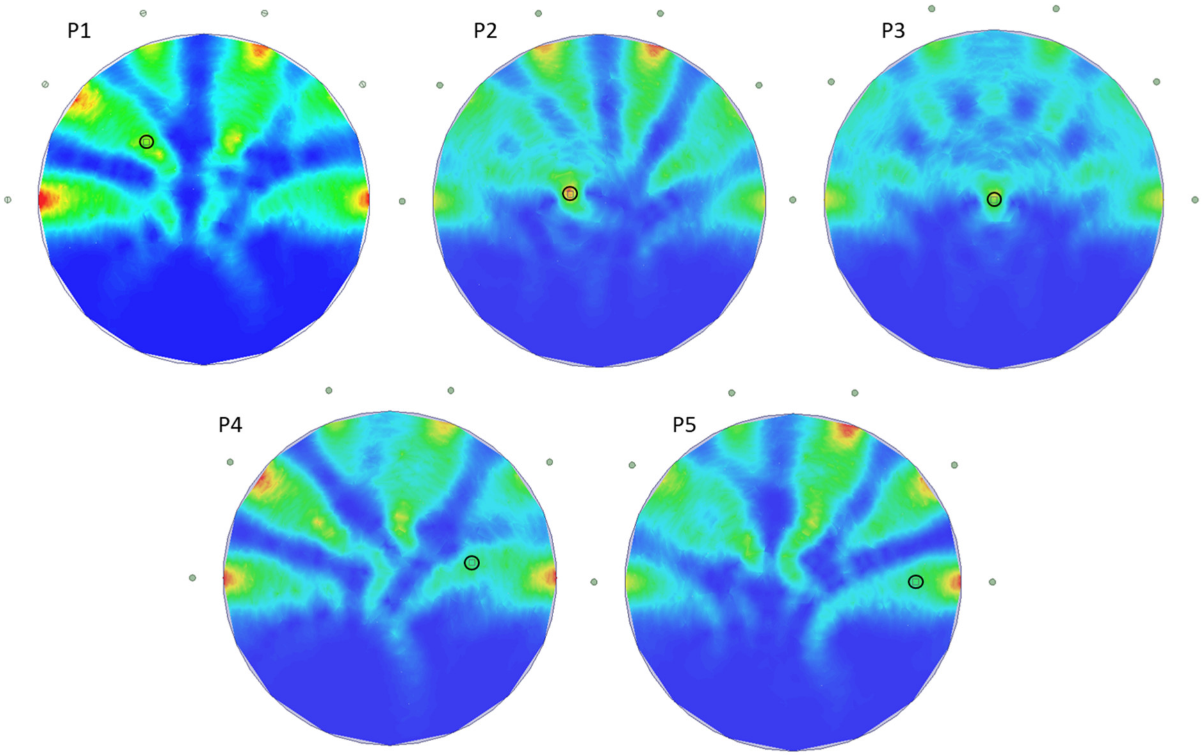

Figure 4.15 - Poynting vector magnitude plot for each of the five interest points along the path of the implantable device for the tracking application.

As it can be seen, the single-antenna scenario is underperforming comparatively to the in-phase six-antennas one in every studied location except for P5, which can be justified by a possible destructive recombination of the signals of the nearby antennas when no tracking is used. For the remaining positions, the existence of antennas around the phantom ensures that there are always antennas closer to the implant, rather than when only one is used. This, allied to the constructive recombination of the signals, results in an increase in available power in the remaining positions.

Table 4.2 - Poynting vector magnitude at the interest area for one transmitter, six transmitters without tracking, and six transmitters with tracking.

	P1 (W/m^2)	**P2 (W/m^2)**	**P3 (W/m^2)**	**P4 (W/m^2)**	**P5 (W/m^2)**
1 antenna	4.0	28.0	41.0	127.0	317.0
6 antennas (no tracking)	187.0	232.0	536.0	216.0	247.0
6 antennas (tracking)	487.0	803.0	537.0	349.0	356.0

Comparing both scenarios, with and without tracking, it is possible to see that, for P1 and P2, the available power drastically increases when tracking is used, as these no longer correspond to “cold” areas. P3 remains the same, as expected, since it is in the geometric centre of the phantom, i.e. when no tracking is used, the signals of the transmitters will constructively recombine in that location exactly like when tracking is used. P4 and P5 have registered a smaller increase of power, which can be explained by the fact that these points are located much closer to the right-hand side antenna than any of the others. Consequently, the contribution of the remaining antennas is much smaller, making for a result similar to the one obtained when no tracking was used. Still, a slight improvement was registered in both locations with the use of tracking.

The application of self-phasing theory to implantable devices provides immense advantages for a WPT approach. The received signal can be transmitted back to the source without precise confirmation of the source location and movement, and without concern for medium-induced perturbations in the propagation of the wave [5], as demonstrated by the results of Figure 4.16, where a propagation medium of permittivity 49 has several randomly placed obstacles with permittivity ranging from 1 to 100 (A and B). As it can be seen, the transmitters can still concentrate power in the receiver’s location (C), just as it happened in Figure 4.12 B.

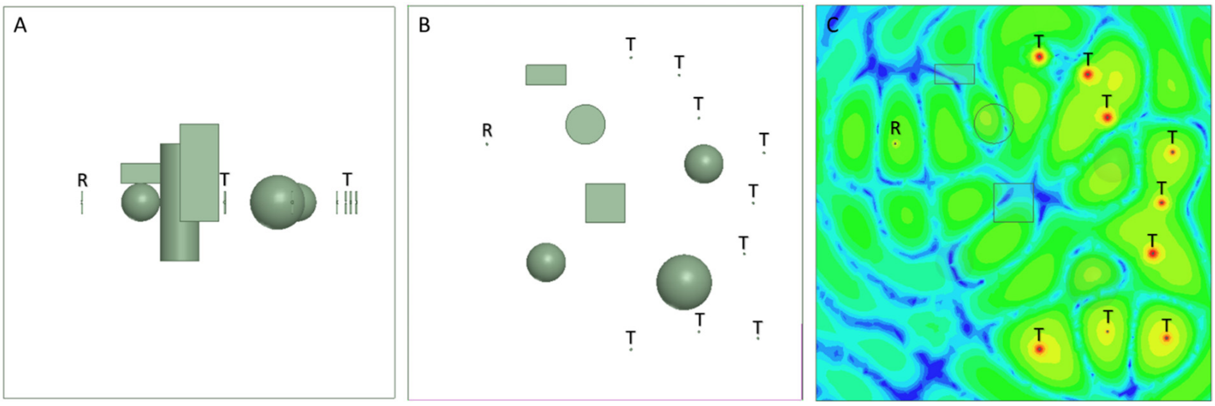

Figure 4.16 - A, B) Obstacle distribution inside the propagation medium. C) Electric field hotspot when the transmitters are configured as described.

With this method, it is possible to power a device implanted anywhere in the human body without prior knowledge of its environment. Furthermore, as the described operation of beacon feedback and power transmission could be repeated periodically in order to adjust the power hotspot's location, tracking of a moving implant becomes possible (for example a device that travels in the bloodstream or an endoscopic capsule). Finally, this system is not limited to use in biological medium and can also be used for applications in free space, which means this system has a plethora of possible applications, such as powering a device on a rat inside a cage.

With the previously reported results, the setup's principle of operation has been validated. Multiple transmitters increase the power availability for the implant. Additionally, the technique for focusing power at the implant's location has been demonstrated and it has shown to greatly increase the power availability. Therefore, the following sections report on the development of a WPT system that employs the previous findings.

4.2.4 System requirements

The WPT system is required to allow for the maximum power to be transmitted to the device, whether it is stationary or moving along a random path within the volume (e.g., a blood vessel). To accomplish this, it must be capable of tracking the implanted device and concentrate power on its location. Additionally, for it to be universal, it must be capable of performing as expected independently of the medium's shape and constituents, i.e., it must treat the medium as a black box. Finally, operation at 2.45 GHz is advantageous, since this frequency is part of the ISM band and, given that it is a commonly used frequency for commercial applications, there is a wide variety of off-the-shelf components that can be used.

4.2.5 System description

The main constituents of the multitransmitter WPT system, represented in Figure 4.17, are the transmission and reception blocks. The reception block is responsible for reading the phase difference of the beacon between the different antennas of the array. As such, it requires access to the antennas, and it must then measure this relative phase difference. The transmission block is where the WPT signal is generated, amplified, and then fed to the antennas of the array with a different phase in each antenna. As both the transmission and reception blocks require access to the antenna array, an RF switch (Mini-Circuits ZX80-DR230-S+) is required. Finally, the entire system is controlled by a control and processing unit (Arduino MEGA), which is responsible for timing the beacon reception and the power transmission and guaranteeing that the switches and amplifiers are correctly activated. Additionally, it is used to perform the required calculations regarding phases.

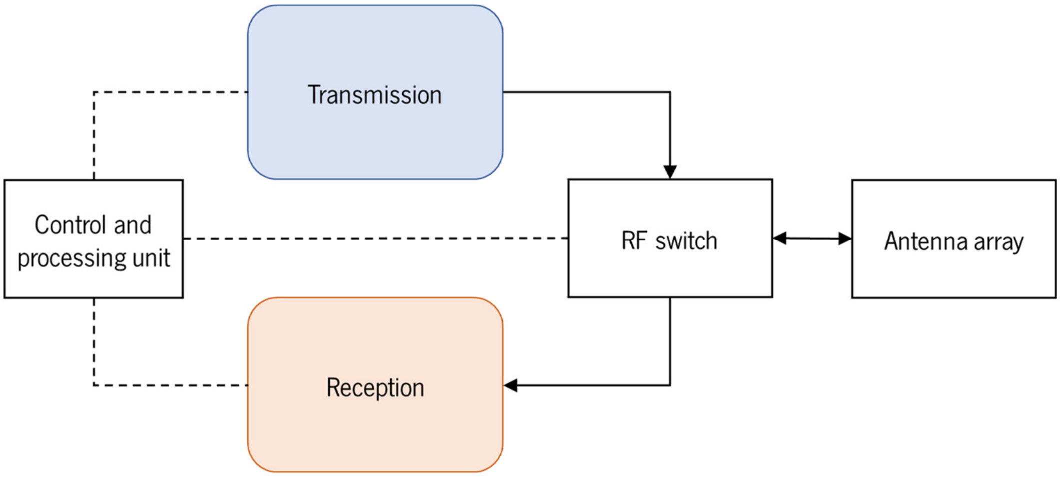

Figure 4.17 -Schematic representation of the WPT system’s main blocks.

The following sections of this work will go into further detail on the most important blocks of the system: the transmission and the reception.

4.2.5.1 Transmission

The transmission block, responsible for sending the power signals to the antennas with different phases, is represented in Figure 4.18. The signal is generated by a VCO (Mini-Circuits ZX95-3800A-S+) and connected to an RF switch (Mini-Circuits ZX80-DR230-S+) that will either connect the VCO to a 50-Ohm load (Mini-Circuits MCL ANNE-50L+) when the transmission is turned off, or to a 6-way splitter (Mini-Circuits ZB6PD-2-S+) when the transmission is on. Each of the first five outputs of the splitter are connected to a phase shifter (Peregrine Semiconductors PE44820), a power amplifier (Skyworks

SKY66294-11) and an RF switch (Mini-Circuits ZX80-DR230-S+). This RF switch allows for the system to access the same antenna for both transmission and reception, as it connects the antenna to either one of them. The sixth channel is used as a reference, i.e., its transmission phase is constant, and the remaining channels are configured through their respective phase-shifters relative to this one. To compensate for the phase-shifter's attenuation in the other five channels, an attenuator (2x Mini-Circuits VAT-3+) is added in the reference, in order to keep the output power balanced in all antennas. Finally, the switches are controlled by the control and processing unit. The latter is also responsible for programming the phase shifter and turning the VCO and power amplifies on and off.

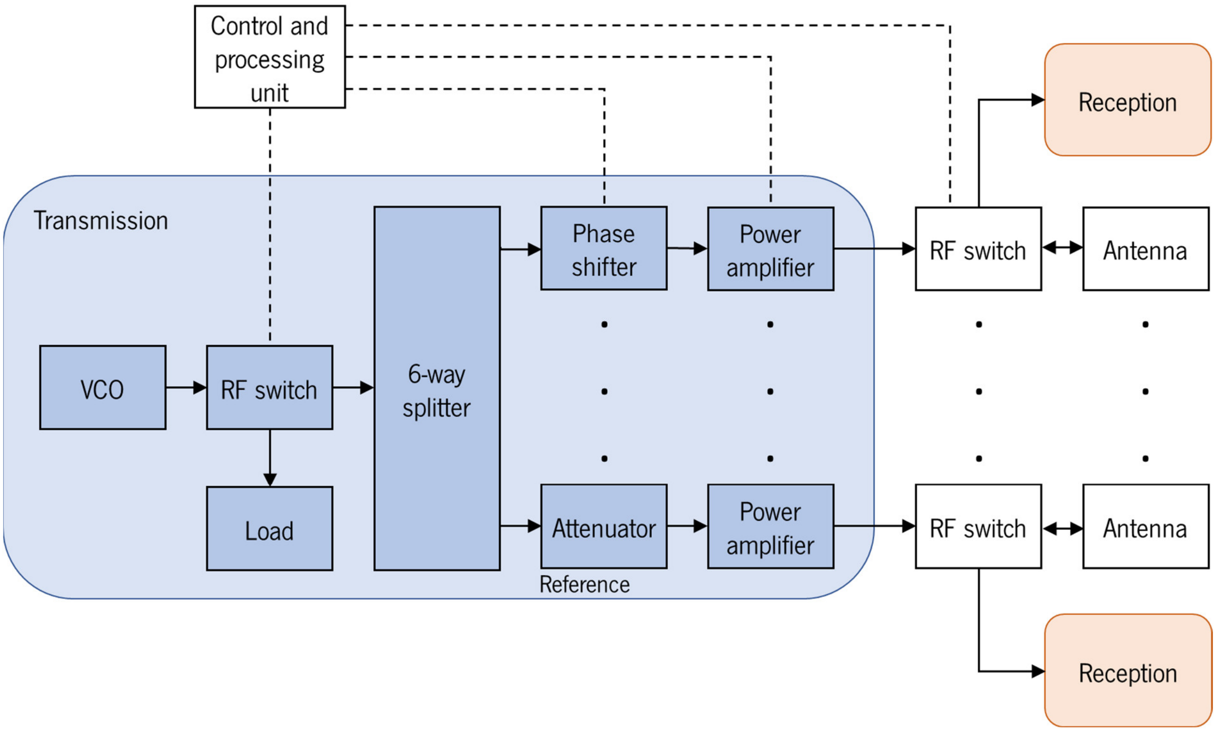

Figure 4.18 - Block diagram of the WPT system transmission module.

4.2.5.2 Reception

The first step of the reception phase consists in the transmission of the beacon by the implant. The antennas receive the beacon and the RF switches direct each of their signals to the reception block, which is represented in Figure 4.19. In the reference channel, the signal goes through an amplification and filtering stage (description added below) before reaching the phase detector (Analog Devices AD8302), which compares the signal from the reference antenna to each of the five channels' signals. For the other channels, the RF switches connect each one of them, in turns, to the reception block, so that only one of them is compared to the reference at a time. The channels that are not being compared are directed to a 50 Ohm load. The selected channel's signal goes through a 6-way combiner (Mini-Circuits ZB6PD-2-

S+), an amplification stage and a bandpass filter. After this, the signal is fed to a 90-degree splitter (Mini-Circuits ZX10Q-2-27-S+), which outputs the original signal at one port and a 90-degree phase-shifted copy of this signal at a second port. Then, an RF switch (Mini-Circuits ZX80-DR230-S+) directs each of these two signals into the phase detector, one at a time. The phase detector then compares the phases between the reference and each of the signals from the 90-degree splitter and outputs a DC value for each comparison, whose noise is attenuated with a passive RC low pass filter and connected to the control and processing unit. This is repeated for the five channels.

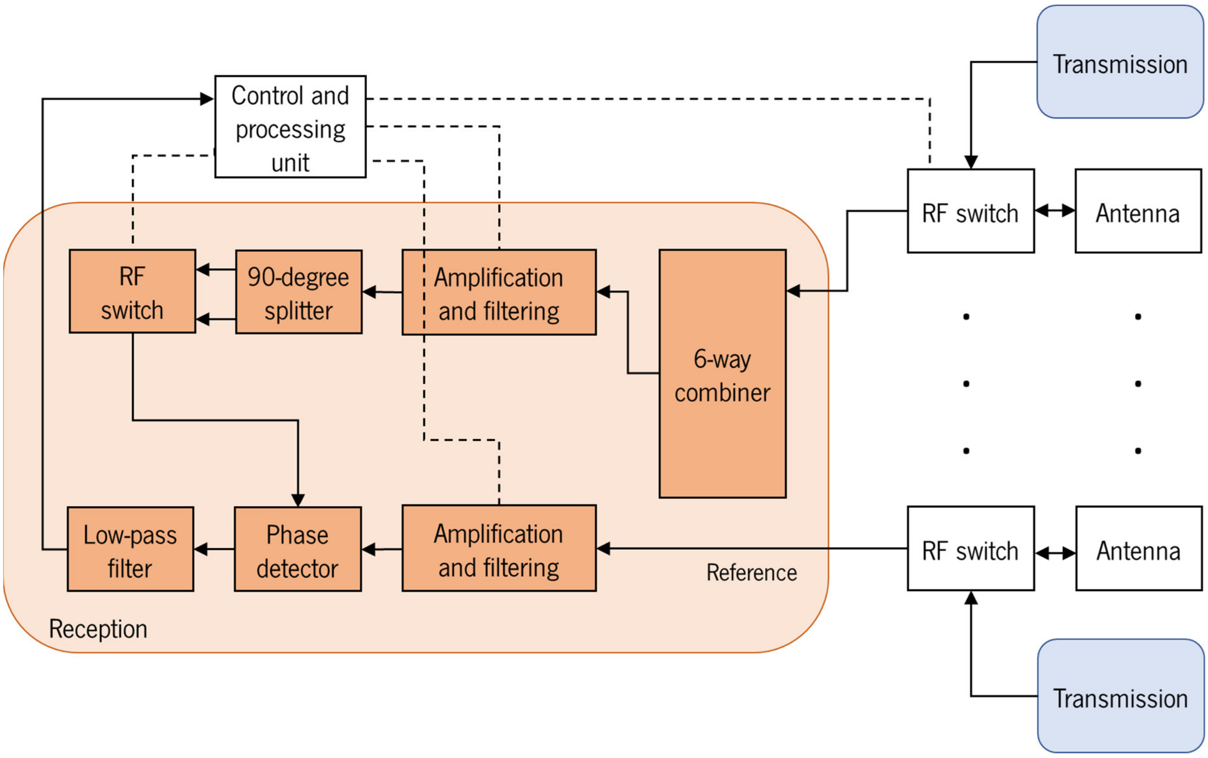

Figure 4.19 - Block diagram of the WPT system reception module.

The beacon's source can be located anywhere in the black-box medium, therefore it can be very distant or very proximate to an antenna. As such, the beacon power level can vary greatly between antennas and different source placements. Consequently, the amplification and filtering stage of the reception consists of a cascade of amplifiers with variable and self-adjustable gain and a bandpass filter. This solution can guarantee enough power at the inputs of the phase detector to allow for its correct operation for a wide range of beacon power levels.

The amplification and filtering stage starts with a low noise amplifier (Mini-Circuits ZX60-272LN+), followed by two variable gain amplifiers (VGA) (Mini-Circuits DVGA1-242APP+) in series. Given the high maximum gain achievable by this series of amplifiers, around 54 dB, the reception stage is susceptible to interference caused by other 2.45 GHz sources either from the environment (e.g., smartphones) or from the WPT system itself (e.g., the VCO). Thus, the three amplifiers are placed inside a faraday cage for increased isolation. Following the amplification, a power limiter (Mini-Circuits VLM-73-1W-S+) is added to protect the system from high amplification output power, which could happen due to an unexpected interference or in case of a system failure. Followingly, the signal is filtered by a bandpass filter (Crystek Microwave's CBPF-2441), which has a centre frequency of 2441 MHz and a bandpass width of 83.5 MHz. At 2.45 GHz, it has a gain of -1.55 dB [6]. The signal is then passed through a bidirectional coupler (Mini-Circuits ZABDC10-25HP) which couples the signal with a 10 dB attenuation to a power detector (Analog Devices DC1120A). The power level of the beacon after amplification and filtering is measured and the control and processing unit adjusts the gain of the VGAs so that the power of the signals at the input of the phase detector is between -10 dBm and -30 dBm, which can be achieved for beacon powers as low as -90 dBm in the reference channel and -75 dBm in the five remaining channels. A diagram of the implemented amplification and filtering stage is presented in Figure 4.20.

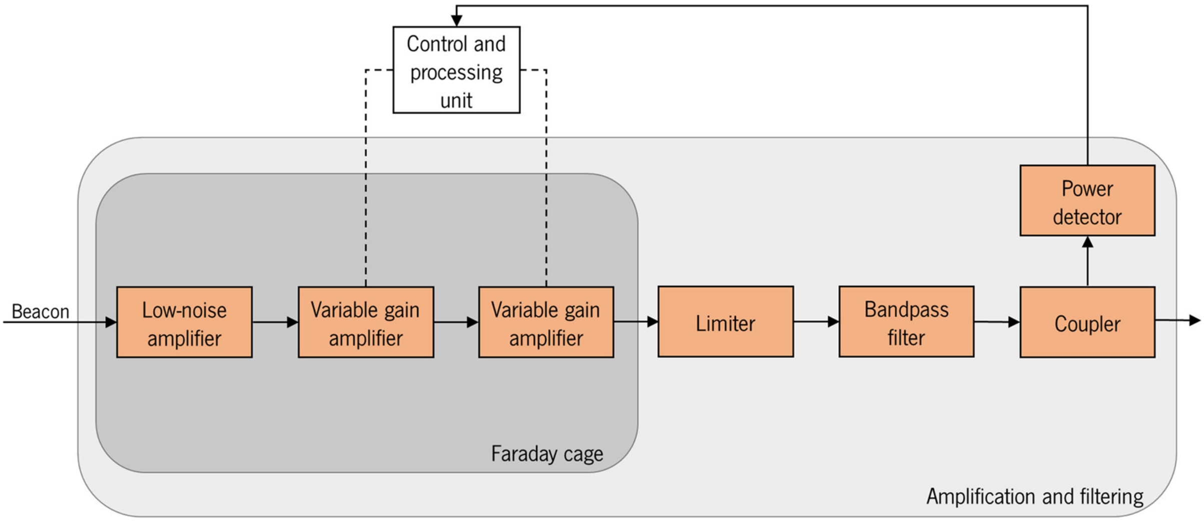

Figure 4.20 - Block diagram of the amplification and filtering stage.

4.2.6 Control and processing unit's flowchart

To control the WPT system, an Arduino MEGA was used. This device controls the states of the switches, the activation of the transmission and reception amplifiers, the amplification and filtering block of the reception, the phase shifters and reads and interprets the outputs of the phase detector. The device was coded so that it cycles between power transmission and beacon phase measurement to be able to periodically adjust its power focus on the implant's location. The flowchart of the software running on the Arduino is presented in Figure 4.21.

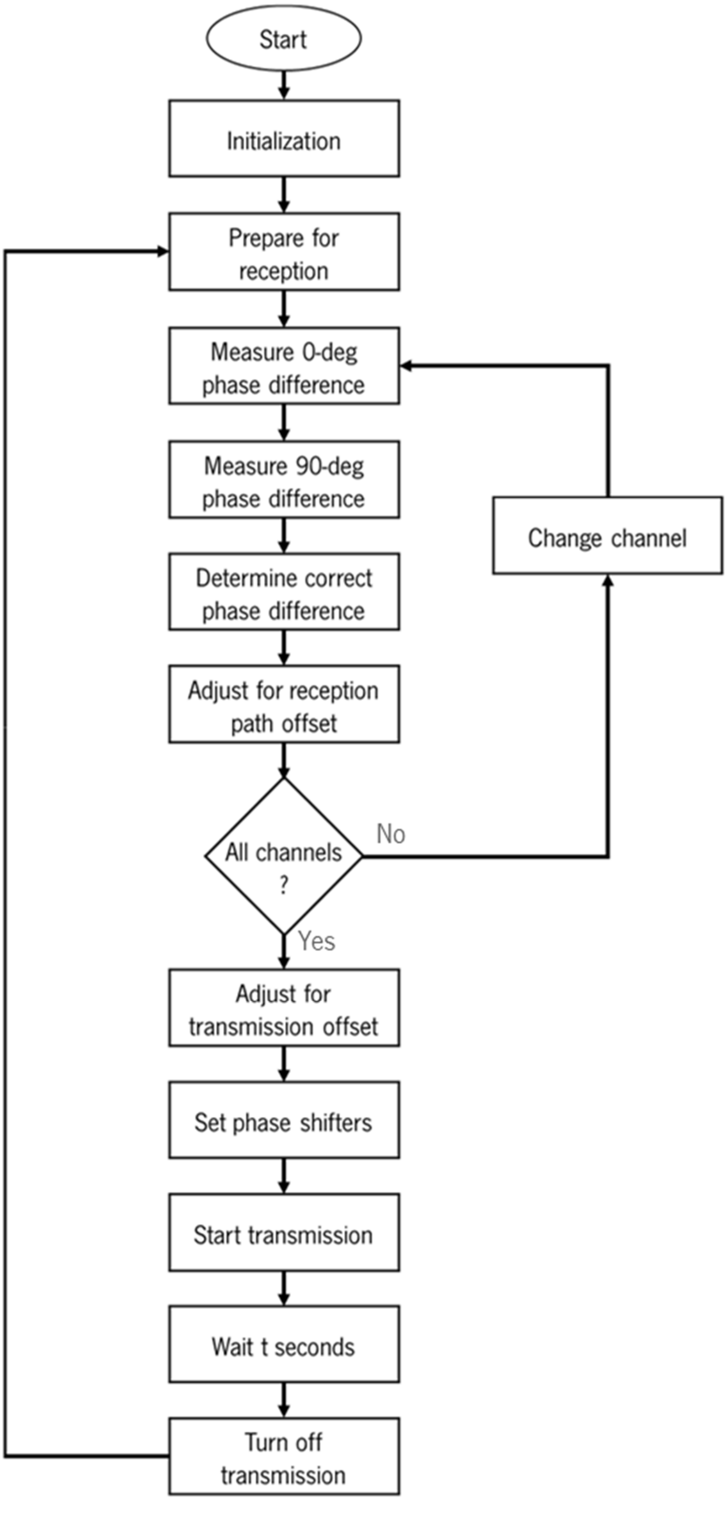

Figure 4.21 - Flowchart of the Arduino software for free-run operation of the WPT system.

The software starts by initializing the SPI which communicates with the phase shifters. Next, the output pins of the Arduino board which control the switches and amplifiers are configured. The main portion of the code then starts by preparing for the reception of the beacon: the power amplifiers and the VCO are turned off, the switches at the antennas are disconnected and the amplification and filtering block is turned on. Then, sequentially, every channel's antenna is connected to the reception block and its signal's phase is measured relatively to the reference channel. Sixteen measurements of the phase detector's output are averaged by the Arduino's ADC.

As it can be seen in Figure 4.22, which represents the phase detector's ideal response curve, each measured DC voltage can correspond to two different phase values. To overcome this, each channel's 90-degree shifted signal is also compared to the reference. The measured DC value at 0 degrees corresponds to two possible angles, while the 90-degree shifted value corresponds to another two, and the correct one needs to be determined. First, the 90 degrees that were added by the 90-degree splitter are subtracted from the two corresponding measured phase values. Then, the four values are compared, and two of them should be very similar. When that happens, it is determined that the phase difference between that channel and the reference is the average of those two similar angle values.

The calibration of the reception channel is then used to remove the effect of the path offset from the measured phase. After all channels are measured, the transmission path offset of each channel is compensated in the complementary phase difference and programmed into the corresponding channel's phase shifter. Finally, the VCO and power amplifiers are turned on for a period of time for power transmissions before the cycle repeats.

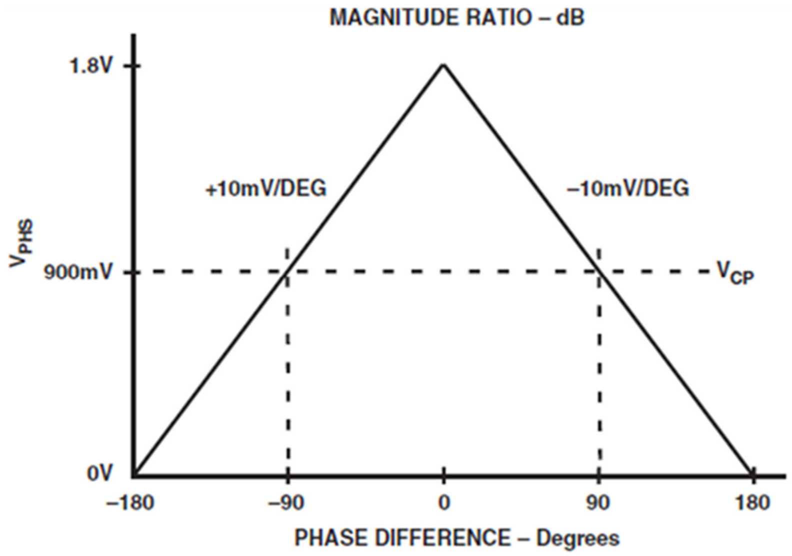

Figure 4.22 - Ideal response curve of the phase detector [7].

The tracking velocity of the WPT system is mostly dependent of the time it requires to measure the beacon's phase at its antennas. The system can perform this operation in 296 ms, after which it transmits power for a user-defined period of time which can be adjusted according to the application. Ultimately, the WPT system can track an implant at a rate of up to 3.4 Hz for extremely short power transmissions.

4.2.7 Prototype

The WPT system was assembled and placed inside a box to provide protection and ease of manipulation, transportation, and storage. The full system is presented in Figure 4.23, and close-up photographs of the different system components are presented in Figure 4.24 and Figure 4.25. Finally, the exterior of the WPT system and its interface with the antennas is presented in Figure 4.26.

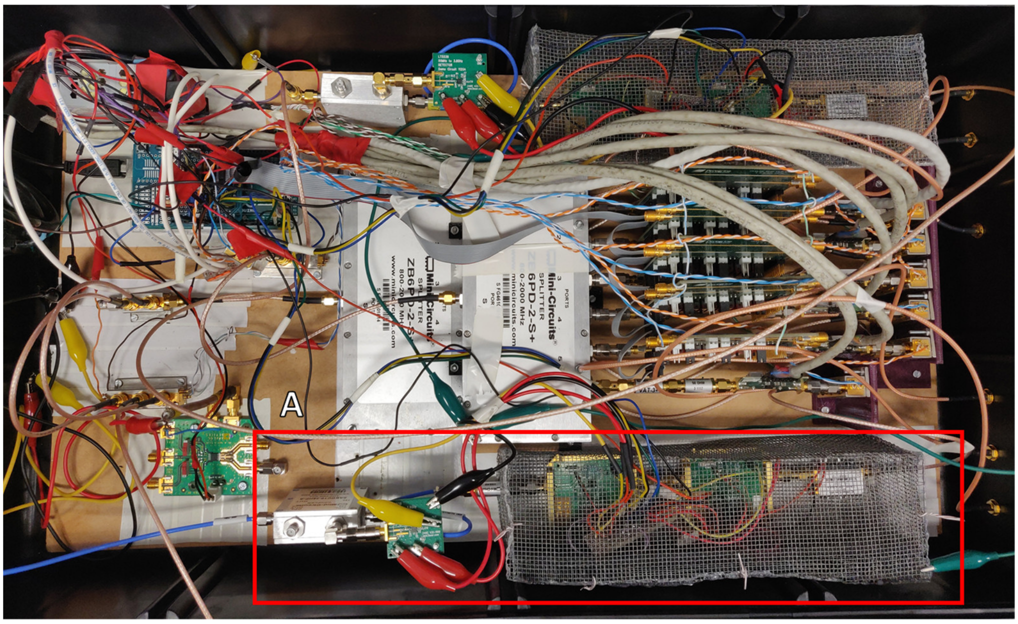

Figure 4.23 - Top-view of the full WPT system with the amplification and filtering block highlighted in A.

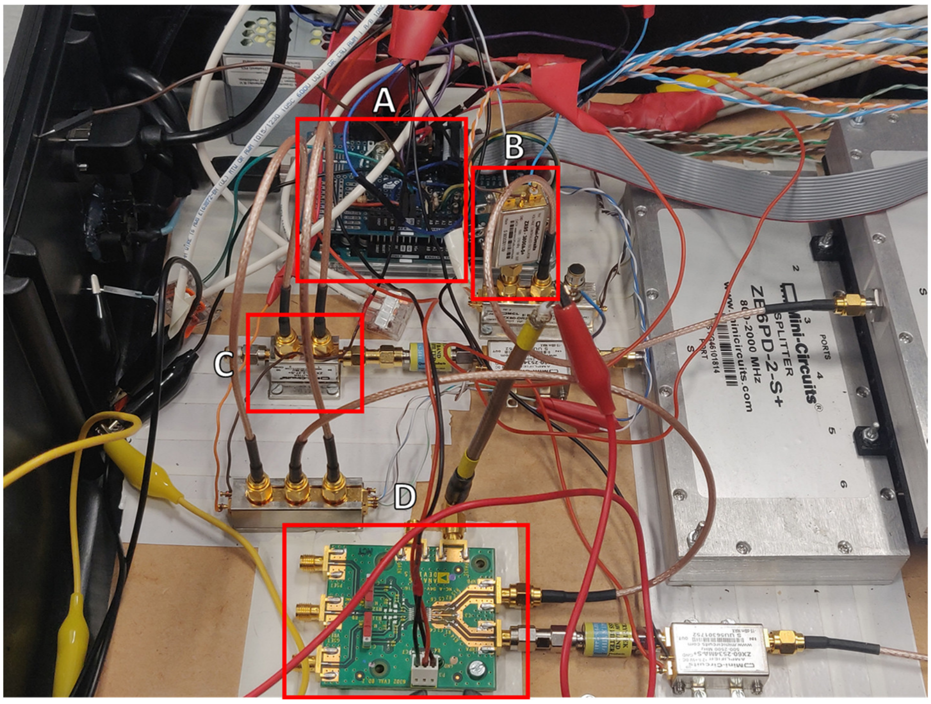

Figure 4.24 – A) Arduino MEGA that controls the WPT system. B) VCO for WPT transmission. C) 90-degree splitter for the phase detection system. D) Phase detector.

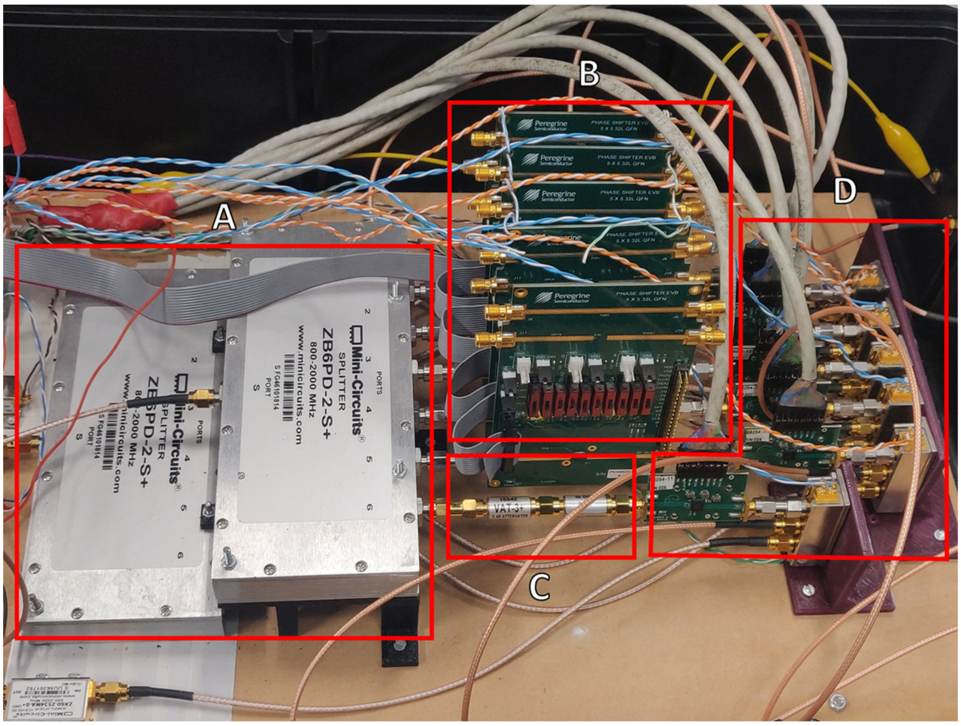

Figure 4.25 -A) 6-way splitter/combiners for the transmission (top) and reception (bottom) parts of the system. B) Phase-shifters, C) 6-dB attenuator and D) power amplifiers and RF switches that interface with the antennas.

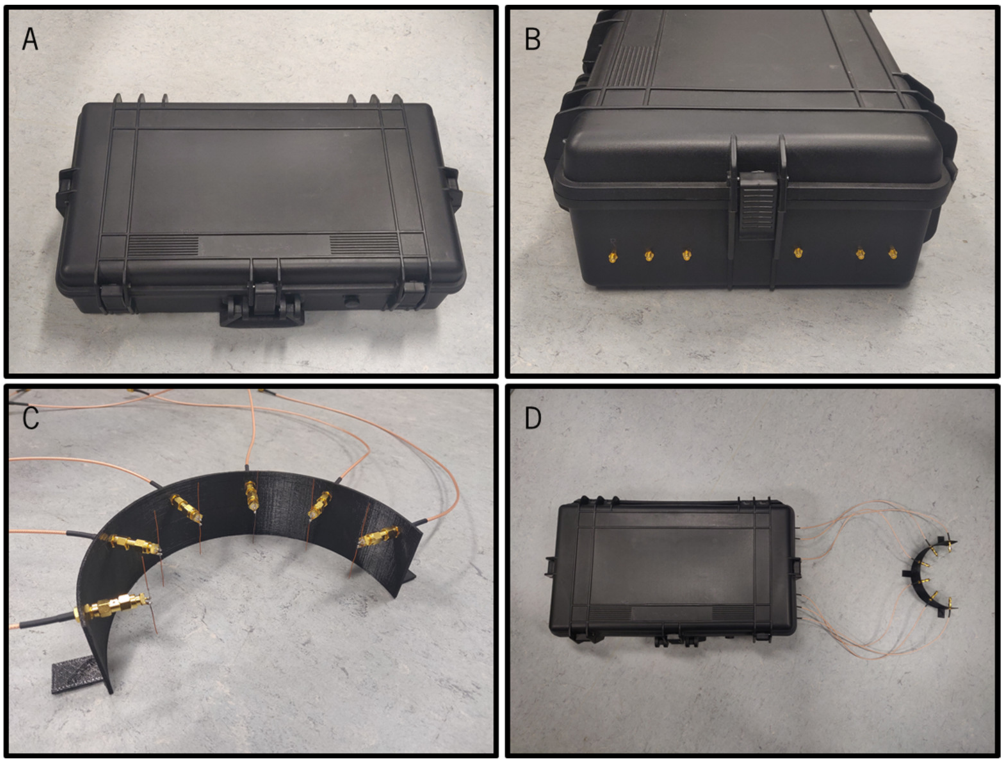

Figure 4.26 – A) Box that contains the WPT system. B) Connection for the external antennas. C) Example of a half-circle distribution of six dipole antennas. D) Full system ready for operation.

4.3 Closing remarks

In this chapter it was verified that the use of multiple power transmitters can yield significantly higher power levels inside biological mediums without increasing the maximum SAR level. This is possible because the multiple transmitters use different propagation paths in the medium to deliver power to the implant, thus making use of volume availability. Additionally, it was established that the use of tracking could increase the power levels even further by focusing power in the implant's location. With the objective of implementing this multimodal WPT, the system's requirements were identified, and it was proposed and developed accordingly.

The next chapter reports the findings obtained with the proposed WPT system, with a validation of its tracking capabilities and power delivery improvement over traditional single transmitter WPT systems.

4.4 References

[1] FCC, "OET bulletin 65: Evaluating compliance with FCC guidelines for human exposure to radiofrequency electromagnetic fields," vol. 65, 1997.

[2] P. Anacleto, "Self-Folding 3D Micro Antennas For Implantable Medical Devices," University of Minho, 2016.

[3] D. Nikolayev, M. Zhadobov, P. Karban, and R. Sauleau, "Electromagnetic Radiation Efficiency of Body-Implanted Devices," *Phys. Rev. Appl.*, vol. 9, no. 2, p. 24033, 2018.

[4] Z. Nie and Y. Yang, "A Model Independent Scheme of Adaptive Focusing for Wireless Powering to In-Body Shifting Medical Device," *IEEE Trans. Antennas Propag.*, vol. 66, no. 3, pp. 1497–1506, Mar. 2018.

[5] K. Zhang *et al.*, "Near-Field Wireless Power Transfer to Deep-Tissue Implants for Biomedical Applications," *IEEE Trans. Antennas Propag.*, vol. 68, no. 2, pp. 1098–1106, 2020.

[6] Crystek Microwave, "CBPFS-2441 Bluetooth SAW Band Pass Filter." 2016.

[7] Analog Devices, "AD8302 LF–2.7 GHz RF/IF Gain and Phase Detector."

CHAPTER 5 WPT SYSTEM PERFORMANCE ASSESSMENT

A multimodal approach to WPT for implantable devices has been proposed. It demonstrated enormous potential for changing the way energy is transferred to implantable devices and, consequently, allow for ever-smaller electronic devices to be powered inside the human body. As such, an experimental WPT system was designed for performance assessment, and the results are presented in this chapter, starting with a power distribution mapping inside a liquid phantom and then moving on to geometrically-accurate human body models and use cases with a wireless 'implant'.

5.1 Power distribution inside a liquid head phantom

The WPT system's operation was tested and its working principle validated resorting to the experimental setup presented in Figure 5.1. An antenna was placed inside a cylindrical container with a radius of 55 mm, containing human head phantom with a permittivity of 39.2 and a conductivity of 1.8 S/m. It was connected through an RF switch (Mini-Circuits ZFSWA2R-63DR+) to the VNA for received power measurement, and to a RF signal generator (Agilent N9310A) to transmit the beacon (cf. with 4.2.2) to the WPT system. The output power of each antenna of the WPT system was measured at 13.3 dBm. Two step motors were used to move the antenna in the horizontal plane inside the phantom. All hardware was controlled by a Labview program, which also synchronized the reception/transmission cycles with the WPT system. Six antennas (Antenova Amoris SRF2W021) were placed 15 mm away from the phantom, equally spaced between themselves in one hemisphere of the container.

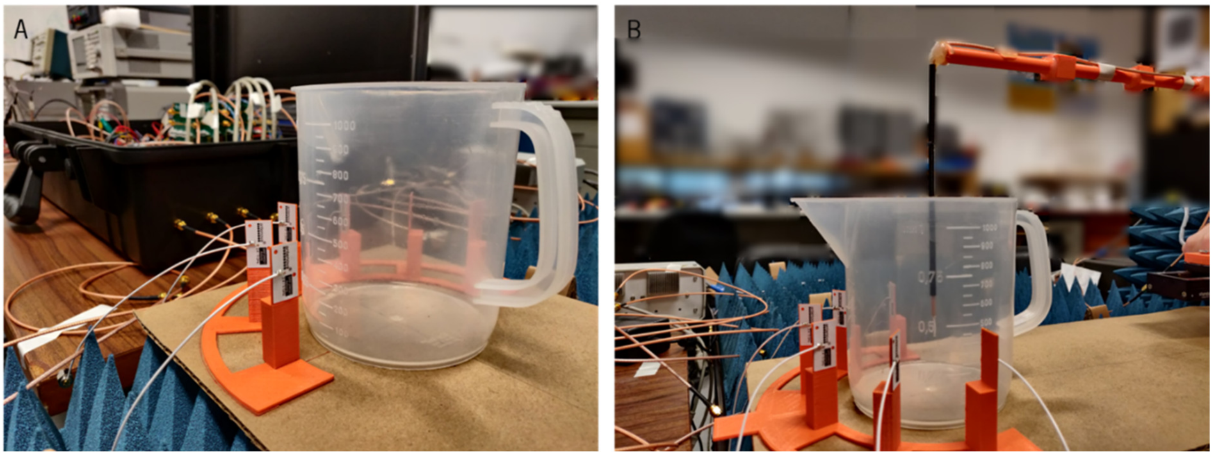

Figure 5.1 – Experimental setup for power mapping inside a liquid phantom demonstrating the positioning of the phantom holder (A) and the antenna inside of it (B).

The experimental setup was replicated in HFSS (Figure 5.2). Resorting to a script implemented in Python, HFSS swept a plane inside the phantom (akin to the experimental setup) and calculated, for each point, the average Poynting vector's magnitude in an area of 4 mm^2 around the "implanted" antenna, and the maximum SAR_{10g} of the whole phantom. The script then adjusted the transmission power of the antennas so that the SAR_{10g} in the phantom was 10 W/kg. Both the simulation and the measurements considered the following three scenarios: 1 - a single antenna transmitting power; 2 - six antennas transmitting in-phase signals (no tracking); and 3 - six antennas transmitting signals with the phases determined by reading the beacon (with tracking). The simulation was performed in ANSYS HFSS (Windows 10 64-bit Professional, Dual Intel Xeon Gold 6246, 512 GB DDR4 2666 MHz RAM).

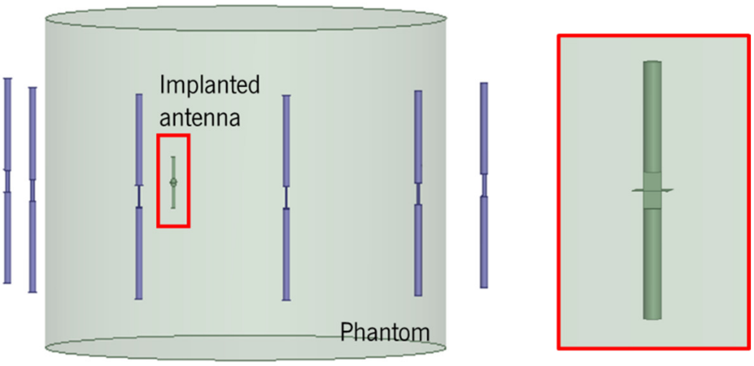

Figure 5.2 - HFSS model of the head phantom surrounded by the WPT system antennas. Highlighted in red is the "implanted" antenna responsible for transmitting the beacon and around which the Poynting vector's magnitude is calculated.

Using the experimental and the simulation setups, it was possible to observe the effectiveness of the proposed WPT system in two different scenarios. In the simulation, the transmission power of the antennas is adjusted so that the maximum SAR_{10g} in the phantom is 10 W/kg. Consequently, it is possible to see the power levels' improvement inside the phantom when aiming to maximize the power delivery to the 'implant', *i.e.,* operating at the edge of the safety limit. In the experimental setup, the power transmitted by each antenna is constant and, therefore, the SAR can vary as a consequence of the combination of the six transmitted signals. For an output power of 13.3 dBm per antenna, a SAR_{10g} of 0.38 W/kg is expected when all the antennas transmit in-phase signals. Hence, the experimental results show how much power increase can be achieved when the SAR value is not a limiting factor (either when the WPT system is transmitting low power levels, or when the SAR is dismissed).

5.1.1 Single transmitter versus multitransmitter

Traditional WPT schemes, as previously stated, are composed mainly of a single transmission antenna. The first proposed method to increase the power delivered to an implant presented in this work was the use of multiple transmitter antennas. Therefore, the comparison between the power delivered to an implant in these scenarios is presented. Figure 5.3 contains the simulated results, while Figure 5.4 contains the ones obtained experimentally. Both images show the power distribution for a single antenna (A), six antennas (B) and the difference between them (C).

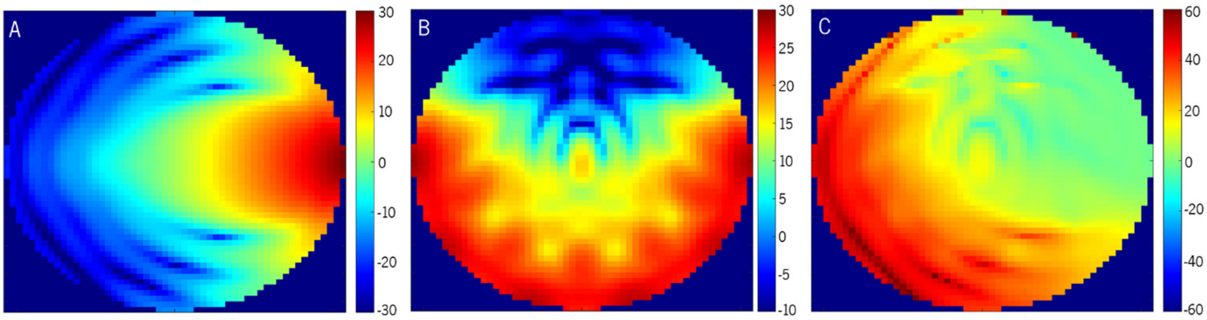

Figure 5.3 - Simulated Poynting vector magnitude (W/m^2), assessing the power that can be delivered to an antenna inside the phantom by one transmitter (A) and by six transmitters (B). The output power of the transmitting antennas is individually adjusted so that the maximum SAR_{10g} in the phantom is always 10 W/kg. The results are presented on a logarithmic scale, and the difference between B and A is presented in C.

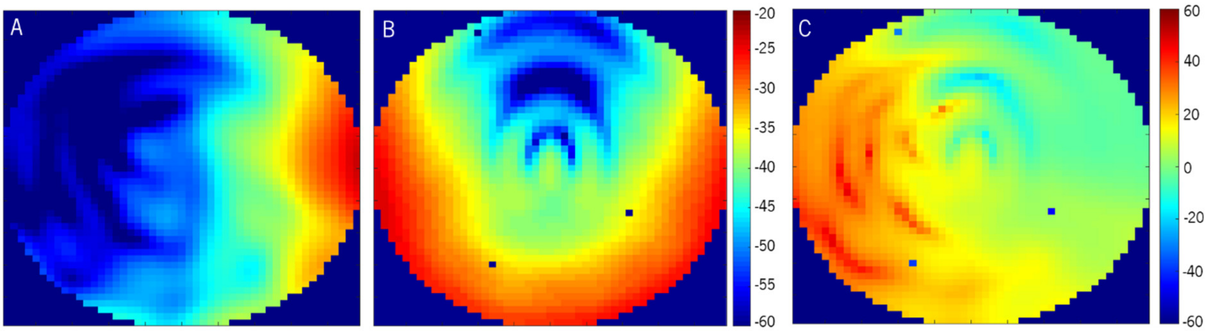

Figure 5.4 - Measured power received by the antenna inside the phantom with one (A) and with six (B) transmitting antennas. The results are presented in dB relatively to a 6 dBm output by the VNA. The difference between B and A is shown in C.

From the previous figures, it is immediately possible to conclude that a good agreement between numerical and experimental results was achieved in terms of power distribution inside the phantom, for both scenarios. The power distribution obtained by a single antenna is highly localized closest to the antenna, as predicted in Chapter 4. In contrast, with the six antennas, the power distribution is much more even across the studied plane. As such, there is a significant difference between the two power distributions. In areas very close to the transmitting antenna that is common in both scenarios, the achieved power was similar, as even in the six-antenna scenario, the influence of the antenna closest to the area is stronger than the other antennas' influence. As the implant moves away from that region, the differences in power increase drastically, achieving differences of over 60 dB in the areas most distant from the single antenna transmitter. Of course, in locations furthest from the single antenna the argument can be made that the antenna may be moved to a more suitable location. However, that may not be possible in some scenarios. Still, power gains of an order of magnitude were registered close to the single antenna when multiple transmitters were employed.

It is noteworthy that there are areas closest to the top of the measurement plane where the single antenna performs better than the multitransmitter scenario. This happens because with multitransmitters a destructive combination of the signals can occur in the described areas, as seen in Figure 5.3 B and Figure 5.4 B. With the single antenna, destructive combination in those locations does not occur and, consequently, the power availability in these small areas is higher. This effect can also be observed in the area just below the antenna that acts as the single transmitter. Here, the power decreased 3 dB when multiple transmitters were used due to a destructive combination between the signals being transmitted.

Ideally, the six transmission antennas are transmitting the same power levels and are equally distanced from the geometrical centre of the phantom. Therefore, equation 3.35 can be applied. As six antennas are used, a power increase of 15.6 dB was expected. In the simulation, a gain of 14.9 dB was verified, which is in agreement with the predicted value, especially when considering that the simulation script may reduce the transmitted power in the six antenna scenario to keep the SAR_{10g} at 10 W/kg, thus accounting for the marginally smaller gain. With this feature turned off, the gain was of 15.1 dB. In the measurements, the gain in the centre position was 12.3 dB, which is lower than expected. However, it is a consequence of the slightly different power levels being transmitted by each of the six antennas and small misalignments in the measurement setup.

Finally, it is interesting to note that the lensing effect due to the phantom's circular shape is evident in both the simulated results (Figure 5.3 A) and in the measurements, albeit less clearly in the latter (Figure 5.4 A).

5.1.2 Multitransmitter with and without tracking

This work showed that the use of multiple transmission antennas increases power availability for an implant inside its medium. However, controlling an additional WPT link parameter, the phase of the transmitted signals, the improvement over the traditional single-antenna approach is even more significant. To validate this claim, the power distribution was measured and simulated with the proposed WPT system, while tracking the implant position. The results were then compared with the six antennas setup without tracking (transmitting in-phase signals). Figure 5.5 and Figure 5.6 have, respectively, the simulated and the experimental results. Again, it is immediately possible to observe a good agreement between numerical and experimental results in terms of power distribution inside the phantom for both scenarios: without tracking (Figure 5.5 A and Figure 5.6 A) and with tracking (Figure 5.5 B and Figure 5.6 B).

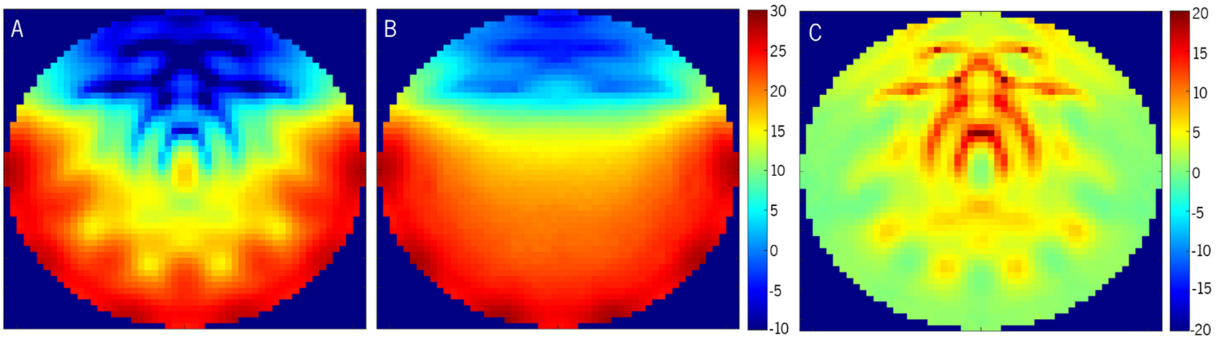

Figure 5.5 - Simulated Poynting vector magnitude (W/m^2) that can be delivered to an antenna inside the phantom with no tracking algorithm applied (A) and with tracking (B). The output power of the transmitting antennas is individually adjusted so that the maximum SAR_{10g} in the phantom is always 10 W/kg. The results are presented on a logarithmic scale, and the difference between B and A is presented in C.

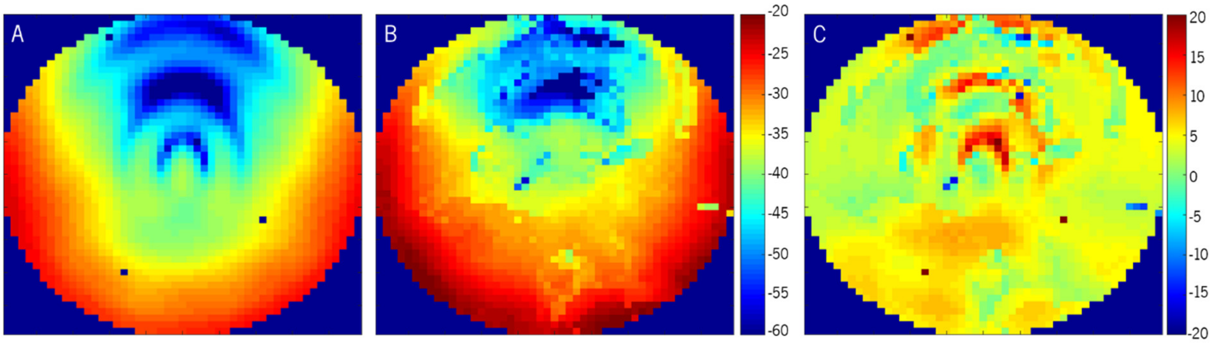

Figure 5.6 - Measured power received by the 'implanted' antenna inside the phantom with no tracking algorithm applied (A) and with tracking (B), where the results are presented in dB relatively to a 6 dBm output by the VNA. The difference between B and A is presented in C.

With tracking, the power availability increased all over the measurement plane, as seen in Figure 5.5 C and Figure 5.6 C. Power increases ranging from around 0.5 dB to 5 dB, were verified in areas where power availability was already high in the in-phase scenario, with the most predominant power gain being between 3 and 10 dB, as shown by Figure 5.6 C, with gains of up to 24 dB being registered.

Using the system's tracking capabilities in the simulation increased the power on the top of the measurement plane, the furthest away from the transmitting antennas, while in the measurements that was not possible. This is caused by the distance between the implant and the antennas, especially the reference antenna, which is far too large and the WPT system may not, accurately, measure the required tracking phases. When that happens, it reverts to transmitting an in-phase signal, and the power is the same in those regions, with and without tracking. This is visible in Figure 5.6 C, as 0 dB of power increase were registered in the cold spots. The same effect can be noted in the phantom's geometrical centre, albeit for a different reason. By definition, this spot is equidistant from all the antennas, and since the propagation medium is homogenous, the tracking algorithm determines that the signals must be transmitted in-phase for them to combine in the geometrical centre. The power available in the centre, with and without tracking, is the same, thus validating the system.

Finally, it is noteworthy to comment on the power that could be delivered to the 'implanted' antenna. According to the measurement of Figure 5.6 B (multitransmitter with tracking), the maximum power of -19.7 dB relative to a 6 dBm source, which translates to -13.7 dBm, was delivered at an 'implant' depth of 5.3 mm. The power output of each transmission antenna was 13.3 dBm, which led to a simulated SAR_{10g} of 0.52 W/kg. If the power output was adjusted so that the SAR_{10g} was 10 W/kg, the antenna output power would be 26.1 dBm. Thus, the power delivered to the implant in such conditions would be -0.9 dBm.

The presented results confirm that the addition of tracking leads to a better power distribution in an implant's medium, comparatively to the use of the multitransmitters alone. By association, the use of multitransmitters and phase manipulation achieves results vastly superior to the traditional singe-antenna WPT solution, as will be discussed below.

5.1.3 Overall improvement over single transmitter system

Previous sections demonstrated that the use of multiple transmitters improves the power delivered to an implantable device without increasing the SAR in the tissue. Furthermore, with tracking, additional power can be provided under the same circumstances. As such, this section demonstrates the overall improvement that the use of multiple transmitters, with phase control, can achieve over the traditional, one transmitter, WPT link. Figure 5.7 presents simulated (A) and measured (B) differences in power distribution between the scenarios mentioned above.

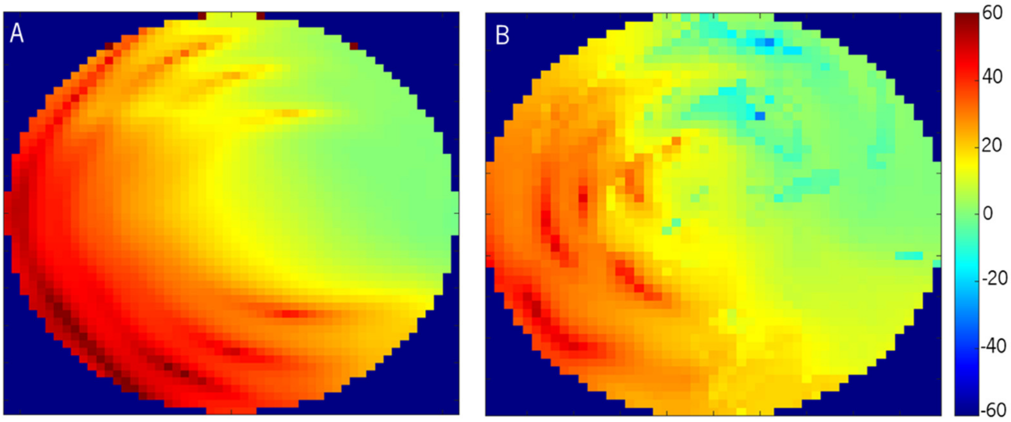

Figure 5.7 – Simulated (A) and measured (B) power distribution difference between a multitransmitter WPT system with tracking and a traditional, single transmitter system (scale in dB).

As in the previous sections, a good agreement was obtained between the numerical and the experimental results. The proposed system is ultimately capable of increasing the power delivered to an implant by over 20 dB (and up to nearly 60 dB) in a large portion of the measurement plane. As expected, the lowest power increase, around 1 dB, occurs near the location of the single transmitter. Experimental results show that there are areas where the power loss is more noticeable than in the simulation. This can be due to limitations of the WPT system in terms of the minimum beacon power required for accurate phase measurements and, consequently, for precise positioning of power at each spot. When this happens, the power signals are transmitted in-phase and destructive combinations can occur, leading to less power than in the one-antenna scenario, as previously discussed.

5.1.4 High-gain antennas

Having achieved the exciting results presented above, it became interesting to observe the effect that different antennas, namely highly-directive ones, would have on the power delivery capabilities of the WPT system. As such, six Yagi-Uda antennas (Figure 5.8) with a gain of 12.9 dB were fabricated, and both the experimental setup and the HFSS model were updated, as shown in Figure 5.9.

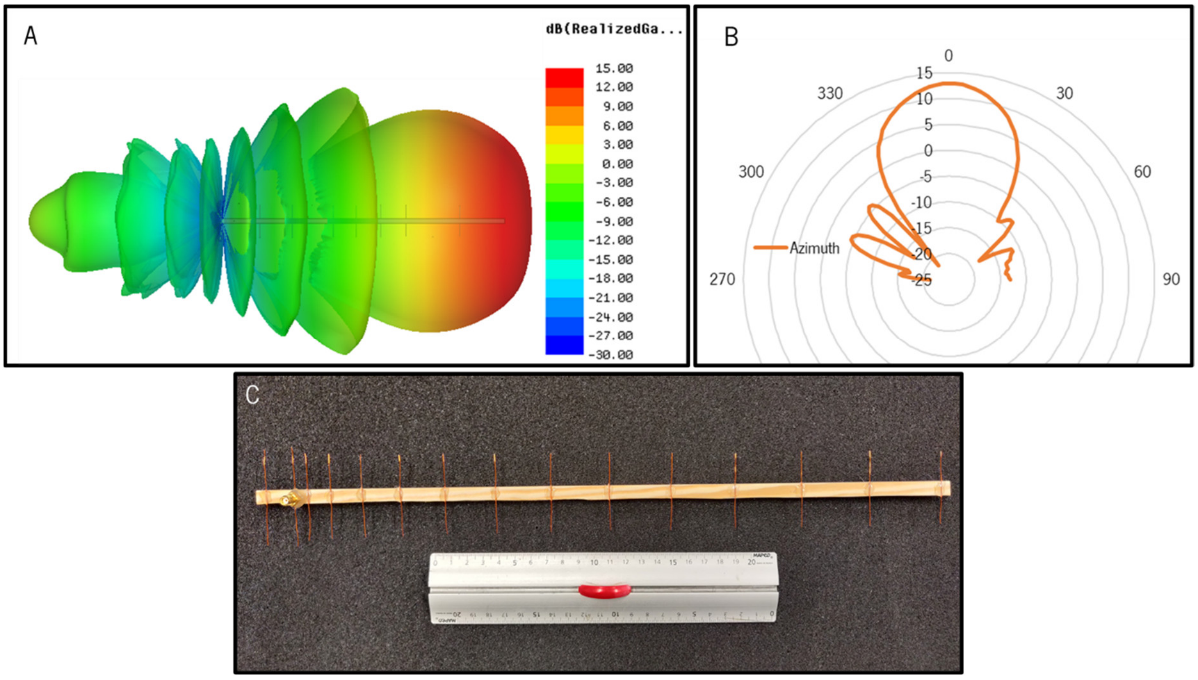

Figure 5.8 – Simulated (A) and measured (B) radiation pattern of the Yagi-Uda antenna (C) at 2.45 GHz.

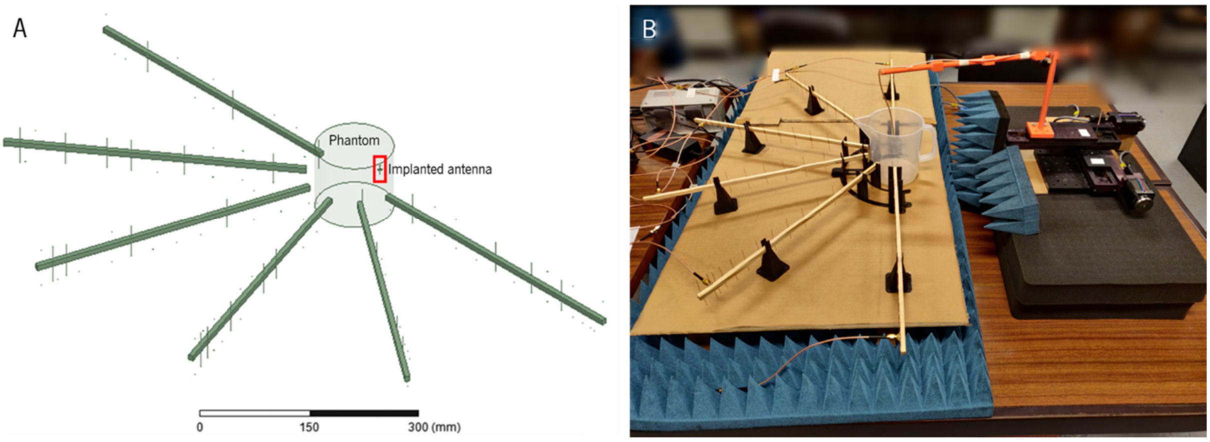

Figure 5.9 - HFSS model of the six Yagi-Uda antennas distributed around the phantom (A), and the corresponding experimental setup (B).

The geometrical complexity and the high volume of the HFSS model required around 300 GB of memory to simulate each point inside the phantom using in the same machine as the previous simulations. Hence, given the 512 GB limit, parallelization was not possible, and the simulation of each point required several hours to be completed. To achieve the same resolution as Figure 5.3 and Figure 5.5, which have 2244 points per plot, several months of continuous simulation would be necessary. Therefore, the number of simulated points had to be significantly reduced, compared to the simulations of previous setups. Figure 5.10 A and B contain, respectively, the Poynting vector magnitude when six

Yagi antennas are used without and with tracking. As usual, Figure 5.10 C presents the difference between B and A. Figure 5.11 presents the same setup, but with experimental values.

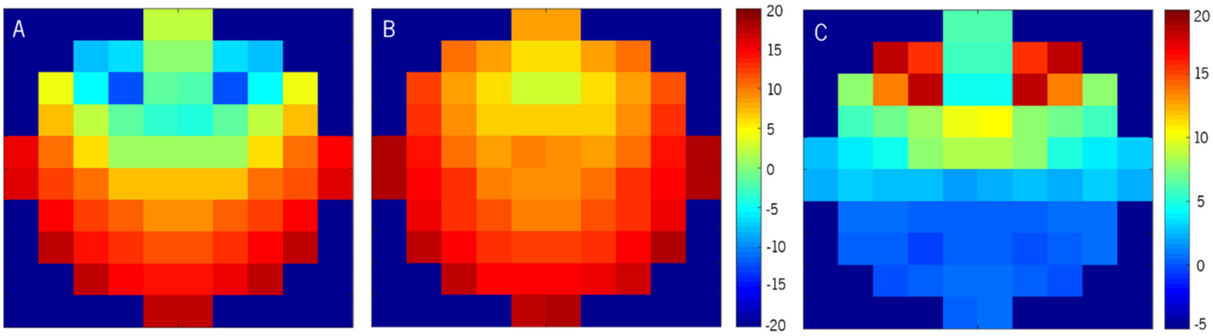

Figure 5.10 - Simulated Poynting vector magnitude (W/m²) that can be delivered to an antenna inside the phantom with no tracking algorithm applied (A) and with tracking (B). The output power of the transmitting Yagi-Uda antennas is individually adjusted so that the maximum SAR_{10g} in the phantom is always 10 W/kg. The results are presented on a logarithmic scale, and the difference between B and A is presented in C.

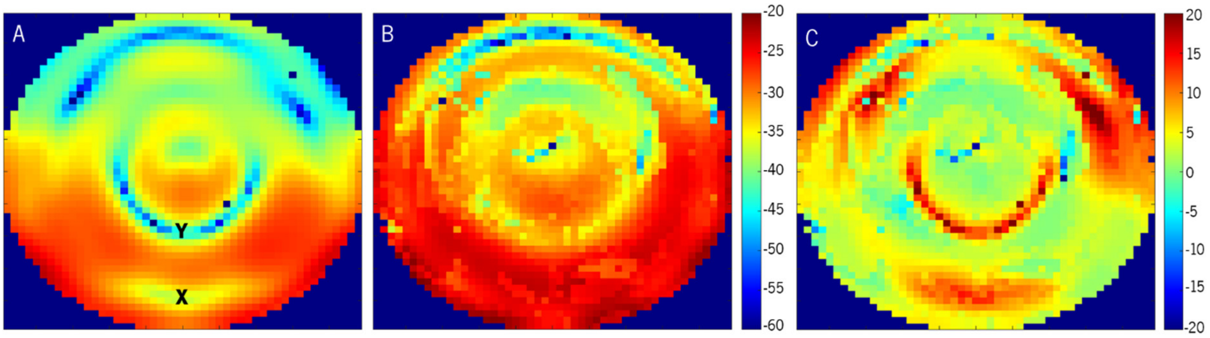

Figure 5.11 - Measured power received by the 'implanted' antenna inside the phantom with no tracking algorithm applied (A) and with tracking (B) with the Yagi-Uda antenna setup. The results are presented in dB relatively to a 6 dBm output by the VNA. The difference between B and A is presented in C.

Implementing highly directive antennas did not compromise the overall operation of the WPT system, because tracking still significantly increases power levels in the phantom. With the Yagi-Uda antennas, the maximum power level delivered to the 'implanted' antenna was -18.9 dB, relative to the 6 dBm source, which corresponds to -12.9 dBm. This value is higher than the one achieved by the dipole antennas (-13.7 dBm), albeit not as much as initially expected, given antennas' gain difference. However, this could be due to the fact that high directivity antennas make it harder for transmitted signals to recombine than signals emitted by the omnidirectional dipoles, which ideally propagate equally in all directions of the azimuth plane. As such, this antenna array doesn't make use of the full potential of the WPT system's tracking capabilities. Nevertheless, it was still possible to achieve power increases in all the measurement using tracking. The antennas' high gain can be exploited to increase their distance to the phantom. Given their narrow beam, no overlapping is expected between propagation paths inside the biological medium when the antennas are located further away from the medium. Additionally, increasing the number of antennas may also benefit the system's performance.

Interestingly, when no phase control is employed (Figure 5.11 A), some cold areas appear where they are not expected, namely in the southern hemisphere of the measurement plane, and in the shape of a ring around the geometrical centre (marked with the letters X and Y in Figure 5.11 A). A possible explanation for this phenomenon is related to the nature of Yagi-Uda antennas. These antennas are composed of a radiating element and several parasitic structures that re-radiate the signal from the radiating element so that all the signals combined result in a highly directional beam. Therefore, when the 'implanted' antenna is placed at specific distances from the Yagi antenna, it can act as another parasitic element, coupling with the antenna, leading to unexpected results. Inside the phantom, the wavelength of a 2.45 GHz signal is 19.6 mm, and the distance between X and Y is around 20 mm, which corroborates the conclusion drawn from the results. Suppose the 'implant' is at such a distance from the Yagi-Uda antenna where it acts as a parasitic element that generates a signal in phase opposition to the one it receives. In that case, the first attenuates the second, leading to a lower power reading in that location. A full wavelength away from that distance the same effect would occur, as verified. However, this effect could not be replicated in HFSS. Finally, it is important to note that the use of tracking mitigated this effect, albeit not perfectly in region Y.

From these results, it is possible to conclude that the antenna array used with the WPT system bears influence in the results that can be achieved. The antennas' directivity, their number, and the distance they are located from the medium are parameters that must be optimized according to the application. Therefore, sufficient study and care must be given to this critical element of the system to maximize power gains and prevent cold spots.

The next step is the validation of the system's tracking capabilities. Also, we will assess the power delivery improvement over traditional methods in a more geometrically accurate model of the human body, using a wireless 'implantable device' as a receiver.

5.2 Design of the implant

The goal of the system is to locate and power an implantable device inside a black-box medium. Therefore, to make the tests as reliable and close to a real scenario as possible, fully-wireless and independent operation of the implant-mimicking device is required. The first step towards this was establishing the requirements for the device which will simulate the implantable device, now referred to as implant.

In a real scenario, an implant should be capable of transmitting a beacon to the WPT system, and then receive power to perform the tasks it was designed for. In this case, since measuring the power received inside a phantom is the required goal, an RF power detector needs to be included in the implant, along with a RF generator and antenna to transmit the beacon. Furthermore, it should be able to communicate back the outside the power value it is receiving, therefore a communication module is also required.

Considering the identified requirements for the implant, and bearing in mind compatibility with the WPT system, a small microcontroller with integrated ADC and radio to transmit the data wirelessly is highly desirable to keep the implant as small as possible. The Insight SiP's ISP1507 was selected as the implant's brain. This device is based on a Nordic Semiconductor nRF52 Bluetooth 5-ready microcontroller, packaged with an antenna operating at 2.45 GHz, all within an 8x8x1 mm^3 package. Given that this microcontroller can be programmed to transmit the beacon through an unmodulated carrier, and can also wirelessly transmit data, the only external components required are a power detector, a battery and a voltage regulator. The power detector is a Linear Technologies LT5534, which has a maximum operating frequency of 3 GHz and a linear voltage output as a function of input RF power from -55 dBm to -10 dBm, approximately, at 2.45 GHz. The battery is a Powerstream GM301014H-PCB, which has a nominal voltage of 3.7 V, a capacity of 14 mAh and a maximum discharge current of 140 mA. The whole system is powered with 3.3 V, so Texas Intruments' TLV702-Q1 voltage regulator is also required. Finally, a custom PCB was designed. With this solution, a small device that fulfils all the requirements was produced. Figure 5.12 shows the proposed implant.

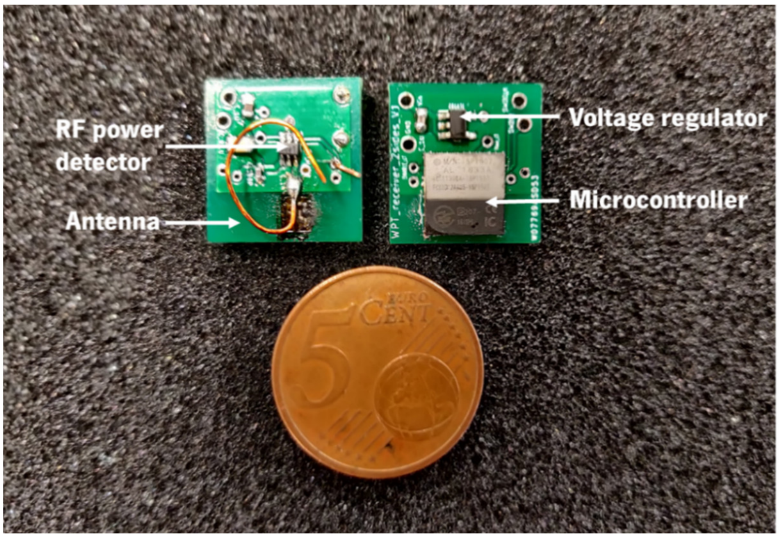

Figure 5.12 – Photograph of the implant ready for use.

5.3 Experimental setup

To further validate the WPT system, it is important to test it in a realistic scenario, for which two crucial elements are required: a wireless ‘implantable’ device, and an implantation medium. This section will report on the development of an experimental setup that will allow the measurement of the power that can be delivered to the implant in several locations inside geometrically accurate human body models.

5.3.1 Integration of the WPT system with the implant

To integrate the wireless implant and the WPT system and allow for automatic operation, a setup had to be devised to automate and synchronize the setup’s components. A PC running Matlab was responsible for synchronizing the WPT system and the implant, as power transmission/power detection and phase reading/beacon transmission had to be timed between these devices. Furthermore, the PC is where the power values received and measured by the implant are stored. For this to happen, the PC also requires a data receiver. For this purpose, the ISP1507-AX-DK development kit ISP130603E board was used. In summary, four different devices were necessary: the WPT system (controlled by an Arduino board), the implant (nRF52 microcontroller), the data receiver (nrF52 microcontroller) and the PC (Matlab). The flowcharts of the software developed for the devices are shown in Figure 5.13, and Figure 5.14 presents a temporal diagram of the interaction between the four devices.

The operation of the implant is as follows. After initialization, the microcontroller deactivates the power detector and sends the beacon signal during a predefined amount of time, at 2.45 GHz. Then, it deactivates its radio to protect it, and enables the power detector. It reads the power delivered to the implant and translates it into a DC voltage that is periodically sampled by the microcontroller’s ADC and stored. After power transmission ends, the microcontroller sends the stored values and a ‘SYNC’ command to the outside and the cycle repeats. The implant’s microcontroller executes this program in a loop, and the devices on the outside synchronize with the implant through the ‘SYNC’.

The receiver is constantly waiting for wireless data sent by the implant, and when it receives that data, it directs it via a Serial port to the PC. When it detects the ‘SYNC’, it changes a pin state to ‘1’, which triggers the Arduino in the WPT system, while the PC simply reads and saves the data sent via Serial port by the reader.

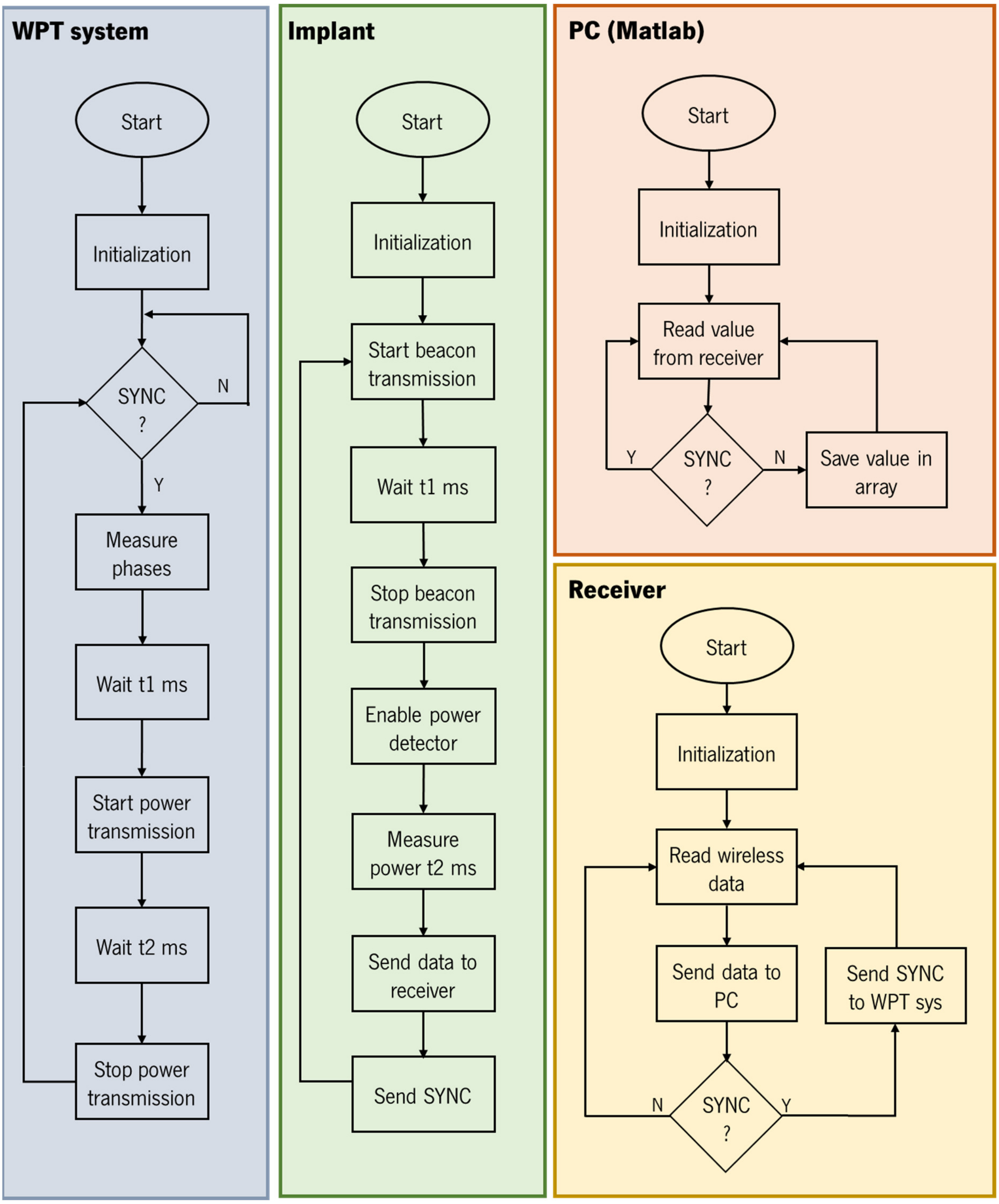

Figure 5.13 - Flowcharts of the whole system for WPT to a wireless implant.

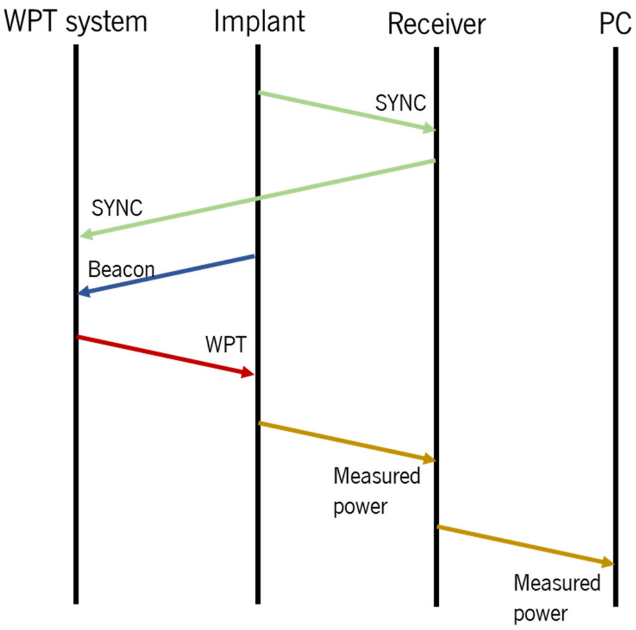

Figure 5.14 -Temporal diagram representing the operation of the four devices.

The WPT system will start and wait until it receives the 'SYNC' signal for synchronization with the implant through an interruption that triggers when a given pin level rises. When that happens, it reads the implant's beacon and waits t1 milliseconds, the time during which the implant will transmit the beacon. After that time, the WPT system transmits power with the adjusted phase during t2 ms. The WPT system then stops sending power and goes back to waiting for another synchronization signal. During that time, the implant wirelessly sends the stored data to the receiver, followed by the 'SYNC' signal, and the cycle begins all over again. The decimal value '255' was chosen as the 'SYNC' signal because the DC output of the power detector is, at most, 2.4 V, while the ADC is powered with 3.3 V, therefore the end of scale of the ADC will never be reached during normal operation.

5.3.2 Human body models

The human body models must fit three requirements to perform the desired measurements: be geometrically accurate, allow the use of a phantom, and have a path for the implant to travel inside. With this in mind, a plastic torso, leg, and skull were adapted for the proposed experiments. The models were fitted with a thin plastic tube inside and properly insulated to become watertight. Due to their large volumes, the leg and the torso were filled with water, which acts as a good initial approximation to biological tissue's dielectric properties. The skull was filled with a human head phantom with a permittivity of 39.2 and a conductivity of 1.8 S/m. Photographs of the models are presented in Figure 5.15 and Figure 5.16, in which are marked the points where the measurements were performed.

Figure 5.15 -Anatomical models of a human torso (A1 and A2) and lower leg (B) adapted to be filled with phantom, along with the pipe for the implant to travel in. The points where measurements were performed are marked in the photographs.

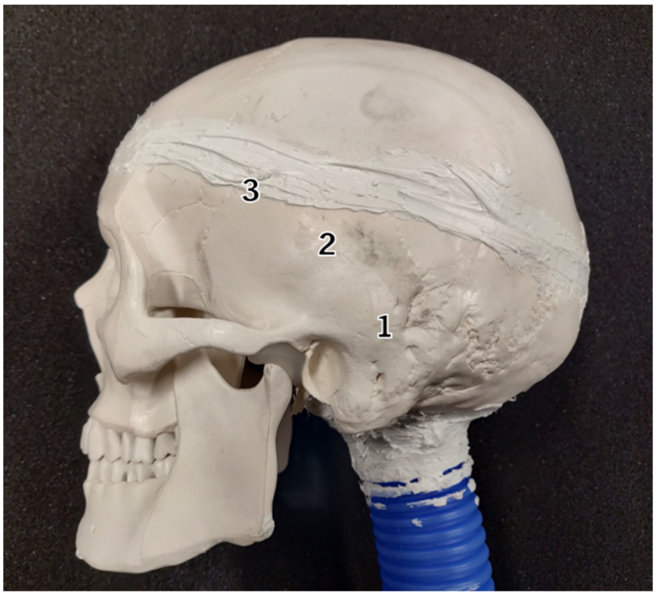

Figure 5.16 – Anatomical model of a human skull adapted to be filled with phantom, along with the pipe for the implant to travel in. The points where measurements were performed are marked in the photograph.

5.4 Power transfer to the wireless implant

The wireless implant was placed inside the tubing of the models and moved along its path. In the previously specified locations, the implant would stop and the power it received was measured for three transmitter scenarios: single antenna, six antennas and six antennas with tracking. The experimental setups are presented in Figure 5.17. Due to the shape of the torso model, a different and flatter antenna mount was developed (Figure 5.17 B).

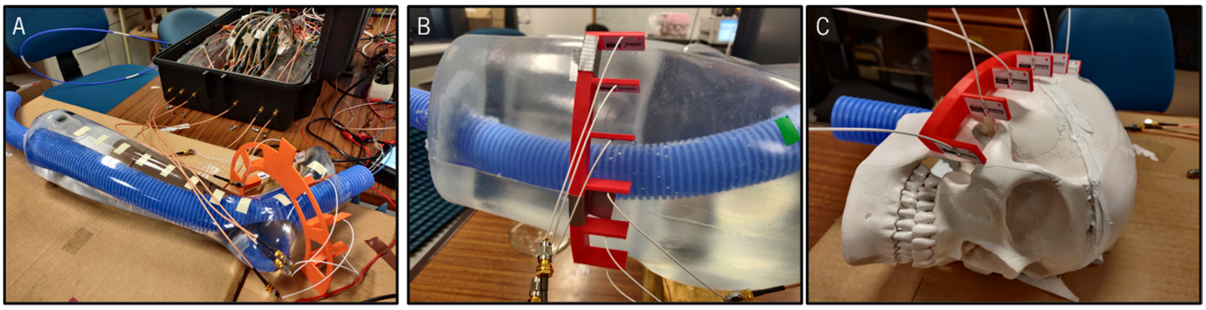

Figure 5.17 - Experimental setup to transfer power to the wireless implant in the lower leg (A), torso (B) and skull (C) models.

The experimental results obtained in the lower leg and the torso models are presented in Figure 5.18. The absolute power reading of the implant in each location is shown in graphics A and C. Figure 5.18 B and D present the power increase achieved using multitransmitters with and without tracking comparatively to the traditional single-antenna transmitter.

From the results, it is possible to verify that the use of multitransmitters and tracking results in significantly higher power levels being delivered to the implant. In the leg and torso models, power increased between 4 and 18 dB relative to the traditional WPT link, demonstrating the advantages of the proposed WPT system. In terms of absolute power, the proposed system delivered between -12 dBm and –25 dBm to the implant. Two factors can explain this variability. First, the implantation depth and geometry of the model vary from point to point and, finally, the alignment between the implant’s antenna and the WPT system’s antenna array varies between each point, therefore it is also not possible to compare power levels between points. The results obtained in the skull, presented in Figure 5.19, confirm these findings. There was less variation among points of the skull because the shape of the medium and the distance between the antennas and the receiver did not change significantly amongst them, in opposition to the leg and torso models. Additionally, the use of tracking didn’t result in power gains as high as in the torso and leg models. This may be due to the shape of the antenna array, which can be optimized for the human head.

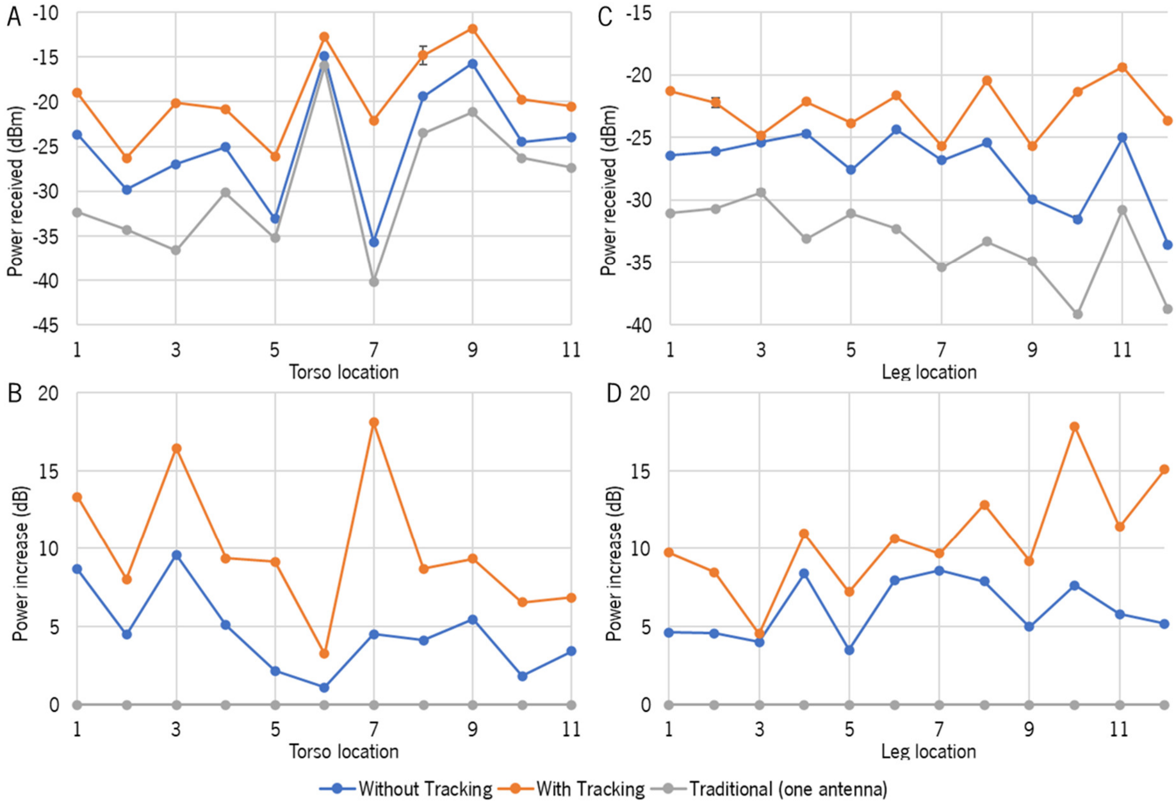

Figure 5.18 – Power received by the implant (top) and power increase (bottom) relative to the traditional one-transmitter scenario for each measurement location in the torso (left) and lower leg (right) models.

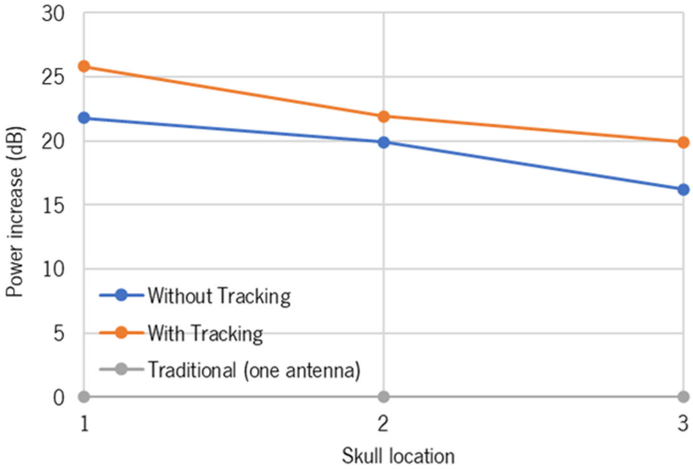

Figure 5.19 - Power increase relatively to the traditional one-transmitter scenario for each measurement location in the skull model.

The results obtained in the geometrically accurate models further validated the improvement that the proposed WPT system provides over traditional WPT approaches, this time in more realistic models with different medium shapes and a fully functioning wireless device inside the models. It is possible to conclude that with this system we can increase immensely the power transferred to an implantable device that moves along an unknown path inside the human body, treating the propagation medium as black box.

5.5 Closing remarks

The multimodal WPT system with multiple transmitters and tracking was validated in this chapter. The distribution of power inside a human head phantom was mapped for a traditional single-transmitter WPT system and then compared with the improvements proposed in this thesis. Furthermore, the WPT system was used to transfer power to a fully functional wireless device inside models of the human body. It was demonstrated that the proposed WPT system significantly increases the power delivered to the implant and can track it without prior knowledge of the implantation medium.

A power of -13.7 dBm was delivered to an antenna inside a human head phantom at a depth of 5.3 mm. Adjusting the transmitted power for a SAR_{10g} of 10 W/kg, -0.9 dBm would be delivered to the antenna. Comparatively to a single antenna WPT link, the proposed system increased the power provided to the ‘implant’ by up to 18 dB in the torso and leg models, and 25 dB in the skull model. This ultimately means that the proposed WPT system has fulfilled its requirements and it has the potential to be used in a broad spectrum of applications, as the concepts it employs are not limited to the medical field.

CHAPTER 6 CONCLUSIONS AND FUTURE WORK

The miniaturization of IMDs is a cornerstone for enabling advances and breakthroughs in the medical field, leading to an improvement of the quality of life of patients. However, several hurdles need to be overcome for this to become a reality. One of the most significant obstacles is the powering of the device, as suitable battery technology for miniaturized devices is still lacking. This thesis studied WPT solutions and came up with a way to increase the amount of power transferred to an IMD, enabling medical breakthroughs to take place.

6.1 Conclusions

Understanding how EM waves interact with biological mediums and how to calculate the safety exposure limits allowed us to identify WPT link parameters that could be explored to increase the power inside a medium. We did this by using multiple transmitters with multiple propagation paths to ‘distribute’ the energy across the medium, and combining the phase of the signals to track and focus power at the target location.

The previous findings were tested and after confirming their potential to improve WPT to implants, we proposed, developed, tested and validated a WPT system with six transmitters and tracking capabilities. We mapped the power distribution inside a human head phantom and demonstrated that it is possible to significantly increase the amount of power delivered to an IMD inside a human head phantom comparatively to the single-transmitter approach that is traditionally employed, without increasing the maximum SAR in the medium. Our system is capable of providing a power of -13.7 dBm to an antenna inside a human head phantom at a depth of 5.3 mm. Furthermore, the system can deliver -0.9 dBm to the antenna by adjusting the transmitted power for a SAR_{10g} of 10 W/kg.

We designed a wireless device to demonstrate the system’s suitability to power a fully-implantable device inside human body models with accurate geometrical features. We proved that the WPT system increases the power delivered to the wireless device as it moves inside the models. In the torso and leg models, the power delivered to the implant was increased by up to 18 dB, while in the skull model, the gain was 25 dB, comparatively to the single transmitter scenario, where the antenna used for the traditional scenario was the one placed closest to the implant. It is noteworthy that implementing alternative antenna array designs can increase the power gain even more. Additionally, the WPT system can track the implant at a rate of up to 3.4 Hz.

The proposed multitransmitter WPT system enables the natural and necessary miniaturization of IMDs, because the increase in power available to the IMD can compensate for their loss in WPT efficiency due to smaller sizes. Additionally, by using RF signals and tracking, it is more robust against misalignments than IC and US solutions thus allowing further implantation depth. Therefore, the findings of this thesis have the potential to see a widespread application in the future and become a staple in WPT solutions for miniaturized IMDs.

Recently, some works were presented that also make use of tracking technology in US WPT systems which reported significant increases in power delivered to the targets [1], [2], which demonstrates that concepts used in this thesis can be implemented in other WPT technologies. Additionally, in 2020 a study was published where beamforming was used to track and transfer power to IMDs at a distance of two meters which increased power delivery by over five-fold [3], further demonstrating the potential of this technology. However, the use of multiple propagation paths in the biological medium through multiple transmitters to increase power availability has not, to the best of the author's knowledge, been implemented before.

The multimodal WPT system is capable of operating in a black-box environment, it is easily scalable in terms of the number of transmitters, and its periodic phase measurement algorithm allows real-time tracking of the IMD, therefore a plethora of applications can be envisaged, amongst which:

- Employment in a vest to track and transfer power to an endoscopic capsule;
- Creating a universal IMD recharge station: a chair with several sets of antennas, where a patient with a compatible IMD (beacon-emitting) can sit and wait while the system detects which antenna array to use and then recharges the IMD's battery;
- Development of a universal WPT station for testing wireless devices in mice: simply placing the antennas in the cage and letting the WPT system track and transfer power to the device under test, alleviating weight carried by the mice which can influence the results.

6.2 Future work

The work carried out in this thesis is not over, and the proposed WPT system is far from complete. Before implementing the previously mentioned potential applications, some improvements to the system have to be made, as they have proven to be shortcomings in the current version.

The first upgrade to the WPT system would be to change its operating frequency to one whose use isn't as widespread. With 2.45 GHz, the abundance of Wi-Fi and Bluetooth sources in the vicinity of the WPT system difficult an accurate beacon reception and processing when its power is low. This would, however, require the design of a new module for implants to transmit the beacon, as off-the-shelf components that can perform that task would most likely not exist. This module can be implemented in CMOS technology and then added to the implants.

Followingly, the WPT system was produced using evaluation boards for quick setup construction. To massively reduce costs and overall device volume, a custom PCB that integrates all the necessary components must be designed. With this, the expensive and voluminous evaluation boards are no longer required, and the extensive and complex cabling of the system can be better managed. Additionally, to maximize the power delivered to the IMD, this opportunity can be used to upgrade some components of the system, namely the power amplifiers, as the current power output can be increased safely.

Another essential upgrade to the system is the implementation of an adaptable reference antenna. As the reference is the most critical channel of the system, as all others are measured relative to it, the system should identify which of the antennas receives the beacon with the highest power and then use it as the reference. This can be achieved with RF switches.

Finally, another WPT link parameter can be used to concentrate power at the implant's location, which is the combination of multiple frequencies. This was demonstrated in [4], where the authors implement multiple frequencies to concentrate power in a tumour for ablation. A WPT system with multiple frequencies was also presented in [5] that is capable of powering multiple miniaturized devices inside biological medium. Hence, it can be of interest to integrate the use of multiple frequencies in the WPT system presented in this thesis.

6.3 References

[1] M. L. Wang, T. C. Chang, and A. Arbabian, "Ultrasonic Implant Localization for Wireless Power Transfer: Active Uplink and Harmonic Backscatter," *IEEE Int. Ultrason. Symp. IUS*, vol. 2019-Octob, pp. 818–821, 2019.

[2] M. Meng and M. Kiani, “Self-Image-Guided Ultrasonic Wireless Power Transmission to Millimeter-Sized Biomedical Implants,” *Proc. Annu. Int. Conf. IEEE Eng. Med. Biol. Soc. EMBS*, pp. 364–367, 2019.

[3] X. Fan *et al.*, “Towards flexible wireless charging for medical implants using distributed antenna system,” *Proc. Annu. Int. Conf. Mob. Comput. Networking, MOBICOM*, pp. 280–294, 2020.

[4] G. G. Bellizzi, L. Crocco, G. M. Battaglia, and T. Isernia, “Multi-frequency constrained SAR focusing for patient specific hyperthermia treatment,” *IEEE J. Electromagn. RF Microwaves Med. Biol.*, vol. 1, no. 2, pp. 74–80, 2017.

[5] Y. Ma, Z. Luo, C. Steiger, G. Traverso, and F. Adib, “Enabling deep-tissue networking for miniature medical devices,” in *Proceedings of the 2018 Conference of the ACM Special Interest Group on Data Communication*, 2018, pp. 417–431.

ANNEX 1 - WPT SYSTEM BILL OF MATERIAL

Components of the WPT system and their characteristics.

Device	Model	Frequency range (MHz)	Gain (dB)	Resolution	Input power limit (dBm)	Ref.
Control and proc. unit	MEGA 2560	N/A	N/A	10 bit [1]	N/A	
RF switch	ZX80-DR230-S+	0-3000	-0.9	N/A	33.0	
6-way splitter/combiner	ZB6PD-2-S+	800-2000	-9.0 [2]	N/A	40.0	
90-degree splitter	ZX10Q-2-27-S+	1700-2700	-3.4	N/A	43.0	
VCO	ZX95-3800A-S+	1900-3700	4.1 [3]	N/A	N/A	
Power amplifier	SKY66294-11	2000-2300	30 [4]	N/A	10.0	
Phase shifter	PE44820	1700-2200	-6.0	1.9 deg/step	28.0	
Phase detector	AD8302	>0-2700	N/A	10.0 mV/deg	10.0	
Attenuator	VAT-3+	0-6000	-3.2	N/A	30.0	
50 Ohm load	MCL ANNE-50L+	0-12000	N/A	N/A	30.0	
Bandpass filter	CBPFS-2441	2389-2499	-1.5 [6]	N/A	20.0	
Low-noise amplifier	ZX60-272LN+	2300-2700	14 [7]	N/A	17.0	
Variable gain amplifier	DVGA1-242APP+	450-2400	[-10.8, 20.7] [8]	N/A	24.0	
Limiter	VLM-73-1W-S+	30-7000	-0.3 [9]	N/A	31.8	
Coupler	ZABDC10-25HP	1500-2500	-0.5	N/A	40.0	
Power detector	DC1120A	40-3800	N/A	17.7 mV/dB [10]	15.0	

[1] ADC resolution

[2] at 2.45 GHz

[3] power output

[4] at 2.45 GHz. Maximum power output = 36.3 dBm

[5] maximum power output = 17 dBm

[6] at the passing band

[7] maximum power output = 18.3 dBm; NF=0.8 dB

[8] maximum power output = 22.5 dBm

[9] maximum power output ≈ 10 dBm

[10] minimum power input = -70 dBm